Neurologische klinik und Poliklinik

Ludwig-Maximilians-Universität München

Dissertation
zum Erwerb des Doctor of Philosophy (Ph.D.)
an der Medizinischen Fakultät der
Ludwig-Maximilians-Universität zu München

The role of CX3CR1 for cerebral metastasis formation

.....Wenlong..ZHAGN.....

..Dongying,.Shandong,.China...

2020

First supervisor: Prof. Dr. Steffen Massberg

Second supervisor*:* Prof. Dr. Andreas Straube

Third supervisor: Prof. Dr. Christian Schulz

Dean: **Prof. Dr. med. dent. Reinhard Hickel**

Datum der Verteidigung:

__23.03.2020_

Wenlong Zhang (PhD student)

AG Experimental Neuro Oncology,

Department of Neurology,

University hospital

Munich University, Munich, Germany

PhD Thesis

The role of CX3CR1 in cerebral metastasis formation

PhD “Medical Research” (IRTG914)

Contents

List of Figures

Abbreviations

AGM	Aorta-gonad-mesonephros
APP	Amyloid precursor protein
ATP	Adenosine triphosphate
BBB	Blood-brain barrier
CCL2	Chemokine (C-C motif) ligand 2
CCL7	Chemokine (C-C motif) ligand 7
cDNA	Complementary DNA
CX_3CR1	CX_3C chemokine receptor 1
CX3CL1	Chemokine (C-X3-C motif) ligand 1
CSF-1R	Colony stimulating factor 1 receptor
CNS	Central nervous system
DAMPs	Damage-associated molecular pattern molecules
DAPI	4', 6-Diamidino-2-phenylindole
DCs	Dendritic cells
DMSO	Dimethyl sulfoxide
DMEM	Dulbecco's Modified Eagle' Medium
DR6	Death receptor 6
ECs	Endothelial cells
EGF	Epidermal growth factor

FACS	Fluorescence-activated cell sorting
FBS	Fetal bovine serum
FITC	Fluorescein isothiocyanate
F4/80	EGF-like module-containing mucin-like hormone receptor-like1
GABA	Gamma-Amino butyric acid
GDNF	glia cell-derived neurotrophic factor
GFP	Green fluorescent protein
G418	Geneticin
GM-CSF	Granulocyte-macrophage colony-stimulating factor
GL261	Glioma 261
HFG	Hepatocyte growth factor
HSCs	Hematopoietic stem cells
IBA 1	Ionized calcium-binding adapter molecule 1
i.v.	Intravenously
i.p.	Intraperitoneal
LL/2-Tdt	Lewis lung carcinoma/LLc1-Tdtomato
mRNA	Messenger ribonucleic acid
MDPs	Macrophage and/or dendritic cell progenitors
MIP	Maximum intensity projection
MLKL	Mixed lineage kinase domain-like pseudokinase
NaCl	Sodium chloride solution

NF1	Neurofibromatosis type 1
NK	Natural killer
PBS	Phosphate-buffered saline
PCR	Polymerase chain reaction
PFA	Paraformaldehyde
PMT	Photomultiplier tubes
PTEN	Phosphatase and tensin homolog
RIPK1	Receptor-interacting serine/threonine protein kinase 1
RNA	Ribonucleic acid
RFP	Red fluorescent protein
ROI	Region of interest
rpm	Rotations per minute
s.c.	Subcutaneous
SD	Standard deviation
SF	Scatter factor
STI1	Stress-inducible protein 1
TAMs	Tumor-associated microglia and macrophages
tdTomato	Tandem dimer tomato, a red fluorescent protein derived from a monomeric mutant of *DsRed*

1 Abstract

Brain metastasis frequently occurs in individuals with cancer and is often fatal. The interactions between tumor cells and tumor-associated microglia/macrophages (TAMs) in different steps of cerebral metastasis formation are poorly characterized. Moreover, the role of CX3CR1 in brain metastasis is still unclear.

To elucidate the mechanism underlying brain metastasis formation, our group established a syngeneic cerebral metastasis mouse model by combining a chronic cranial window and two-photon laser scanning microscopy (TPLSM), which allows the tracking of single fluorescent metastasizing tumor cells *in vivo* over time for a period of weeks. Transgenic CX3CR1$^{GFP/wt}$, CX3CR1$^{GFP/GFP}$ mice and red fluorescent Lewis lung carcinoma/LL/2/LLc1-Tdt tumor cells were used for *in vivo* imaging. The role of CX3CR1 was investigated by comparing the density and cell body volume of TAMs, as well as the fate of single metastatic tumor cells in different steps of cerebral metastasis formation. Interactions between TAMs and metastatic tumor cells were also assessed by TPLSM.

Herein, we illustrate that TAM density and cell body volume are influenced by metastatic tumor cells in different steps of cerebral metastasis formation. Both the density and cell body volume of TAMs are increased during tumor growth and decreased in regressing tumors. TAMs have close contact with metastatic tumor cells in different steps of cerebral metastasis formation, and their interactions in early steps assist in the elimination of tumor cells. CX3CR1 deficiency decreases the number of TAMs infiltrated into metastatic tumor lesions, but the cell body volume of TAMs is not influenced. The absence of CX3CR1 increases the efficiency of cerebral metastasis formation.

Our data indicate that CX3CR1 mediates interactions between TAMs and metastatic tumor cells in different steps of cerebral metastasis, and CX3CR1 inhibition facilitates brain

metastasis formation.

2 Introduction

Brain metastasis commonly occurs in patients with systemic cancer and is associated with a dismal prognosis[1]. Therefore, improved therapeutic approaches are urgently needed for patients with brain metastasis. The development of novel therapies requires a detailed understanding of the complex process of brain metastasis formation and growth within the brain microenvironment.

Previous studies have shown that successful metastasis formation requires several steps: intravasation of tumor cells into the tumor vasculature, circulation of tumor cells in the bloodstream, arrest in capillaries at distant sites, and extravasation into the parenchyma of the target organs to start colonization[2]. Accumulating evidence underscores the importance of the tumor microenvironment and immune cells for tumor metastasis[3-7].

Parenchymal microglia are the main resident immunological cells in the CNS. Additionally, the brain hosts several myeloid cells, including perivascular macrophages, meningeal macrophages and choroid plexus macrophages[8]. Although all of these microglia/macrophages share numerous myeloid- and macrophage-specific markers (such as IBA1, F4/80, and CX3CR1) and exhibit similar immune regulatory functions (such as local immune surveillance and removal of debris), early results suggested that they have a distinct ontogenesis, with microglia being derived from the yolk sac while macrophages originate from hematopoietic stem cells (HSCs) of the bone marrow[8-10]. A former study has shown a large number of infiltrating microglia/macrophages in brain metastasis lesions[11-13]; however, the exact role of TAMs in brain metastasis is still unclear. Immunohistochemistry results indicate that during the initial steps of breast cancer brain metastasis, activation of microglia will assist in cancer cell extravasation and progression[14], while an *in vitro* assay showed that LPS-activated microglia induced apoptosis of metastatic lung cancer cells in a dose and time-dependent manner[12].

The seven-transmembrane receptor CX3CR1 is a specific receptor for the CX3CL1 chemokine fractalkine (FKN), which is expressed on monocytes, brain microglia, subsets of NK and dendritic cells[15]. CX3CL1 and its receptor CX3CR1 are thought to be important for the trafficking of immune cells and intercellular communication between different cell types. Research has shown that the CX3CL1/ CX3CR1 system has a crucial tumor-promoting role in human glioblastomas via its impact on glioma-infiltrating immune subsets[16]. Thus, CX3CR1 may act as a potential therapeutic target for cerebral metastasis formation.

To shed light on the interactions between TAMs, and metastasizing tumor cells in the brain and to identify the factors (for example: CX3CR1) that mediate their interactions during brain metastasis, our group established an animal model that allows the tracking of single metastasizing tumor cells from different carcinomas *in vivo* over time for a period of weeks using dual photon microscopy and a chronic cranial window[17].

2.1 Cerebral metastasis

Metastasis means that cancer cells that originate from the primary tumor site spread to a distance organ, which is the main cause of death of cancer patients[18]. Among cancer patients, 10-20% develop brain metastasis. Brain metastasis occurs 10 times more often than primary brain tumors[19-21]. Usually, brain metastases occur in the late steps of cancer progression and are associated with a poor prognosis. Furthermore, the brain is a sanctuary site for cancer cells, as some large molecule drugs are unable to cross the blood-brain barrier (BBB). Brain metastasis most often derives from lung cancer (3.1%), breast cancer (2.9%), and melanoma (2.8%) (**Figure 1**)[22].

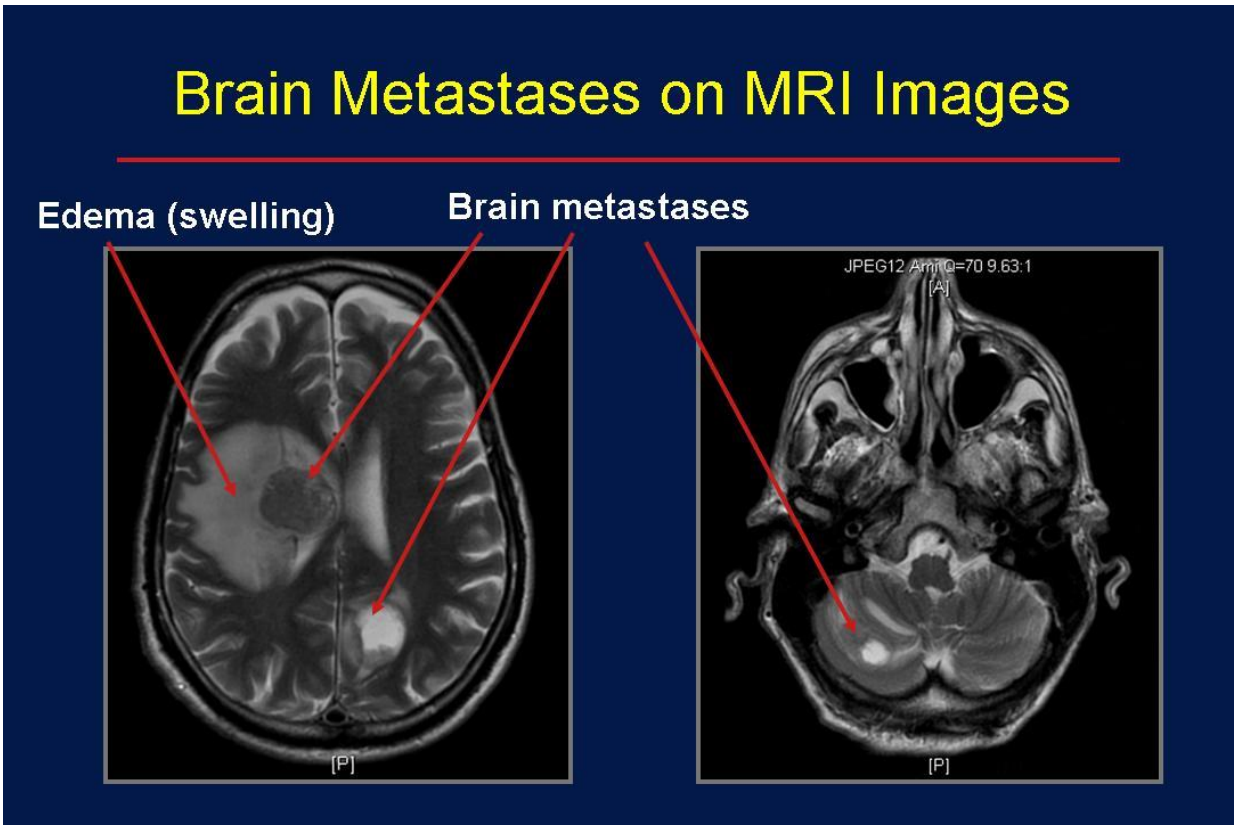

Figure 1: Magnetic resonance images of brain metastases.

Coronal (left) and transverse (right) section of MRI images from brain metastasis patients. Metastases were observed near the ventricle, cerebellum. Edema is also observed because of the metastases. (Image from Carolyn Vachan *et al.* 2017[23])

Blood flow and tissue volume are the main factors influencing the distribution of brain metastasis. Former research has shown that 80% of brain metastases occur in the cerebral hemispheres, followed by the cerebellum (15%) and the brainstem (5%)[24].

Clinical symptoms of brain metastases are headache, seizures, and neurological deficit. Neuropsychological testing illustrates that 65% of brain metastasis patients suffer from cognitive impairment[25,26], which might be a result of brain tissue damage because of tumor proliferation, cerebral edema, high intracranial pressure, and vascular compromise[27].

Unfortunately, the treatment options are limited for brain metastasis. The commonly used therapeutic strategies for brain metastases include surgical removal, chemotherapy, radiation therapy, and growth factor inhibitors[27]. For multiple brain metastases, whole-brain radiation therapy is recommended. For patients with oligometastases (one to three metastases) or multiple lesions less than 3 to 4 cm, stereotactic radiosurgery is recommended[28].

2.2 Brain metastasis cascade and organ-specific metastasis

Brain metastasis is a very complex process. For successful brain metastasis formation, tumor cells need to successfully complete several steps known as the metastasis cascade (Figure 2). First, single tumor cells have to escape from the primary tumor site, invade the surrounding tissue, and then intravasate into the blood stream or the lymphatic system. After circulating in the bloodstream, tumor cells must be arrested in the capillary bed of the brain. Afterwards, cancer cells need to extravasate successfully to survive in the host tissue. In the early stages of metastasis after extravasation, tumor cells will grow through cooption of the pre-existing vessels. For continued growth, micrometastases need to develop a new vascular network, a process known as angiogenesis. Each of these processes have proven to be very inefficient, indicating that in contrast to the large number of circulating tumor cells in the bloodstream, only a minority of tumor cells lead to cerebral macrometastasis.

With the development of in *vivo* imaging, more mechanisms behind the veil of metastasis have emerged. A murine lung metastasis model revealed that in the early metastatic niche, neutrophils, monocytes, dendritic cells, and macrophages have close interactions with circulating tumor cells before extravasation[29]. While another study focused on the interaction between tumor cells and endothelial cells, their data illustrated that the tumor cells induced endothelial cell necroptosis that facilitated extravasation and promoted metastasis. Furthermore, targeting the DR6 (death receptor)-mediated necroptosis signaling pathway worked as a novel anti-metastatic therapy[30].

Certain tumor cells shows organ-specific metastasis patterns; for instance, prostate cancer cells more easily form bone metastases, while melanoma frequently metastasizes to liver, lung, and brain[31,32]. The 'soil and seed' hypothesis from Stephen Paget illustrates two factors that may influence the organ-specific preference of tumor cells: the characteristics of cancer cells and the host organ microenvironment[33]. An alternative hypothesis from pathologist James Ewing indicates that circulation patterns of primary and secondary organs lead to organ-specific metastasis[34]. A new hypothesis proposes that cancer cells from the primary site may introduce some stromal components such as activated fibroblast to the host organs, which will facilitate tumor growth in the new microenvironment[35](**Figure 2**).

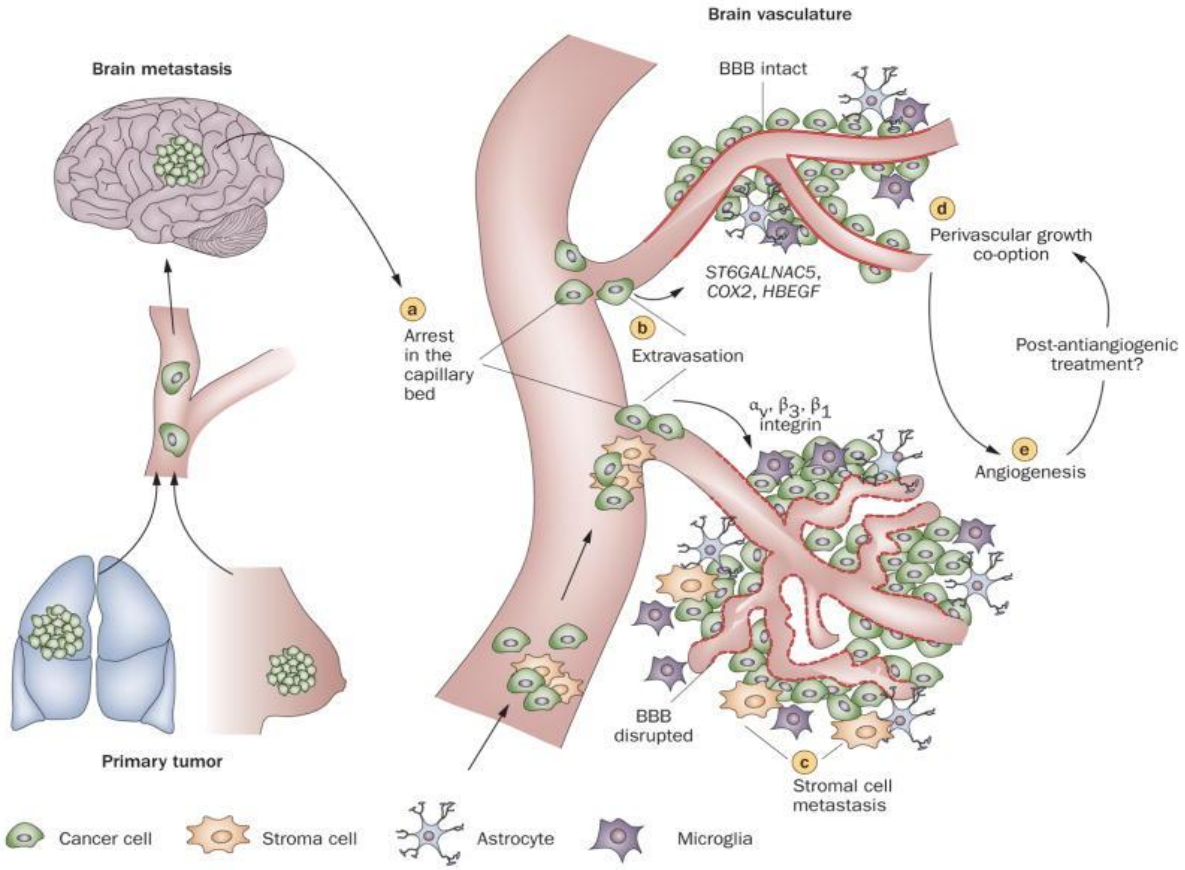

Figure 2: Brain metastasis cascade.

Brain metastasis is a multistep process. After escape from the primary tumor site, tumor cells must undergo the following steps to colonize in the brain parenchyma. a. Arrest in the capillary bed. b. Extravasation, mediated by *ST6GALNAC5, COX2,* and *HBEGF* genes; activated integrin $\alpha_v\beta_3$ andβ_1 are suggested to involved in arrest and adhesion of tumor cells to small capillaries. c-e. Perivascular growth through the cooption of pre-existing vessels and angiogenesis, the blood brain barrier (BBB) will be disrupted during tumor proliferation**.** (Image from April F. Eichler *et al*., *Nat Rev Clin Oncol*, 2011[27])

2.3 Brain tumor microenvironment

The main cell types in the brain are neurons, glial cells, including astrocytes, microglia, as well as oligodendrocytes, fibroblasts, and pericytes. The blood brain barrier also plays an important role in the CNS. Brain tumor progression involves the coevolution of cancer cells together with these stromal cells, extracellular matrix, and the vasculature. Under normal physiological conditions, the stroma functions as the main barrier against tumorigenesis; however, during tumor cell proliferation, this microenvironment may support cancer cell progression.

After extravasation into the brain parenchyma, tumor cells will encounter different kinds of host stromal cells, such as astrocytes and microglia[27]. Numerous publications have demonstrated the accumulation of microglia/macrophages in metastatic brain tumors, and their communication determines the fate of metastasis formation[12-14,36,37]. For instance, astrocyte-derived exosomes mediate microRNAs interactions with metastatic tumor cells, leading to tumor suppressor PTEN loss as well as increased secretion of CCL2, facilitating the recruitment of IBA1-positive cells at the micrometastasis site. The recruitment of IBA1-positive cells (ionized calcium binding adapter molecule 1, marker for microglia and macrophages) enhances tumor proliferation and outgrowth[38]. Not only astrocytes but also microglia/macrophages play an important role in cerebral metastasis. The role of TAMs in brain metastasis formation will be discussed later in this thesis. Neuron debris may also lead to the activation of TAMs[37]. Therefore, targeting stromal cells in the brain tumor mass microenvironment may serve as a good strategy for metastasis[27].

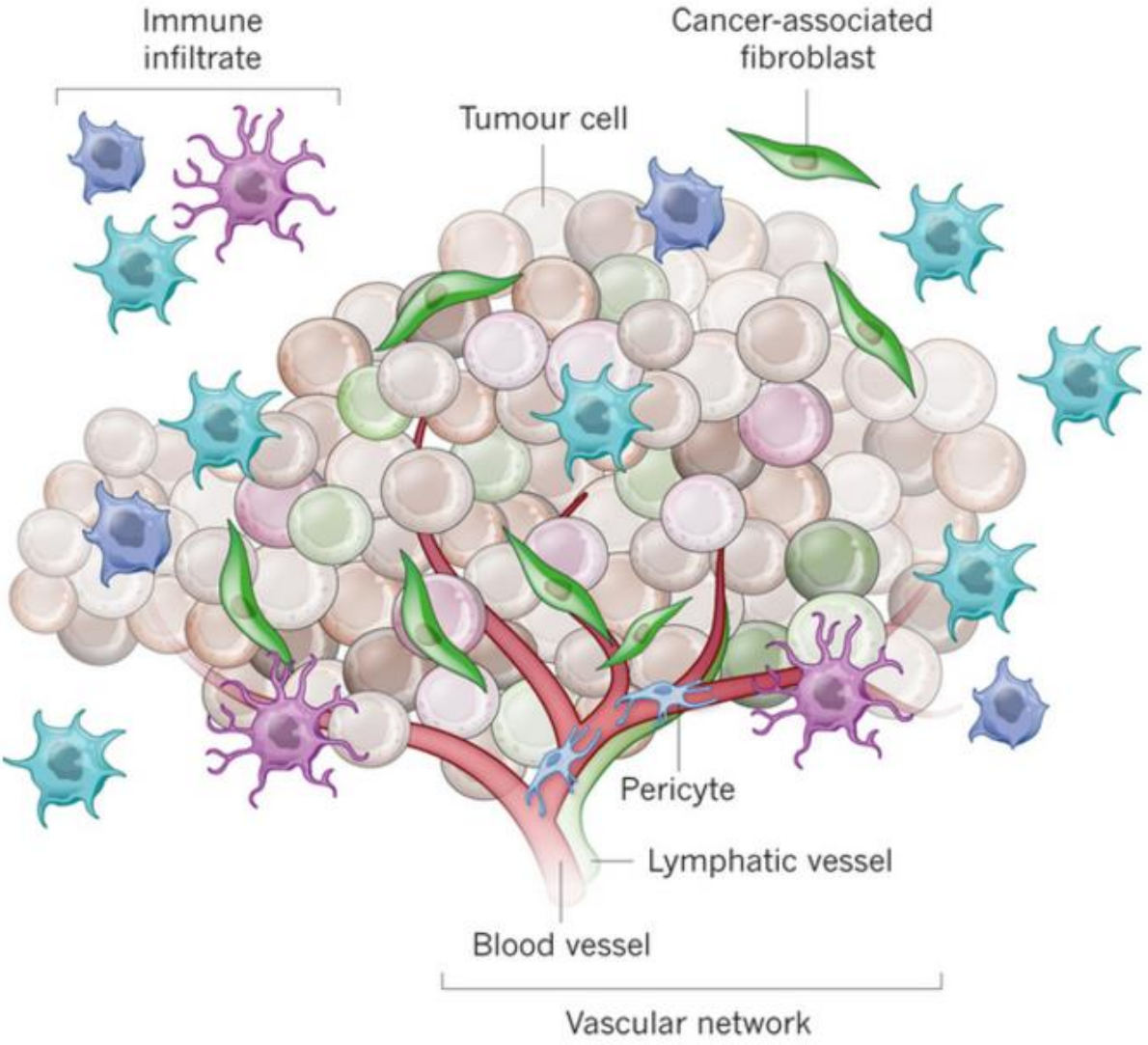

Figure 3: Tumor microenvironment in the CNS tumor mass.

Brain tumor lesions comprise a very complex microenvironment containing not only tumor cells but also many stromal cells, including pericytes, immune cells, and fibroblasts, and newly established vessels developed via a process known as angiogenesis. Cancer cells, stromal cells, factors, and vessels constitute the complex microenvironment. (Image from Melissa R. Jnttila, *et al.*, *Nature*, 2013[39]).

2.4 CX3CR1 and CX3CL1

CX3CR1 is a conventional $G\alpha_i$-coupled seven transmembrane receptor (Figure 4)[40], which is expressed on human monocytes, subsets of NK and T cells, dendritic cells, and brain microglia[15].

CX3CR1 is defined as the specific receptor of CX3CL1. Unlike any other known chemokine, CX3CL1, also known as a novel CX3C chemokine fractalkine (FKN), was found to exist in two isoforms: one is membrane-anchored and presented on an extended mucin-like stalk, and the other one is a soluble form that results from proteolytic cleavage. CX3CL1 has been shown to be expressed on activated endothelium cells[41,42], dendritic cells[43,44], astrocytes[45], and neurons[46,47]. The main functions of CX3CR1 are defined as the regulation of immune cell migration, adhesion, and activation[46,48-50].

Conventionally, CX3CL1 functions as a chemoattractant, and the literature indicates that high-affinity interactions between CX3CL1 and CX3CR1 assist the flow of peripheral leukocyte capture and adhesion[51]. In the CNS, the CX3CL1/CX3CR1 axis contributes to neuron-microglia communication[52,53], neuron survival[54,55], and neurotransmission[56].

CX3CL1 and CX3CR1 are overexpressed both at mRNA and protein levels in brain tumor masses[57-59]. However, the role of the CX3CR1/CX3CL1 axis in brain tumors is still controversial. Numerous evidence indicates that the CX3CL1/CX3CR1 axis mediates tumor invasion[60], proliferation[58,61], and metastasis[59,62,63], with the upregulation of CX3CR1 leading to increased infiltration of immune subsets[58]. Large numbers of infiltrating immune cells in tumor lesions may create a microenvironment that suppresses the immune response and favors tumor proliferation and metastasis[64]. Targeting nonneoplastic stromal cells can block tumor progression and metastasis[62,64-66]. In contrast, other GL261 murine glioma models with a CX3CR1 deficiency do not show altered microglia and lymphocyte infiltration, or tumor

growth[67].

Accordingly, we deduce that CX3CR1 may mediate the interactions between TAMs and metastatic tumor cells, and a deficiency of CX3CR1 may influence the recruitment and activation of TAMs and subsequently alter different steps of cerebral metastasis formation. To reveal whether CX3CR1 plays a role in the crosstalk of TAMs and metastatic tumor cells, and to investigate the role of CX3CR1 in the brain metastasis cascade, we initiated our project to focus on this receptor.

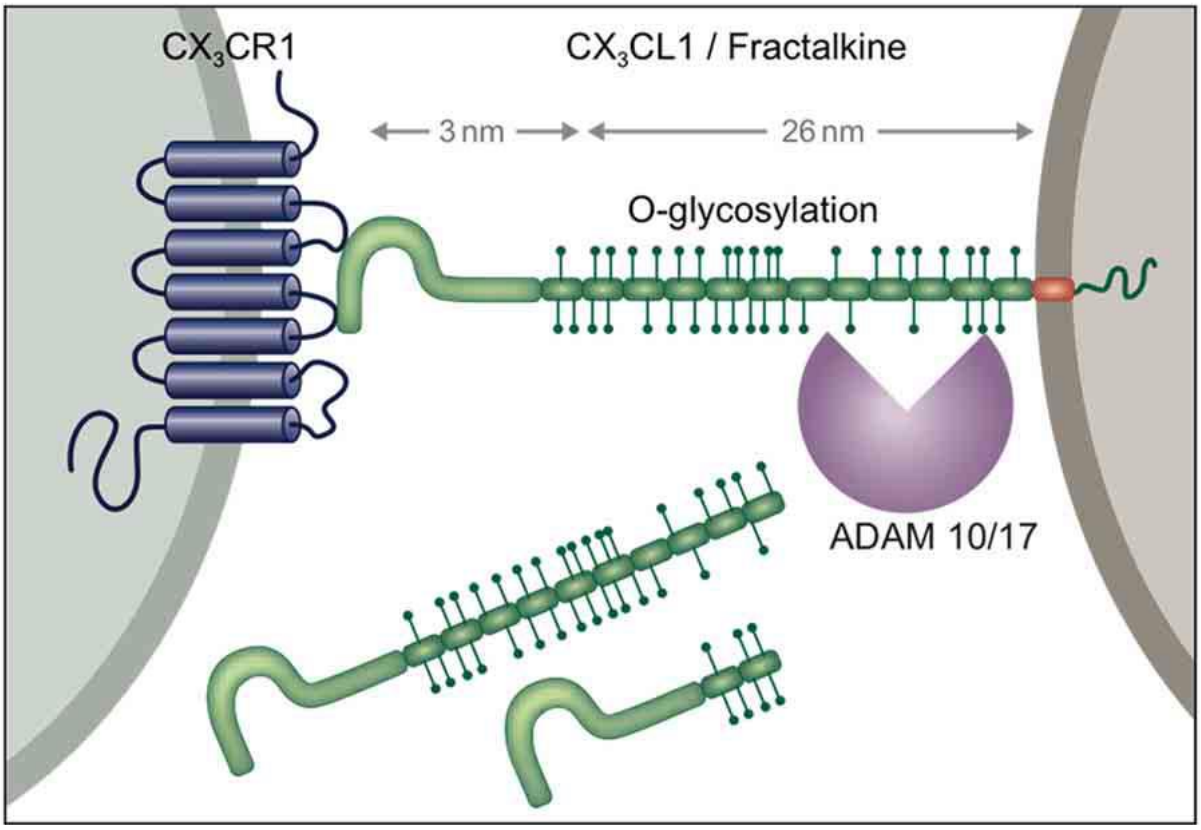

Figure 4: Schematic of the CX3C chemokine family.

CX3CR1 is a seven-transmembrane receptor, and its ligand CX3CL1 has two isoforms: the membrane-anchored and soluble form. Soluble CX3CL1 can be formed by proteolytic cleavage of anchored CX3CL1. (adapted Image from Zochai Wolf, *et al*., *Cellular Neuroscience,* 2013[40])

2.5 CX3CR1$^{GFP/wt}$ and CX3CR1$^{GFP/GFP}$ mice

The CX3CR1$^{GFP/wt}$ mouse strain was generated in 2000 to investigate the physiological interactions between CX3CR1 and its ligand FKN. In heterozygous transgenic mice, the physiological 390 bp of one *CX3CR1* exon following the CX3CR1 promoter, was replaced with EGFP cDNA[15], resulting in EGFP expression in monocytes, dendritic cells, NK cells, and brain microglia.

Homozygous CX3CR1$^{GFP/GFP}$ mice are robust, normal in size, fertile, and do not display any behavioral abnormalities. After chronic cranial window implantation, TAMs could be observed under two-photon microscopy using both normal CX3CR1$^{GFP/wt}$ mice and homozygous CX3CR1$^{GFP/GFP}$ mice. Furthermore, in homozygous CX3CR1$^{GFP/GFP}$ mice, both alleles were displaced by the GFP gene, resulting in no expression of the CX3CR1 receptor in this mouse strain, which thus served as a CX3CR1 deficiency mouse[68].

Another reason for using this transgenic mouse strain is that it on the C57/BL6 background, which is suitable for murine Lewis lung carcinoma/LL/2/LLc1 cells to establish a syngeneic cerebral metastasis mouse model.

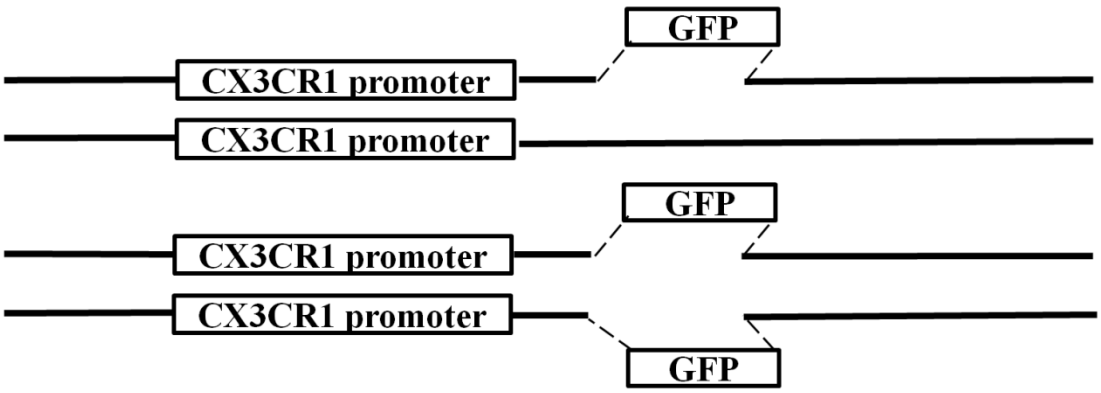

Figure 5: Targeted disruption of the murine *CX3CR1* gene.

In heterozygous CX3CR1$^{GFP/wt}$ mice, only one locus is replaced by the GFP gene, and thus, physiological CX3CR1 receptor is retained. In homozygous CX3CR1$^{GFP/GFP}$ mice, both alleles are replaced with GFP, providing a CX3CR1 deficiency mouse. (Steffen Jung *et al*., *Mol Cell Biol*, 2000[68])

2.6 Microglia and CNS macrophages

In 1932, Spanish neuroscientist del Rio-Hortega discovered microglia using silver staining and light microscopy[69]. Several decades later, in 2005, through two-photon microscopy, scientists found that microglia continually survey their surrounding microenvironment with marked changes in their morphology[70].

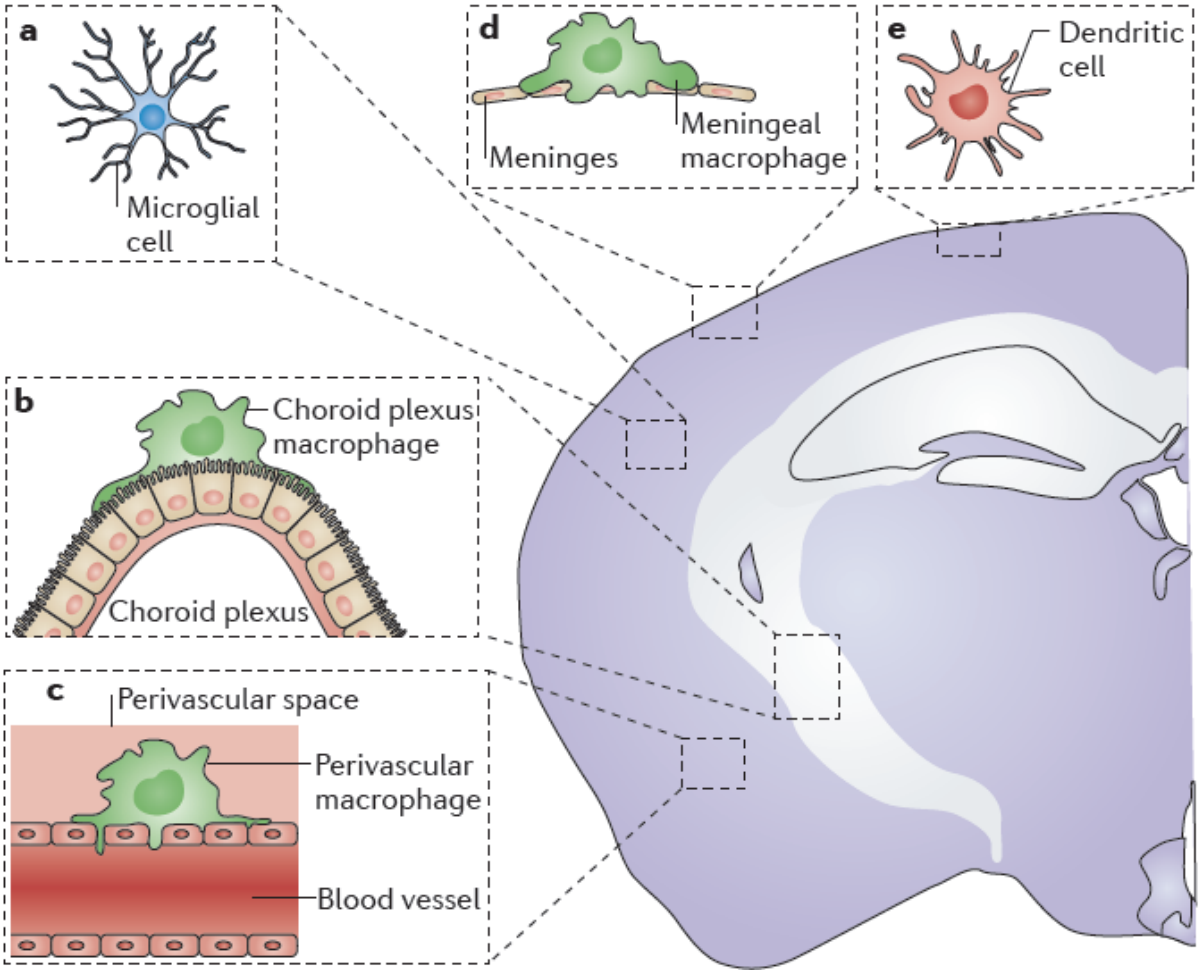

Figure 6: Myeloid cell types in the brain.

There are different kinds of microglia and macrophages distributed in the brain. In addition to brain microglia, other types of macrophages include perivascular, choroid plexus, and meningeal macrophages (image from

Marco Prinz, *et al.*, *Nature Review*, 2014[71]).

After further investigation, scientists unveiled the mystery of microglia: they are the main resident immunological cells in the CNS (central nervous system), constituting 12% of all cells in the CNS. Different from macrophages, microglia are long-lived and normally not replaced by peripheral cells from the circulation[72]. Moreover, microglia are self-renewable in a context-dependent manner to ensure cell expansion. Fate-mapping studies have demonstrated that, under homeostatic conditions, microglia originate from HSCs (hematopoietic stem cells) of the yolk sac[73-75], which illustrates that the microglial compartment is already established before birth[76]. Microglia are extremely plastic and undergo various structural changes. The resting form of microglia consists of a small cell body and long branching processes, which are very sensitive to the surrounding changes, serving as important sensors of injury and pathology. Once activated by certain stimuli such as inflammation, microglia enter an activated state, and their structure changes from a branched to an ameboid form or even to a phagocytic morphology. After activation, microglia will express pro-inflammatory signaling molecules, present the undesired antigen and perform phagocytic functions[70,77-79].

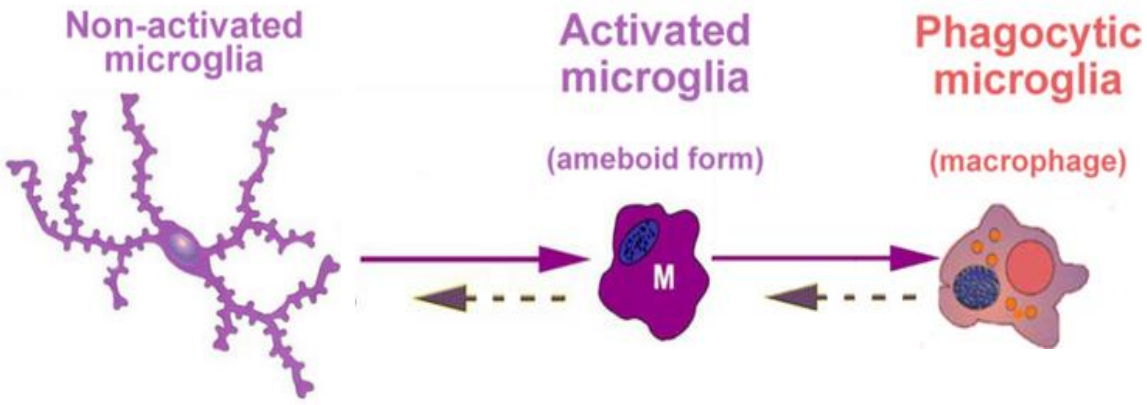

Figure 7: Morphological changes of microglia.

Certain stimuli can activate resident microglia into the activated amoeboid form, or even phagocytic microglia. Resident microglia usually have a small cell body and many processes, which are highly dynamic and keep

scanning the surrounding microenvironment. Once activated by certain stimuli, these processes will be retracted and the cell body will enlarge. Activated microglia present the amoeboid form or even the phagocytic form (Image from S. Vandenberg, *et al.*, *Introduction to the pathobiology of the Nervous system*, 2010[80]).

In addition to parenchymal microglia, there are several other myeloid populations in the brain, including perivascular, choroid plexus, and meningeal macrophages[81,82]. Macrophages originate from the definitive hematopoiesis that starts at E10.5, first in the aorta-gonad-mesonephros (AGM) region, or later, at E12.5, in the fetal liver[83,84]. Postnatally, monocytes are formed in the bone marrow. Hematopoietic stem cells (HSCs) generate monocytes from myeloid precursors (MPs) and macrophage and/or dendritic cell progenitors (MDPs)[82,83].

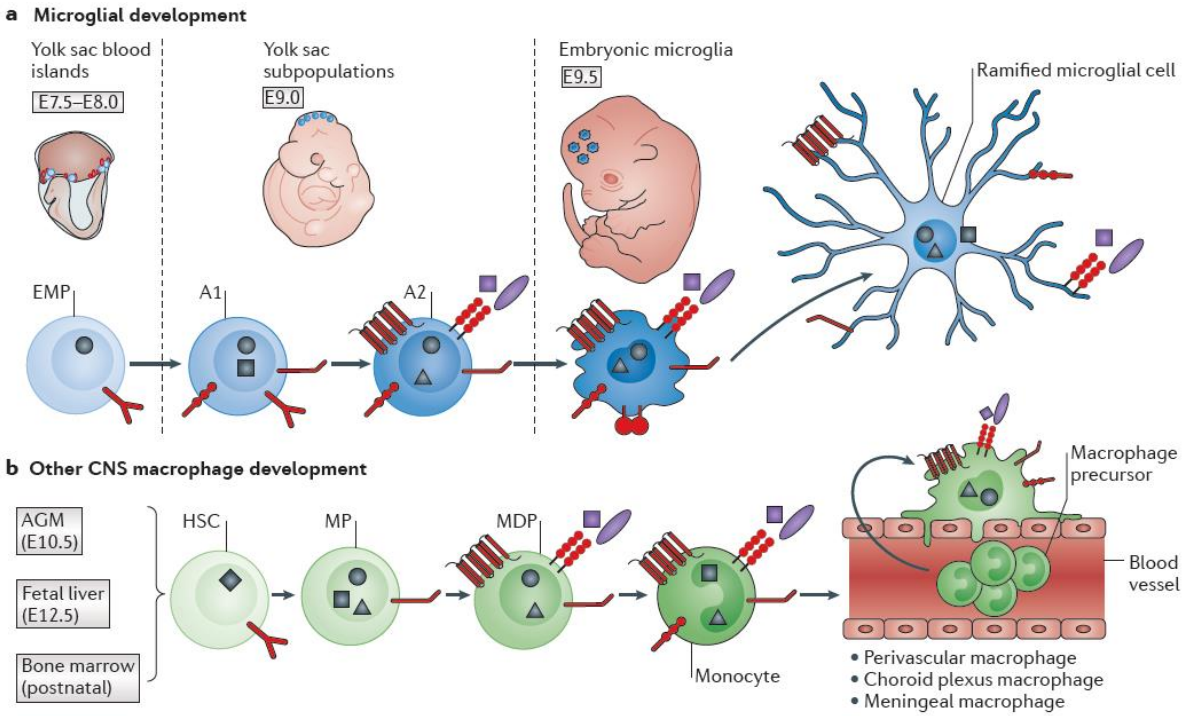

Figure 8: Distinct ontogenesis of microglia and macrophages.

Microglia and CNS macrophages have different origins and development processes. Microglia originate from the blood island of the yolk sac and are established before birth, while other CNS macrophages are generated via hematopoiesis. Different markers are expressed during different steps of microglial/macrophage development. a

Microglia originate from erythromyeloid progenitors (EMPs) at embryonic day 7.5-8.0 in the yolk sac in mice, and subsequently, these cells upregulate different markers as indicated and populate the brain mesenchyme. b CNS macrophages are derived from definitive hematopoiesis at E10.5 in the aorta-gonad-mesonephros (AGM), or at E12.5 in the fetal liver, or postnatally from bone marrow. Hematopoietic stem cells (HSCs) gradually develop into myeloid precursors (MPs) and then into macrophage and/or dendritic cell progenitors (MDPs), and surface markers are upregulated during the process of their maturation (Image from Marco Prinz, *et al*., *Nature Review*, 2014[71]).

2.7 Role of TAMs in cerebral metastasis formation and brain tumor outgrowth

Former studies have indicated that the majority of stromal cells in brain tumor masses are tumor-associated microglia and macrophages (TAMs); for instance, TAMs can make up as much as 30-50% of the brain tumor mass[85,86]. Research has repeatedly demonstrated that TAMs may play an important role in the processes of brain malignancies. Notably, TAMs exhibit both protective and antitumor functions. On the one hand, TAMs are accumulated and chronically activated during melanoma brain metastasis formation, the activation of TAMs facilitates metastatic tumor outgrowth in mouse brain, and high expression of matrix metalloproteinase 3 (MMP3) released from TAMs facilitates tumor cell metastasis[37]. Cross-talk between TAMs and metastatic melanoma cells induces matrix metalloproteinase 2 (MMP2) activation and enhances tumor proliferation and migration[87]. Microglia can facilitate metastatic breast cancer outgrowth in a Wnt-dependent manner[36]. A melanoma brain metastasis model has shown that the stimulation of TAMs is essential for the outgrowth of metastatic tumor cells[37]. Moreover, TAMs may contribute to angiogenesis and anti-angiogenic therapy resistance, and assist in tumor cell colonization and proliferation[88-90]. On the other hand, LPS-activated TAMs can induce apoptosis of metastatic lung cancer cells[12]. Activation of TAMs through Toll-like receptor (TLR9) agonist upregulates phagocytosis-related genes and reduces brain metastasis[91].

Different functions of TAMs may be attributed to their different subtypes. Generally, TAMs can be divided into two phenotypes: M1 and M2, which coexist in the tumor microenvironment, the proportions and balances of which will determine the fate of the tumor mass[92]. For the M1 subtype of TAMs, factors like IL-12, CXCL9, CXCL10, and CD86 are upregulated, which activate the immune response and facilitate the eradication of tumor cells[93,94]. In contrast, the M2 subtype of TAMs displays tumor-promoting functions based on the ability to express growth factors, proangiogenic cytokines, as well as immunosuppressive factors to inhibit T cell functions[95-98]. Transformation of the subtypes of TAMs is regarded as a good strategy for cancer treatment[94,99].

2.8 Two-photon laser scanning microscopy (TPLSM)

Two-photon excitation is a fluorescence process in which two photons are absorbed by a single fluorophore molecules to produce an excited state[100].

In 1931, Maria Göppert-Mayer established the theoretical basis of two-photon excitation[101], and decades later, this photophysical effect was verified experimentally by Kaiser and Garret in 1963. In 1990, the invention of two-photon fluorescence light microscopy by Denk, Webb and coworkers[102] revolutionized three-dimensional (3D) *in vivo* imaging of cells and tissues.

The principle of one-photon and two photon excitation is similar but slightly different. For one-photon excitation, the fluorophore is excited from the electronic ground state to an excited state, which requires one photon in the ultraviolet or blue/green spectral range. Nevertheless, this process can be achieved by simultaneous absorption of two longer wavelength photons under sufficiently intense laser illumination.

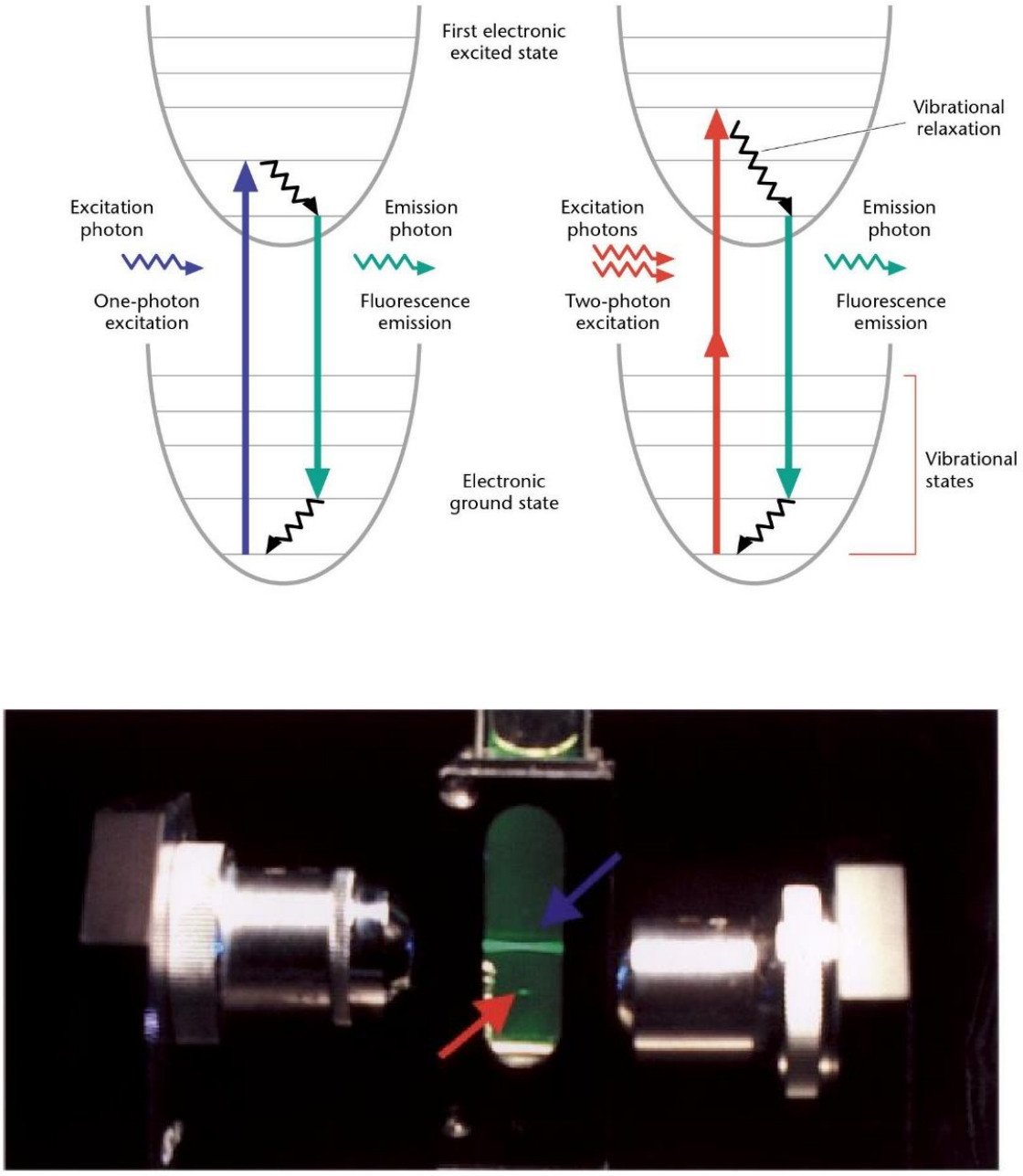

Figure 9: One-photon and two-photon microscopy.

One-photon excitation occurs through the absorption of a single photon, and fluorescence excitation is observed throughout the path of the laser beam. Two-photon excitation occurs through the absorption of two lower-energy photons, and fluorescence excitation occurs only from a 3D localized spot (Image from Peter TC So, Two-photon Fluorescence Light Microscopy, 2002[103]).

Two-photon fluorescence microscopy has both advantages and drawbacks compared with confocal microscopy. In contrast to one-photon excitation confocal microscopy, which illuminates the specimen with a double inverted cone of light, for two-photon microscopy, photobleaching and photodamage are limited to a subfemtoliter volume at the focal point. This reduction results in limited damage for the tissue and dramatically increases the viability of biological specimens[104]. Thus, TPLSM is more suitable for living organs.

Another advantage of two-photon microscopy is deeper tissue penetration. Two-photon excitation microscopy typically uses near-infrared excitation light, which minimizes scattering in the tissue. Third, two-photon microscopy minimizes signal loss, as no pinhole aperture is required. In confocal microscopy, out-of-focus light is rejected by the usage of a pinhole, which leads to a dramatic loss of photons at the confocal pinhole.

Previously, TPLSM was widely used in neuroscience, such as nervous system development, neuron degeneration diseases, cell plasticity and physiology[105-110].

The combination of two-photon intravital microscopy and transgenic rodents that express cell-specific fluorescence has opened up a new approach for studies of disease mechanisms and mammalian biology[111-113].

Although two-photon microscopy has certain advantages, it also have disadvantages such as a lower spatial resolution. The principles of physics reveal that the longer the wavelength of excitation light, the lower is the resolution. Two-photon excitation requires the usage of excitation that is twice that of the one-photon wavelength, leading to approximately half the resolution.

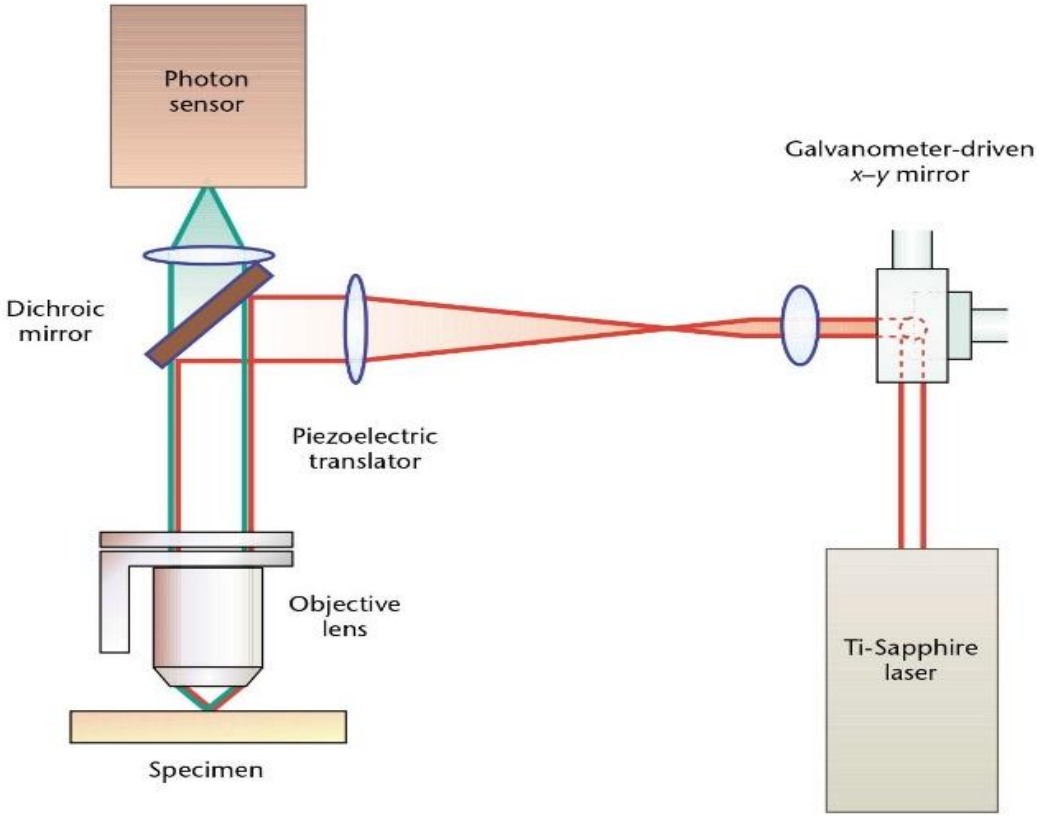

Figure 10: A schematic drawing illustrating the light path of a two-photon microscope.

The laser is excited by Ti-Sapphire and focused on the specimen by a complex light path system. The light signal is then obtained by a sensor and transferred to an electronic signal in the PMT. It is then presented on the computer screen after calculation (Image from Peter TC So, Two-photon Fluorescence Light Microscopy, 2002[103]).

2.9 Aim of this project

Despite numerous studies attempting to unravel the role of TAMs in brain metastasis, the exact function of these tumor-associated TAMs remains elusive and debatable. Thus, understanding the interactions between TAMs and metastatic tumor cells can not only reveal the mystery of the metastasis brain microenvironment but also help to identify novel therapeutic strategies for brain metastasis.

Therefore, the aims of this project are as follows:

to establish a syngeneic cerebral metastasis model for *in vivo* two-photon microscopy to follow the fate of metastatic tumor cells,

to investigate the dynamic interactions of TAMs and metastatic tumor cells during different steps of cerebral metastasis formation,

to investigate the role of CX3CR1 in cerebral metastasis formation.

3 Material and Methods

3.1 Cell culture

Lewis lung carcinoma/ LL/2 /LLc1-Tdt cells were obtained from the ECACC (European Collection of Authenticated Cell Cultures, Catalog No. 90020104). The base medium for this cell line is Dulbecco's Modified Eagle' Medium (DMEM, Gibco, Catalog No. 41965-039). To make complete growth medium, Fetal Bovine Serum (FBS, Biochrom GmbH, Catalog No. S 0615) was added to DMEM to a final concentration of 10%. After successful transfection with pLVX-tdTomato-IRES-Neo plasmid, selection medium should be used, thus G418 (an aminoglycoside antibiotic, also known as G418 sulfate and geneticin) (Biochrom GmbH, Catalog No. A 2912) should be added to the growth medium to a final concentration of 1000 µg/ml. A subcultivation radio of 1:4 to 1:6 is recommended, and the cells should be subcultured every 2-3 days. Two milliliters of trypsin (Biochrom GmbH, Catalog No. L 2123 Trypsin/EDTA Solution 0.05%/0.02% (w/v) in PBS) was used to resuspend the cells during subculture. The freezing medium contained 10% dimethyl sulfoxide (DMSO, SIGMA, Catalog No. D 2650) and 90% FBS. The liquid nitrogen vapor phase was used for long-term storage. Cells were regularly tested for mycoplasma infection using the PCR mycoplasma Test Kit (PanReac AppliChem GmbH, Darmstadt, Germany).

3.2 Generation of the pLVX-tdTomato-IRES-Neo vector

A PCR product with artificial EcoRI and BamHI enzyme restriction sites at the 5‘ and 3‘ ends containing the full-length coding sequence of the dimeric red fluorescent protein tdTomato was amplified using the plasmid DNA of the ptdTomato vector (Catalog No. 632531, TaKaRa Clontech) as a template and subsequently cloned into the EcoRI and BamHI sites of the lentiviral expression vector pLVX-IRES-neo (Content of the Lenti X Bicistronic Expression System, Catalog No. 632181, TaKaRa Clontech). The resulting construct (pLVX-tdTomato-IRES-Neo) was verified by restriction enzyme digestion and direct sequencing (10).

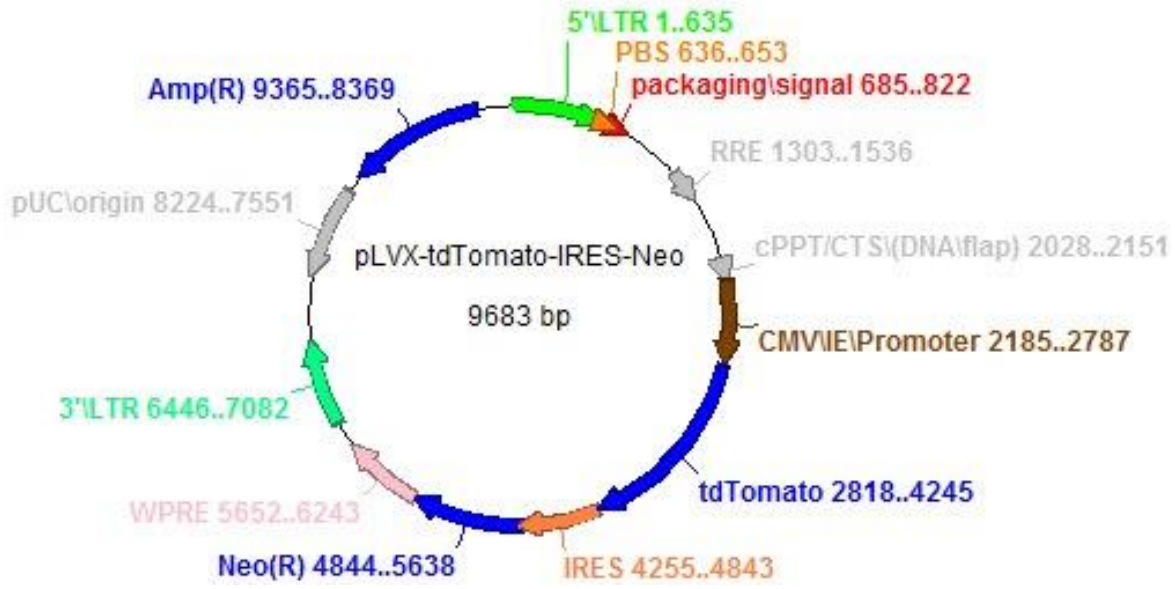

Figure 11: The pLVX-tdTomato-IRES-Neo plasmid.

The Td tomato sequence was cloned into a plasmid under the CMV/IE/promoter and amplified in the tumor cell line.

3.3 Red fluorescence protein gene transduction of cancer cells

We used Lipofection (Lipofectamine 3000, Thermo Fisher scientific) to transfect the vector pLVX-tdTomato-IRES-Neo (Catalog No. L3000015) into Lewis lung carcinoma/LL2/LLc cells according to the manufacturer's instructions. Briefly, lipo-transfection requires the following five steps. First, 5×10^5 cells must be planted into a 6-well plate and cultured overnight. Then, Lipofectamine Reagent is added in Opti-MEM medium (3.75 µl Lipofectamine 3000 in 125 µl Opti-MEM). The DNA was diluted in the Opti-MEM medium (5 µg/3 µl DNA into 250 µl Opi-MEM). Next, the samples from steps two and three were combined and incubated for 5 minutes at room temperature. Finally, the mixed reagents were placed in 2 ml growth medium to culture the cells. Two days after transfection, the cells were viewed under normal fluorescence microscopy to check whether red fluorescent tumor cells could be visualized.

After the cells are successfully transfected with the vector mentioned above, selection medium (details described in the cell culture part of this thesis) should be used to successfully select transfected cells. This selection medium was also used for long-term cell culture to maintain the selection pressure.

3.4 Fluorescence-activated cell sorting (FACS)

To obtain homogeneous and intense expression of Td-tomato in tumor cell lines, repeated FACS sorting (FACS Aria cell sorter, BD Bioscience) was performed.

Flow cytometry and cell sorting was performed as follows. Briefly, cells were resuspended and harvested using trypsin. Cells were diluted in FACS buffer (100 ml PBS, Biochrom Cat. No. L1815, 400 µl EDTA SIGMA, and 1 g BSA, ROTH) and adjusted to a concentration of 1-5 $\times 10^6$/ml. Before flow cytometry measurement, the cells were filtered using a 30-µm filter

(Sysmex, Catalog No. 04-004-2326) to avoid cell clusters.

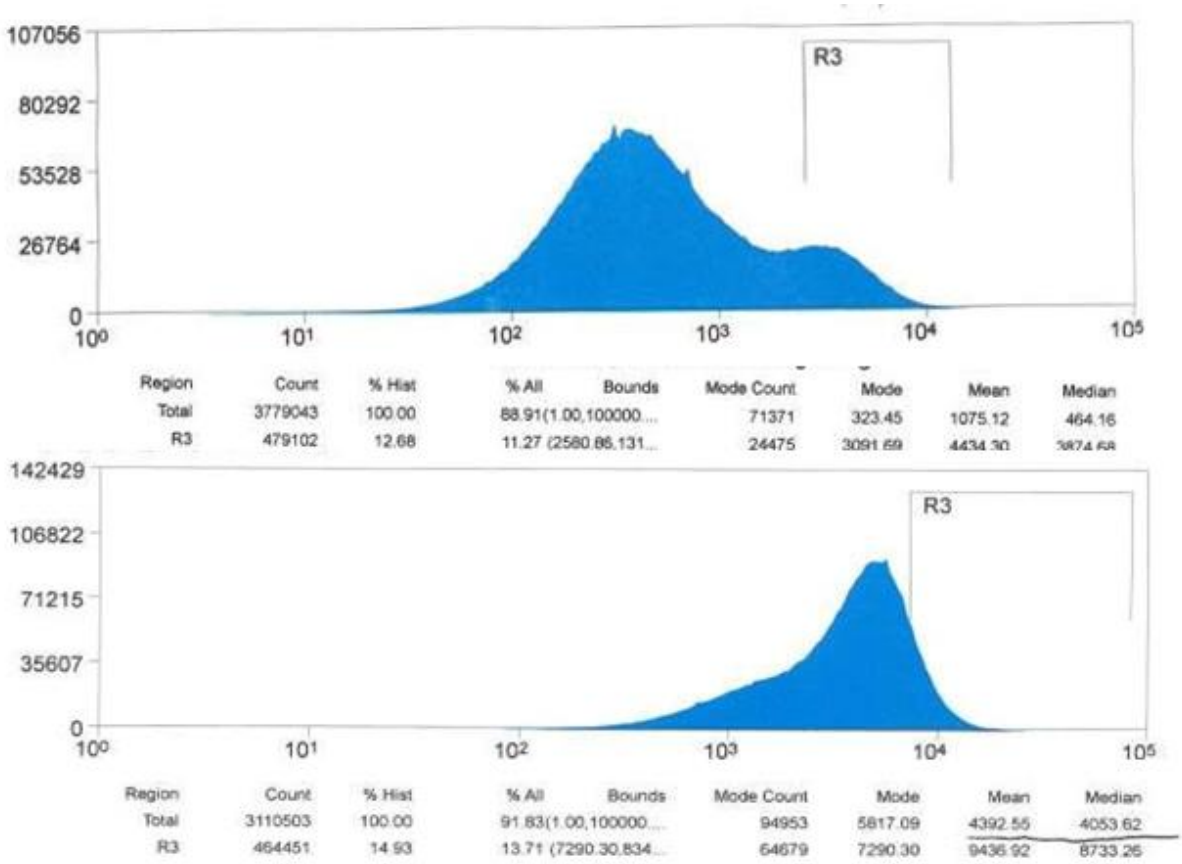

Figure 12: Representative FACS-sorting results showing the increase in the fluorescent signal after repeated sorting.

The images show that the mean fluorescence of the tumor cells increased from 464.16 to 4053.62 after repeated sorting. The peak of fluorescence also moved to the right.

3.5 Mouse experiments

We used 8-12-week-old female CX3CR1$^{GFP/wt}$, CX3CR1$^{GFP/GFP}$ mice and murine Lewis Lung carcinoma/LL/2/LLc1-Tdt cells for the experiment. First, a cranial window was prepared. To ensure that the inflammatory reaction had completely subsided, we waited for four weeks after cranial window preparation, and then tumor cells were injected through the internal carotid artery. In the CX3CR1$^{GFP/wt}$ group, a total of 14 mice were successfully injected with Lewis lung carcinoma/LL/2/LLc1-Tdt through the intracarotid artery; 8 mice could be used for *in vivo* imaging and further quantitative analysis, and 21 regions could be used for statistical analysis. The fate of 107 single cells could be successfully followed up over time. In the CX3CR1$^{GFP/GFP}$ group, 12 mice were successfully injected with Lewis lung carcinoma/LL/2/LLc1-Tdt through the intracarotid artery; 8 mice could be used for *in vivo* imaging and further quantitative analysis, and 40 regions could be used for statistical analysis. The fate of 137 single cells could be successfully followed up over time.

3.5.1 Cranial window preparation

Cranial windows were prepared as previously described[114,115]. After the mice were deeply anesthetized via intraperitoneal (i.p.) injection of MMF (midazolam 5 mg/kg, medetomidine 0.05 mg/kg, and fentanyl 0.5 mg/kg), a mixture of cefotaxime (250 mg/kg) and dexamethasone (2 mg/kg) was subcutaneously injected to reduce infection, inflammation, the cortical stress response, and cerebral edema. Then, the animal's heads were shaved, with additional use of depilatory cream. After completion of the preliminary treatment, the mice could be fixed on the stereotaxic apparatus. Next, eye ointment was applied to avoid eye dehydration and irritation. Povidone-iodine was then used for disinfection, followed by removal of the skin and cranial bone. Thereafter, the periosteum was removed and the cortical area of interest marked. Later, a thin circular groove around the region of interest was created with a dental drill. The thickness of the skull in the groove was checked by gently pushing the bone. If the island of the bone could be easily moved without attachment to the skull, we

started to remove the cranial bone. After successful skull removal, the dura meter was also separated from the leptomeninges and removed. If the superficial capillary was damaged and bleeding occurred during the process of dura removal, Tachosil (Takeda Austria, Linz, Austria) was applied and the procedure suspended until the bleeding stopped. During the whole microsurgical process, both the cranial bone and brain should be kept wet by application of 0.9% NaCl. The brain was covered with a 6-mm-diameter transparent and sealed with a dental cement mixture of ethylcyanoacrylate liquid and methylacrylate powder (Cyano veneer, Hager Werken, Duisburg, Germany). The ring was then placed around the cranial window and pasted. After surgery, 100 µl Temgesic (0.1 mg/kg/8 hour) should be injected subcutaneously, followed by 272 µl Wach (flumazenil 0.1 mg/ml 5 ml, atipamezole 5 mg/ml 0.5 ml, NaCl 3 ml) 30 mins later to awaken the mouse. The cage was placed on a heating plate until the mouse had fully recovered and was freely moving. Six additional dosages of Temgesic were injected every 8 hours after the operation.

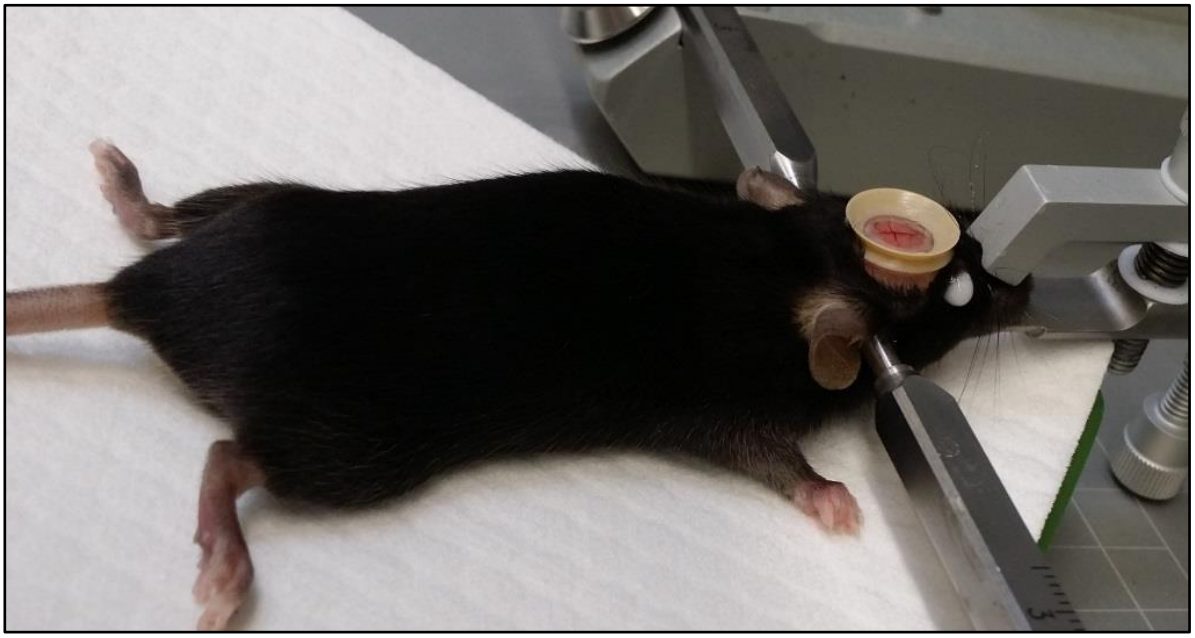

Figure 13: Cranial window preparation.

Mice were fixed on a stereotaxic apparatus, and teeth were fixed using a tooth bar, while two ear bars were also used for fixation of the head. Mouse eyes were protected using eye ointment. As shown, the cranial window was already well-prepared, and the sinus could be visualized through a transparent cranial window. A cranial ring was also pasted on the mouse head for future fixation under the objective of TPLSM.

3.5.2 Intracarotid artery injection

The mice were anesthetized via intraperitoneal (i.p.) injection of MMF (midazolam 5 mg/kg, medetomidine 0.05 mg/kg, and fentanyl 0.5 mg/kg). After a subcutaneous injection of cefotaxime (125 µl 50 mg/ml), the hair was removed from the lower jaw to the manubrium using depilatory cream. The mouse was then fixed on the heating mat and the incision area disinfected with povidone-iodine. A 1-cm longitudinal cut was created slightly to the midline of the neck. Forceps were used to separate the fat and muscle to expose the trachea. The salivary gland was then isolated and covered with gauze. Forceps were used to carefully separate the fascia overlying the artery. The vagus nerve was pulled gently aside from the carotid artery, and forceps were inserted into the intervening space. The vagus nerve was pulled aside, and the common carotid artery was isolated. The isolate external carotid artery was then isolated using 7-0 silk thread (ETHICON, Cat. No. K 803) with a needle and permanently ligate. The common carotid artery was permanently ligated at the anterior side. The common carotid artery was temporarily ligated at the posterior side with a slipknot. Minor forceps were then used to cut a hole on the common carotid artery, which should be close to the anterior ligation position. Thereafter, a self-prepared catheter was inserted into the common carotid artery through the hole. A mini vessel clip (AESCULAP, Tuttlingen Germany) was used to fix the inserted tube, and then silk thread was used to temporarily ligate the inserted part to avoid outflow of the liquid. The ligated threads were temporarily opened, and a back blood phenomenon was typically observed. Then, 7.5×10^5 Lewis lung carcinoma/LL/2/LLc1-Tdt (in 150 µl PBS) tumor cells (concentration 5×10^6/ml) were slowly injected into the common carotid artery in 5 mins. After successful tumor injection, the common carotid artery was permanently ligated at the posterior side and the catheter removed. A certain amount of NACl was applied to the surgical incision to flush the blood and clean the tissue. The skin was sutured followed by a subcutaneous injection of 1 dosage of Temgesic. After 30 minutes, 272 µl Wach was subcutaneously injected to wake the mouse. The mouse was at 1 hour, 3 hours and 6 hours after the operation. Six more dosages of Temgesic were injected every 8 hours after the operation (optimum of 8 hours, 6-12 hours is also acceptable).

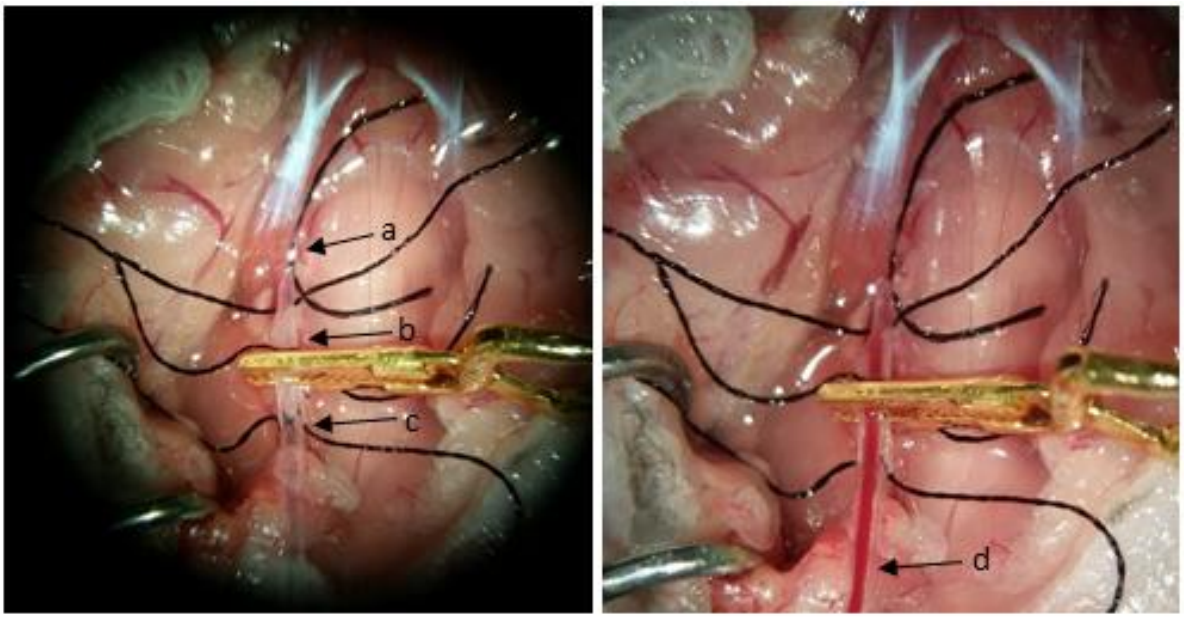

Figure 14: Intracarotid artery injection.

The catheter was successfully injected into the common carotid artery to ensure that the tumor cells travelled only go to the brain through the internal carotid artery via blood flow, the external carotid artery was permanently ligated (a), the vascular clamp was used for fixation (b), and the common carotid artery on the anterior side was permanently ligated to avoid blood flow from the heart. The blood back phenomenon could be observed if surgery was successful (d), and then tumor cells could be injected.

3.5.3 *In vivo* Two-photon Laser Scanning Microscopy (TPLSM)

We used a multiphoton LaVision Biotech TrimScope I system connected to an upright Olympus microscope, equipped with a MaiTai Laser (690-1040 nm) Spectra Physics and a 20× water immersion objective (numerical aperture 0.95, Olympus). Single images were acquired from different depths, depending on different regions, with z-intervals of 2 μm. The excitation wavelength was 920 nm, with 1024 ×1024 pixels, detected by PMTs (G6780-20, Hamamatsu). Imspectro (LaVision Biotech) was used as acquisition software. For cerebral vessel visualization, we injected 0.2 ml 10 mg/ml FITC-dextran (2 M molecular weight, green,

Sigma-Aldrich) through the mouse tail vein. The same regions were followed over time (every two days), which were identified according to their vessel structure. The mouse body temperature was kept constant using a heating pad with a temperature tester. Mice were anesthetized with isoflurane and maintained under a constant flow from 0.8% to 2.0% (as low as possible according to the physical condition of the mouse). The laser power was also limited to the lowest percentage to avoid phototoxicity.

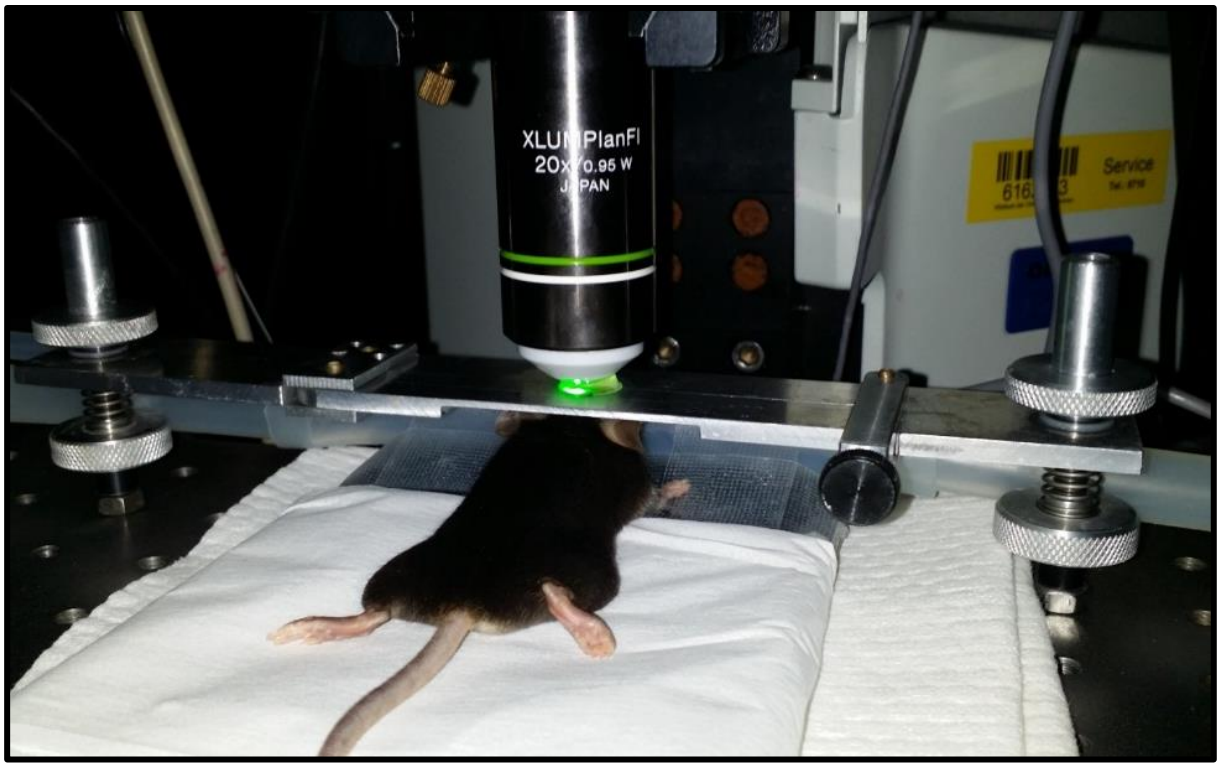

Figure 15: Setup for TPLSM.

The mouse was anesthetized with isoflurane and fixed under the objective of TPLSM with the help of a cranial ring. Body temperature was kept constant using a heating pat under the mouse abdomen. Epi-fluorescence was open at this time; thus, the regions of interest could be visualized under the ocular.

3.5.4 Mouse perfusion

After the mouse was deeply anaesthetized with MMF (midazolam 5 mg/kg, medetomidine 0.05 mg/kg, and fentanyl 0.5 mg/kg) and fixed, the thoracic cavity was opened to expose the

heart.

The right atrial appendage was cut, and blood flowed out. The left apex was punctured with a needle followed by injection of NaCl (0.9%) for approximately 20-50 ml until all the blood was replaced with NaCl, at which time the flow became clear. Next, the mouse was perfused with 4% formalin. In the first few minutes after formalin injection, the mouse exhibited a strong reaction, with shaking legs and tail. Spreading of liquid from the nose indicates an incorrect puncture point going directly to the atrium, and puncture angle should be changed. After perfusion, the organs were harvested. To isolate the brain, the head was separated from the body. The skull was cut through middle line and the line between the two eyes to open the cranial cavity. The whole brain was exposed and then gently peeled away. Organs were collected in 50-ml falcon tubes with 30 ml 4% formalin and stored at 4 ℃.

3.5.5 Organ fixation

After 1-2 hours of storage in 4% formalin, 10%, 20%, and 30% sucrose was used for dehydration. The storage time for different concentration gradients was approximately 24 hours. After fixation in 30% sucrose, the liquid was absorbed on the surface of the brain with soft tissue. Afterwards, the brain was frozen in the liquid nitrogen vapor phase and covered with plastic film and foil paper, which were precooled at -20 ℃ (usually placed in the cutting machine). The brain was then placed in the freezer at -80 ℃.

3.5.6 Frozen brain tissue sections

The brain was removed from the -80 ℃ freezer and placed into the cutting machine. After approximately 30 mins, the temperature had increased to be equivalent to the cutting machine, which was about -20 ℃. Some tissue Tek was applied to the cutting plate, and then the plate was placed in the chamber of the cutting machine until it was solidified. The brain was fixed on the plate with additional tissue Tek. The brain should be vertically standing in the center of

the plate. This process should be done as soon as possible to avoid damage of the freezing brain because of hot fingers. The plate was subsequently fixed on the cutting machine. Then, the section depth was set, typically at 15 µm. Afterwards, the position of the brain was manually regulated until it reached the edge of the cutting knife. After finishing these preparative processes, cutting was started. The exact cutting position was determined based on the mouse brain atlas. After the best cutting position was determined, two slices per slide were collected. The slides were kept at room temperature for approximately 20 mins to dry and then placed in a slide box at -20 ℃ for longer storage.

3.5.7 Imaging processing

After the original data were acquired using two-photon *in vivo* microscopy, all the images were processed in Imaris. To easily distinguish the images, the green channel was replaced with blue color and then merged with the red channel; thus, the colors were manually manipulated as shown in the last image, in which the vessel in silver white, tumor cells are red, and TAMs are sky blue.

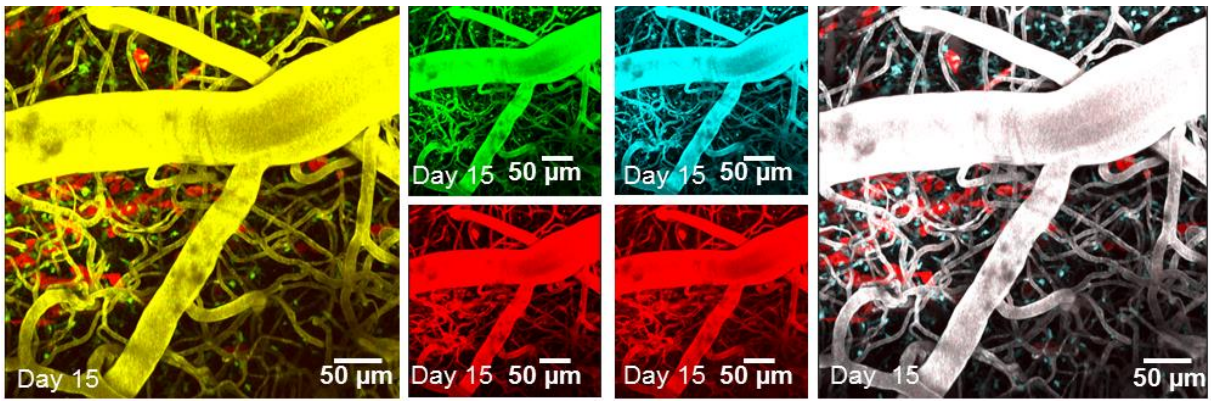

Figure 16: Image processing.

Representative TPLSM shows the image processing. The images in the left column show the merge of green and red channel, the middle column shows the green channel replaced with blue color, and the right column illustrates the merge of these two channels. The last image indicates how the colors were manipulated to clearly distinguish TAMs, tumor cells, and vessels. (Depth, 1-300 µm; Scale bar, 50 µm).

3.5.8 Imaging data analysis

After original images were acquired using Imspector Pro, Bitplane Imaris Software was used for further analysis. To obtain high-quality images, the brightness, contrast, or color balance was regulated manually for the whole image. The density and volume of the TAMs were quantified in a 100 μm × 100 μm × 40 μm three-dimensional region of interest. TAM numbers were calculated semiautomatically using the spots function in Imaris, while the cell body volume of these immune cells was measured through the surface function. Spots were manually added to the cell body, and then cell numbers were calculated. Lines were drawn slice-by-slice around the cell body, and then the three-dimensional structure of the cells was established and the volume calculated. Same regions of interest were chosen on different days according to the vessel structure. The maximum intensity projection (MIP) function was used to obtain 2-dimensional images.

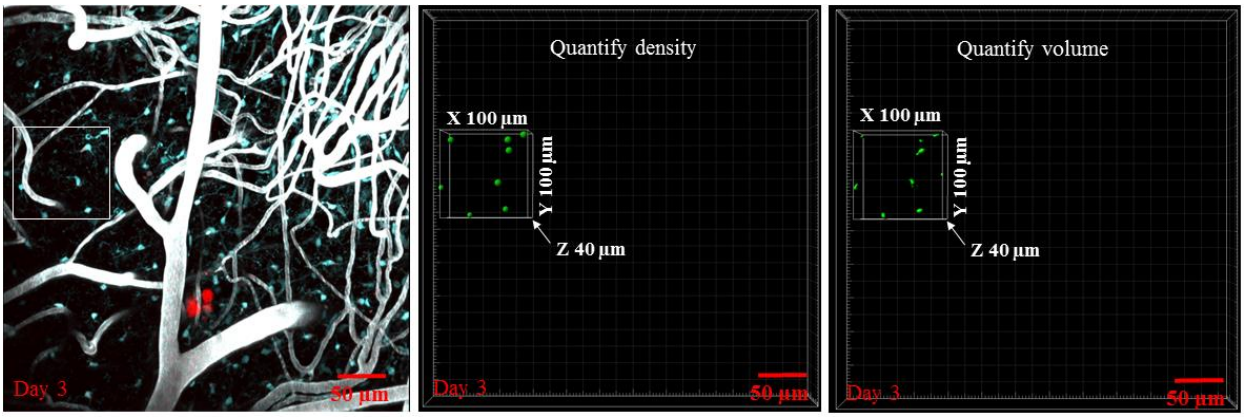

Figure 17: Quantification of both the density and cell body volume of TAMs.

The MIP (left) image indicates the vessels, TAMs and tumor cells. The region of interest was marked in a square box. The number of TAMs in this region (three-dimensional x/y/z 100 μm × 100 μm × 40 μm) was calculated using Imaris software (middle), and the cell body was outlined manually to quantify the cell body volume (right).

3.5.9 Data analysis

Regions of interest (ROI) were randomly selected, and 25% of the data from $CX3CR1^{GFP/GFP}$ were double checked by a colleague in a blinded manner to avoid bias. In $CX3CR1^{GFP/wt}$ mice, n= 17 ROIs for the control, 3 ROIs before single tumor cell arrival, 6 ROIs upon arrival of single tumor cells, 8 ROIs for micrometastasis persistence, 6 ROIs for macrometastasis persistence, and 8 ROIs after micrometastasis regressed regions, were calculated in 8 mice with metastasis and 3 control mice. In $CX3CR1^{GFP/GFP}$ mice, n=18 ROIs for the control, 7 ROIs before single tumor cell arrival, 15 ROIs upon arrival of single tumor cells, 17 ROIs for micrometastasis persistence, 14 ROIs for macrometastasis persistence, and 6 ROIs after micrometastasis regressed, were calculated in 8 mice with metastasis and 3 control mice. GraphPad software was used to analyze all the data. Statistical differences between multiple groups were assessed by the Mann-Whitney-U test. The Chi-square test or Fisher's exact test was used for the metastatic cascade depending on the number of samples; if $n \geq 40$, the Chi-square test was used, and if $n < 40$, Fisher's exact test was used. $P < 0.05$ was regarded as statistically significant.

4 Results

4.1 Stable transfection of the Lewis lung carcinoma/LL/2/LLc-Tdt cell line

To track single metastatic tumor cells in the brain cortex under 2PM, stable fluorescent protein was transfected and expressed in the tumor cell line. Td-tomato was selected considering its brightness and photostability.

Tdtomato consists of two genetically fused dtomato genes and forms an intramolecular dimer in the cytoplasm[116]. This tandem dimer structure plays an important role in the brightness of Tdtomato protein, which makes it an outstanding *in vivo* imaging candidate. Tdtomato is widely used in *in vivo* models, and in a breast cancer metastasis mouse model, tdtomato could be detected as deep as 1 cm below the surface[117].

As Lewis lung carcinoma/LL/2/LLc1-Tdt cells are a semiadherent cell line, lipofection was used to transfect the pLVX-tdTomato-IRES-Neo plasmid carrying the tdtomato sequence. Compared with other transfection strategies such as electroporation, lipofection is easy to perform with high efficiency. One day after lipofection, red fluorescent cells could already be observed under microscopy. To select transfected and nontransfected cells, G418 was used. A concentration gradient assay of G418 showed that 1000 μg/ml was a demarcation point for normal Lewis lung carcinoma/LL/2/LLc1-Tdt cells, representing the highest concentration in which they could survive. Thus, it was used as the selection concentration. Moreover, no morphological nor proliferation differences were observed compared with normal Lewis lung carcinoma/LL/2/LLc1-Tdt cells during *in vitro* cultivation, indicating that Tdtomato plasmid transfection did not change the biological characteristics of Lewis lung carcinoma/LL/2/LLc1-Tdt cells.

To obtain stable and highly fluorescent cells, repeated FACs-sorting was performed. During

each round of sorting, approximately 10% of the cells with the highest fluorescent signal were sorted and subcultured. G418 was also used to maintain the selection pressure. After sorting several times, the Lewis lung carcinoma/LL/2/LLc1-Tdt tumor cells were intracranially injected into the mouse cortex and imaged under 2PM.

4.2 Establishment of the syngeneic cerebral metastasis model (Lewis lung carcinoma/LL/2/LLc1-Tdt cell line)

After obtaining the highly fluorescent red Lewis lung carcinoma/LL/2/LLc1-Tdt tumor cell line, the most important question to be answered was whether these cells would successfully form cerebral macrometastases.

Successful macrometastasis formation could be observed after intracarotid injection of Lewis lung carcinoma/LL/2/LLc1-TdT. In the $CX3CR1^{GFP/wt}$ group, 14 mice were successfully injected with Lewis lung carcinoma cells/LL/2/LLc-Tdt through the intracarotid artery, and 8 mice could be used for *in vivo* TPLSM with a survival of 16.13±3.357 days. In contrast, in the $CX3CR1^{GFP/GFP}$ group, 12 mice were successfully injected with tumor cells, and 8 mice could be used for *in vivo* TPLSM. The survival time for this group was 14.38±2.825 days. Figure 18 indicates how macrometastasis formed over a period of 11 days; one day after intracarotid artery injection, single metastatic tumor cells could be observed outside the vessel. After successful extravasation, tumor cells started to proliferate by cooption of the pre-existing vessels. On day 7, the formation of a micrometastasis could be observed. The tumor cells then aggressively proliferated, leading to the formation of a macrometastasis on day 11. At that time, the vessel structure (dilated vessel diameter, tortuous vessel, nonhierarchical vessel architecture) was indicative of angiogenic changes.

These results suggest that the single steps of cerebral metastasis formation could be visualized after intracarotid injection of Lewis lung carcinoma/LL/2/LLc1-TdT through the chronic

cranial window by using TPLSM, laying a solid foundation for research designed to investigate the interactions between metastatic tumor cells and TAMs.

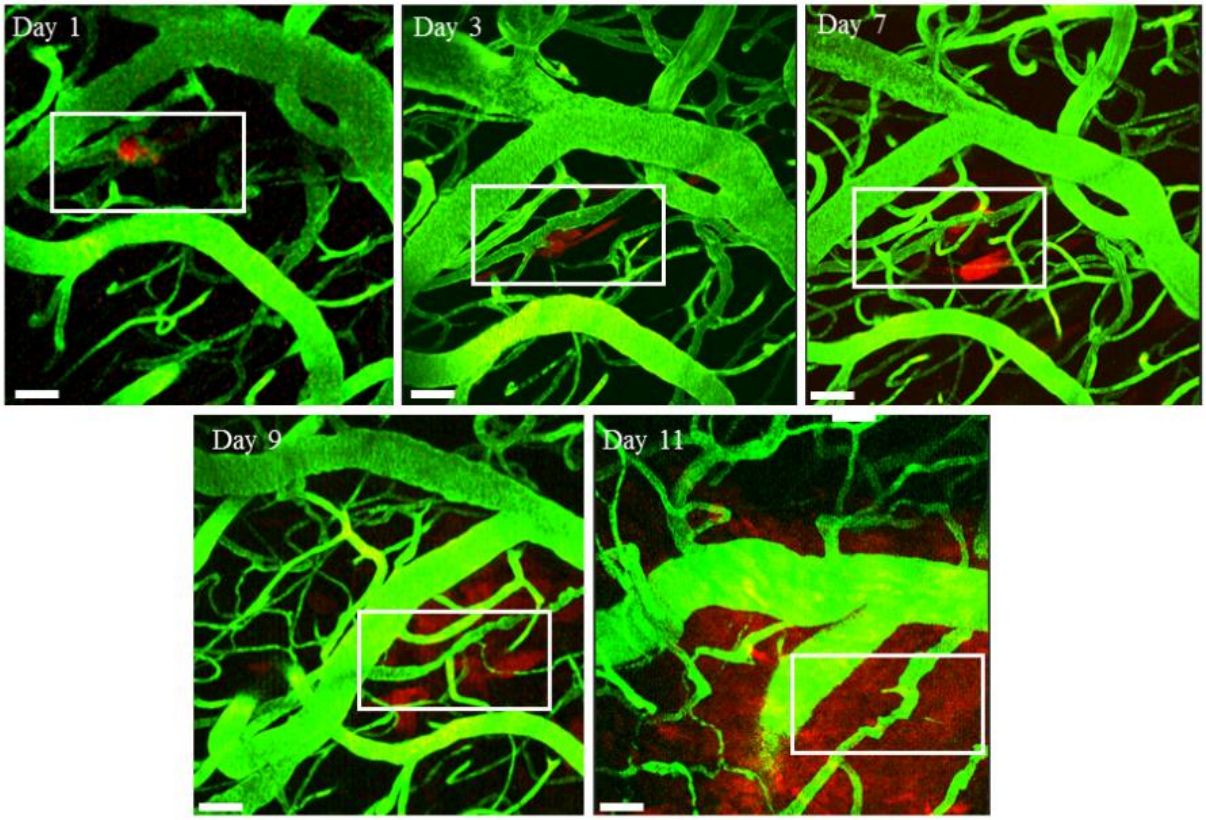

Figure 18: Two-photon microscopy of macrometastasis formation after intracarotid artery injection of Lewis lung carcinoma/LL/2/LLc1-Tdt cells.

Successful Lewis lung carcinoma/LL/2/LLc1-Tdt cerebral macrometastasis formation within 11 days. In the first 7 days, Lewis lung carcinoma/LL/2/LLc-Tdt cells (red) were located in the perivascular location. From day 9 forward, the cell cluster proliferated by cooption of existing vessels (green after i.v. injection of FITC-dextran). Depth: 0-50 µm, the rectangle shows the corresponding region, scale bar, 50 µm.

4.3 Visualization of TAMs and the vasculature in CX3CR1$^{GFP/wt}$ mice

To visualize microglia/macrophages in the process of cerebral metastasis formation, transgenic CX3CR1^{GFP} mice were used. Figure 19 shows an example of TPLSM in CX3CR1$^{GFP/wt}$ mice through the chronic cranial window.

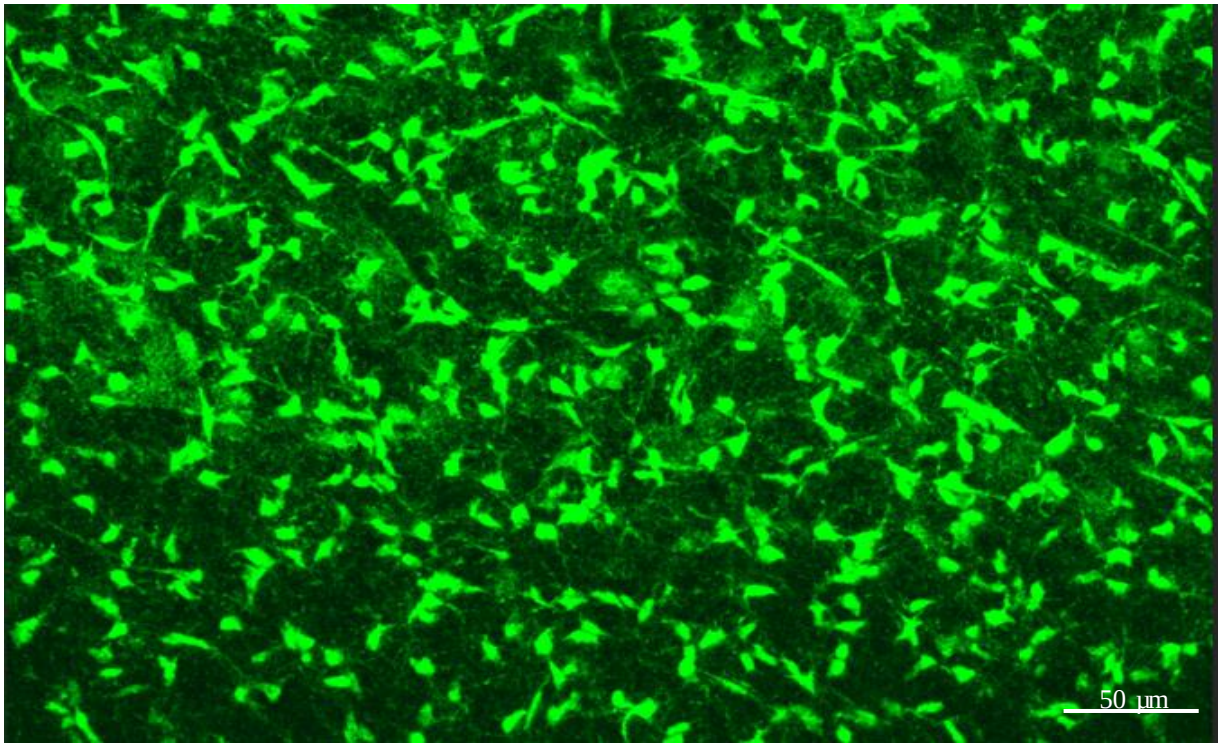

Figure 19: TPLSM of microglia/macrophages in the CX3CR1$^{GFP/wt}$ mouse brain. As seen from the image, microglia/macrophages were evenly distributed in the mouse brain parenchyma, and these resident microglia/macrophages exhibited a small cell body and many processes. The morphology of microglia/macrophages was heterogeneous, with some exhibiting an ellipsoid and others a longitudinal morphology. Depth: 0-200 µm.

To track metastatic tumor cells in different steps of cerebral metastasis formation, especially in the early steps: before and after extravasation, the vasculature should also be labeled. FITC-dextran was used for *in vivo* vasculature staining.

After FITC-dextran injection through the tail vein, both TAMs and the vasculature could be visualized. As shown in the following image, under normal physiological conditions, microglia exhibited a small cell body and many long branching processes (Figure 20). Moreover, the vessels could act as a landmark. The same region in mouse brain could be followed over time for a period of weeks. Accordingly, parameter changes, such as

morphology, density, and cell body volume of TAMs, could be obtained.

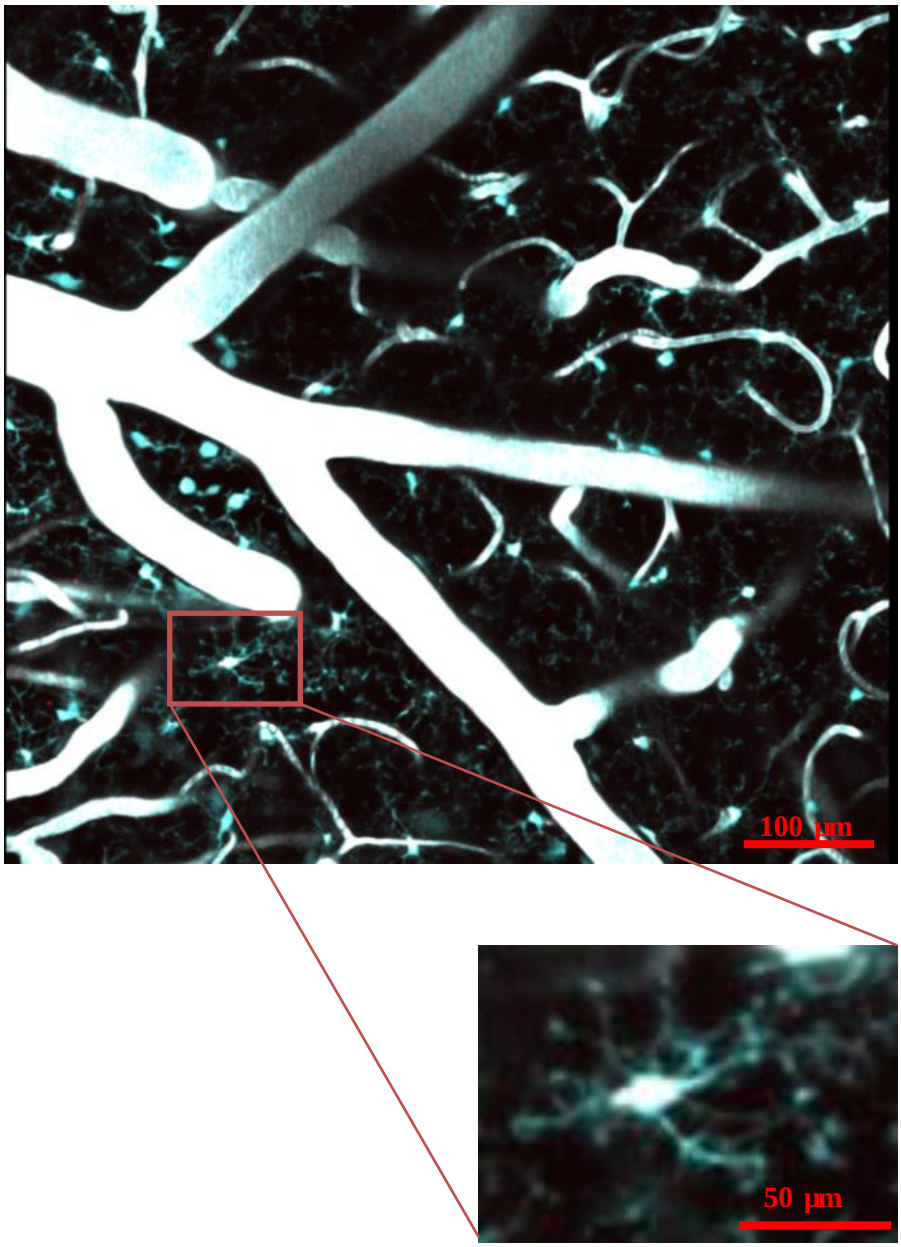

Figure 20: Microglia/macrophages and vessels in CX3CR1$^{GFP/wt}$ mouse brain.

Microglia/macrophages and vessels were visualized simultaneously in the mouse brain cortex. Resident microglia are highlighted in the lower row with a small cell body and long processes. Depth: 38-56 µm, scale bar, 100 µm (up row) and 50 µm (lower row).

4.4 Successful macrometastasis formation of Lewis lung carcinoma/LL/2/LLc1-TdT cells in CX3CR1$^{GPF/wt}$ and CX3CR1$^{GPF/GFP}$ mice

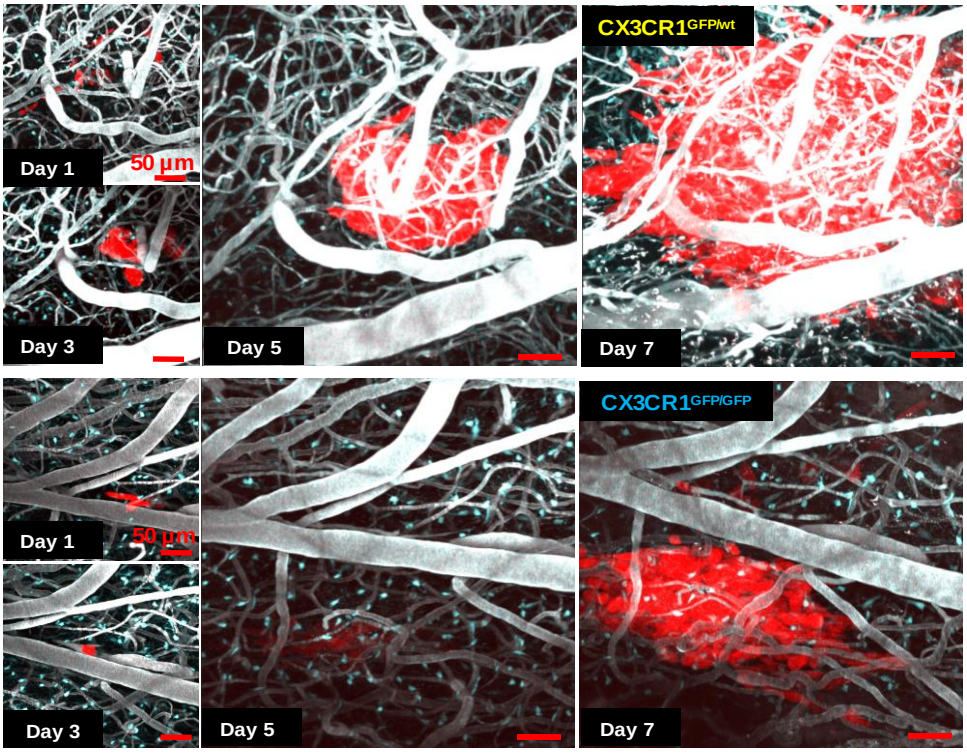

Figure 21: Successful macrometastasis formation of Lewis lung carcinoma/LL/2/LLc1-Tdt in CX3CR1$^{GFP/wt}$ and CX3CR1$^{GFP/GFP}$ mice.

Representative *in vivo* TPLSM images showing macrometastasis formation after single Lewis lung carcinoma/LL/2/LLc1-Tdt cells (red) were arrested in the brain of CX3CR1$^{GFP/wt}$ and CX3CR1$^{GFP/GFP}$ mice. Vessels are highlighted in silver white after i.v. injection of FITC-dextran, while TAMs are shown in bright blue (Scale bar, 50 µm). All images are shown as maximum intensity projections with dimensions of 450 µm × 450 µm × 200 µm (x/y/z). One day after intracarotid artery injection, single tumor cells were located in the brain and then rapidly proliferated and formed micrometastases on day 3 and day 5, respectively. They then continued to grow to form macrometastases on day 7.

One day after intracarotid artery injection of Lewis lung carcinoma/LL/2/LLc1-Tdt cells, only single tumor cells could be detected in the brain cortex both in CX3CR1$^{GFP/wt}$ and

CX3CR1$^{GFP/GFP}$ mice. These single tumor cells then rapidly proliferated and grew to form a solid tumor cluster with close cell-cell contacts and associations with the pre-existing vasculature. Micrometastases were already formed on day 3 and day 5 in CX3CR1$^{GFP/wt}$ and CX3CR1$^{GFP/GFP}$ mice, respectively. Thereafter, these micrometastases continued to grow, and a macrometastasis was formed on day 7. At this time point, single tumor cells were observed distant from the main tumor site, reflecting the histopathological growth pattern of advanced metastasizing tumor cells in the brain cortex.

In addition to elucidating the pattern of metastasizing tumor growth via chronic two-photon imaging of CX3CR1$^{GFP/wt}$ and CX3CR1$^{GFP/GFP}$ mice, the interactions between TAMs and metastasizing tumor cells could also be determined, as seen in the images. Single TAMs had different colors than tumor cells; thus, both the density and cell body volume of TAMs could be analyzed in the region of interest.

4.5 Unsuccessful micrometastasis formation of Lewis lung carcinoma/LL/2 /LLc1-Tdt cells in CX3CR1$^{GPF/wt}$ and CX3CR1$^{GPF/GFP}$ mice

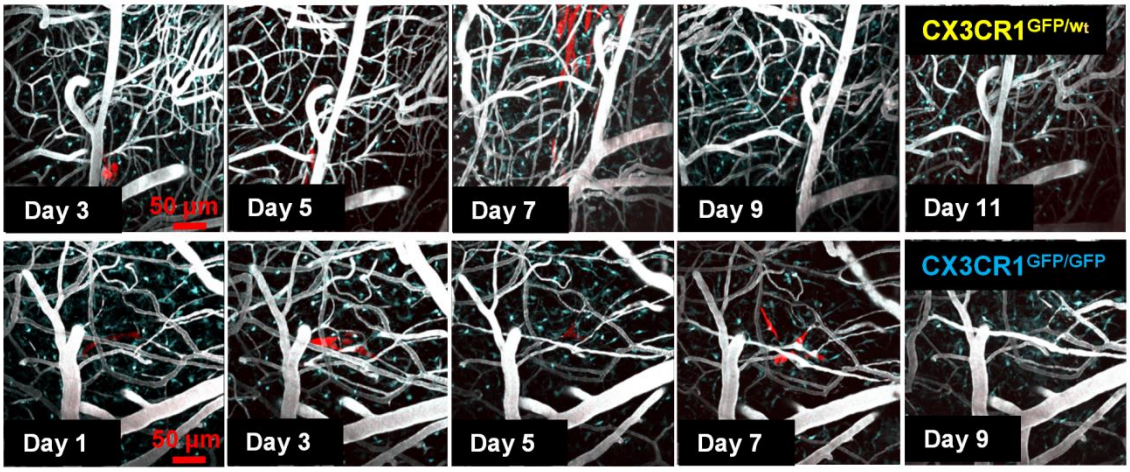

Figure 22: Unsuccessful micrometastasis formation of Lewis lung carcinoma/LL/2/LLc1-Tdt in CX3CR1$^{GFP/wt}$ and CX3CR1$^{GFP/GFP}$ mice.

The TPLSM images illustrate regressing Lewis lung carcinoma/LL/2/LLc1-Tdt cell (red) micrometastasis

in CX3CR1$^{GFP/wt}$ and CX3CR1$^{GFP/GFP}$ mice. All images are shown as maximum intensity projections with dimensions of 450 µm × 450 µm (x/y) and a z depth of 1-100 µm and 20-60 µm, respectively. In the CX3CR1$^{GFP/wt}$ group, a micrometastasis was formed on day 7 from single metastatic tumor cells on day 3. Afterwards, this micrometastasis started to regress, and no tumor cells could be observed on day 11. Similarly, in the CX3CR1$^{GFP/GFP}$ group, metastatic tumor cells persisted in brain from day 1 to day 7 and regressed on day 9.

Not all the Lewis lung carcinoma/LL/2/LLc1-Tdt cells we detected could successfully form a macrometastasis. We also observed micrometastasis regression before macrometastasis formation both in CX3CR1$^{GFP/wt}$ and CX3CR1$^{GFP/GFP}$ mice. Initially, single metastasizing tumor cells were located in the small capillary of the cortex (day 3 and day 1 in CX3CR1$^{GFP/wt}$ and CX3CR1$^{GFP/GFP}$, respectively) and then proliferated through the cooption of pre-existing vessels to a micrometastasis on day 7. Afterwards, instead of continuing to grow, these micrometastases started to regress, and in CX3CR1$^{GFP/wt}$ mice, only one cell could be observed after 2 days with complete tumor regression on day 11. In CX3CR1$^{GFP/GFP}$ mice, the micrometastasis was already regressed on day 9.

Moreover, as TAMs could be clearly distinguished from metastasizing tumor cells throughout the whole process of micrometastasis regression, the interactions between TAMs and metastasizing tumor cells during the process of unsuccessful micrometastasis formation could also be investigated. By analyzing both the density and cell body volume of TAMs over time in the regions of interest in regressing micrometastases, parameter changes could be determined.

4.6 Density and cell body volume changes of TAMs in different steps of cerebral metastasis formation

After obtaining images by TPLSM in different steps of cerebral metastasis formation, both the density and cell body volume of TAMs were quantified in regions of interest over time in

normal CX3CR1$^{GFP/wt}$ mice and in deficient CX3CR1$^{GFP/GFP}$ mice, with a total of 8 mice per group successfully injected with Lewis lung carcinoma/LL/2/LLc1-Tdt cells and used for chronic *in vivo* microscopy and quantification.

Before single tumor cell arrival, both the density and cell body volume of TAMs remained at a stable level both in normal CX3CR1$^{GFP/wt}$ mice and in deficient CX3CR1$^{GFP/GFP}$ mice. After the arrival of metastasizing tumor cells, these parameters significantly increased in both mouse strains. During tumor proliferation, both parameters also rose; however, after tumor regression, both the density and cell body volume of the TAMs decreased. Compared with the control group mice, there were significantly differences in each step of cerebral metastasis formation in both mice strains.

These results indicated that both the density and cell body volume of TAMs were influenced by metastatic tumor cells in different steps of cerebral metastasis formation.

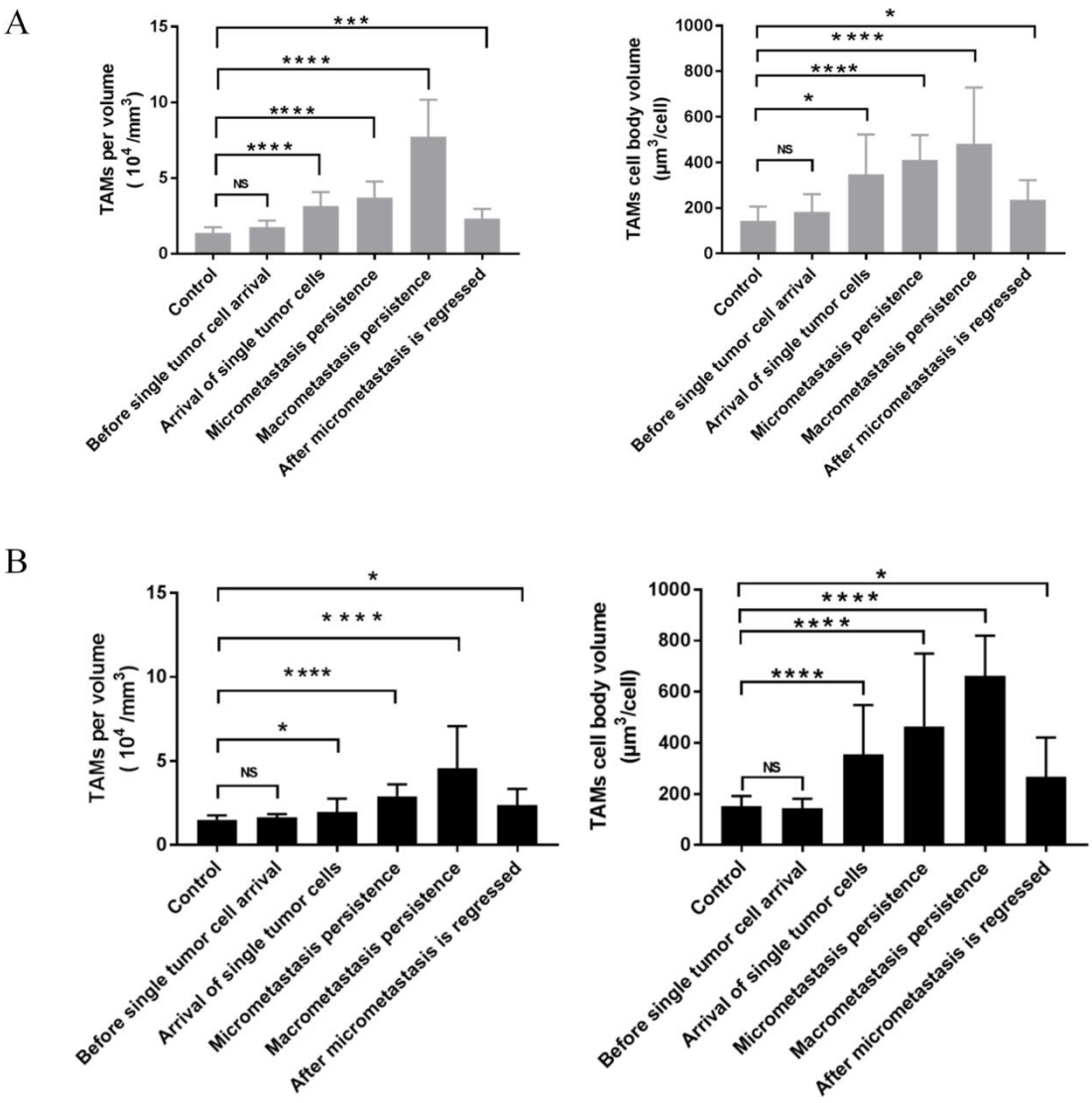

Figure 23: Density and cell body volume changes of TAMs in different steps of cerebral metastasis formation of Lewis lung carcinoma/LL/2 /LLc1-Tdt cells in CX3CR1$^{GFP/wt}$ and CX3CR1$^{GFP/GFP}$ mice.

A. Density and cell body volume changes of TAMs in different steps of cerebral metastasis formation in 8 CX3CR1$^{GFP/wt}$ mice and in 3 CX3CR1$^{GFP/wt}$ control mice (region of interest (ROI): n=17 ROIs for the control animals, 3 ROIs before single tumor cell arrival, 6 ROIs upon arrival of single tumor cells, 8 ROIs showing micrometastasis persistence, 6 ROIs showing macrometastasis persistence, 8 ROIs after micrometastasis regression (two-tailed Mann-Whitney-U test, *P<0.05, **P<0.01, ***P<0.001, ****P<0.0001; error bars indicate SD).
B. Comparison of the density and cell body volume of TAMs in different steps of cerebral metastasis formation in CX3CR1$^{GFP/GFP}$ mice (n=18 ROIs for the control, 7 ROIs before single tumor cell arrival, 15 ROIs upon arrival of single tumor cells, 17 ROIs showing micrometastasis persistence, 14 ROIs showing macrometastasis persistence, 6 ROIs after micrometastasis regression, calculated in 8 mice

with metastasis and 3 control mice). (Two-tailed Mann-Whitney-U test, *P<0.05, **P<0.001, ***P<0.0001, ****P<0.0001; error bars indicate SD).

4.7 Close contact between TAMs and metastasizing carcinoma/LL/2/LLc1-Tdt cells in early steps of cerebral metastasis in CX3CR1$^{GPF/wt}$ and CX3CR1$^{GFP/GFP}$ mice

No differences were observed between CX3CR1$^{GFP/wt}$ and CX3CR1$^{GFP/GFP}$ mice in the early steps of cerebral metastasis. One day after intracarotid artery injection, single metastatic Lewis lung carcinoma/LL/2/LLc1-Tdt lung carcinoma cells (Figure 24) were arrested at the branch point of small capillary, and the TAMs showed close contact with this arresting branch point. Afterwards, on day 3, the tumor cells seemed to be trying to escape from the vasculature. Then, on day 5, single tumor cells had already successfully completed extravasation. However, instead of continuing to grow after extravasation, these tumor cells were phagocytosed by TAMs. On day 9, no tumor cells could be observed. These images indicated that the TAMs could exert engulfment functions for metastasizing tumor cells after extravasation. Therefore, during the early steps of cerebral metastasis, innate responses mediated by TAMs were beneficial and involved the activation of effective surveillance and tumoricidal effects, resulting in the elimination of single metastasizing cells.

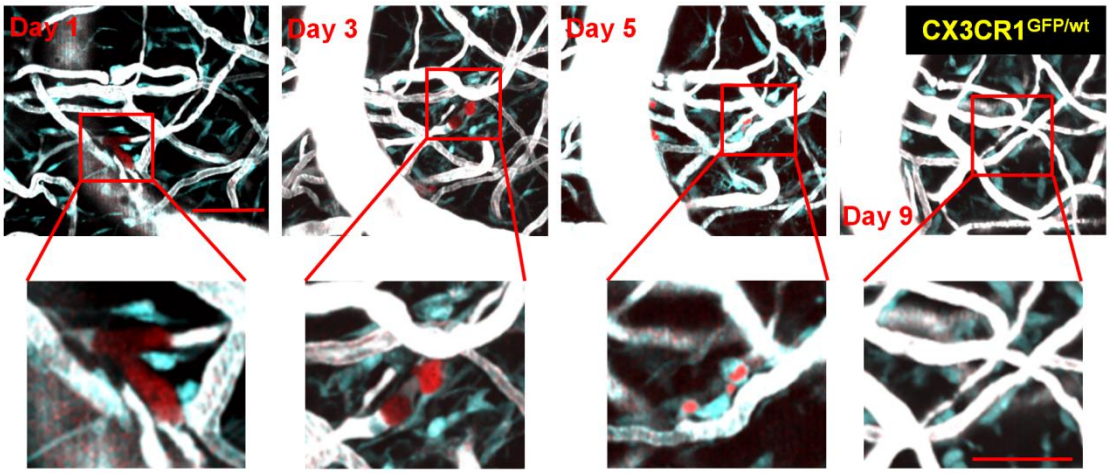

Figure 24: Single metastatic Lewis lung carcinoma/LL/2/LLc1-Tdt lung carcinoma cells are phagocytosed

by TAMs.

An individual metastatic tumor cell (red) was phagocytosed by TAMs (bright blue) after extravasation (magnification shows TAM changes before and after extravasation; depth, 14-30 μm; scale bar, 50 μm).

An interesting phenomena from CX3CR1$^{GFP/GFP}$ mice, as seen in the images (Figure 25 A), revealed a red single tumor cell located in an intravascular position over a period of 5 days, and the arresting position changed slightly, potentially because of the blood flow. The three TAMs that were located the closest to this metastasizing cell were marked. During these 7 days, no changes in the morphology or density of the TAMs were observed, which indicated that the TAMs remained in a relatively stable state while metastasizing tumor cells were located in an intravascular position.

Another interesting phenomenon we observed in CX3CR1$^{GFP/GFP}$ mice was the close contact between TAMs and metastasizing tumor cells during the early steps of cerebral metastasis formation. As shown in the figure (25 B), on day 3 and day 5, single tumor cells were located at the branch point of the small capillary in brain cortex. On day 5, the blood brain barrier was destroyed, as small parts of the tumor cells appeared to be outside of the vasculature. Seven days after intracarotid artery injection, the tumor cells had already disappeared. At this time point, the vasculature displayed a pathological condition, as the diameter of the small capillary was enlarged. Moreover, the size of the TAMs was also increased, and they exhibited close contact with the pathological vessels. From day 9 to day 13, the cell body volume of the TAMs generally decreased with a low density in the region of interest.

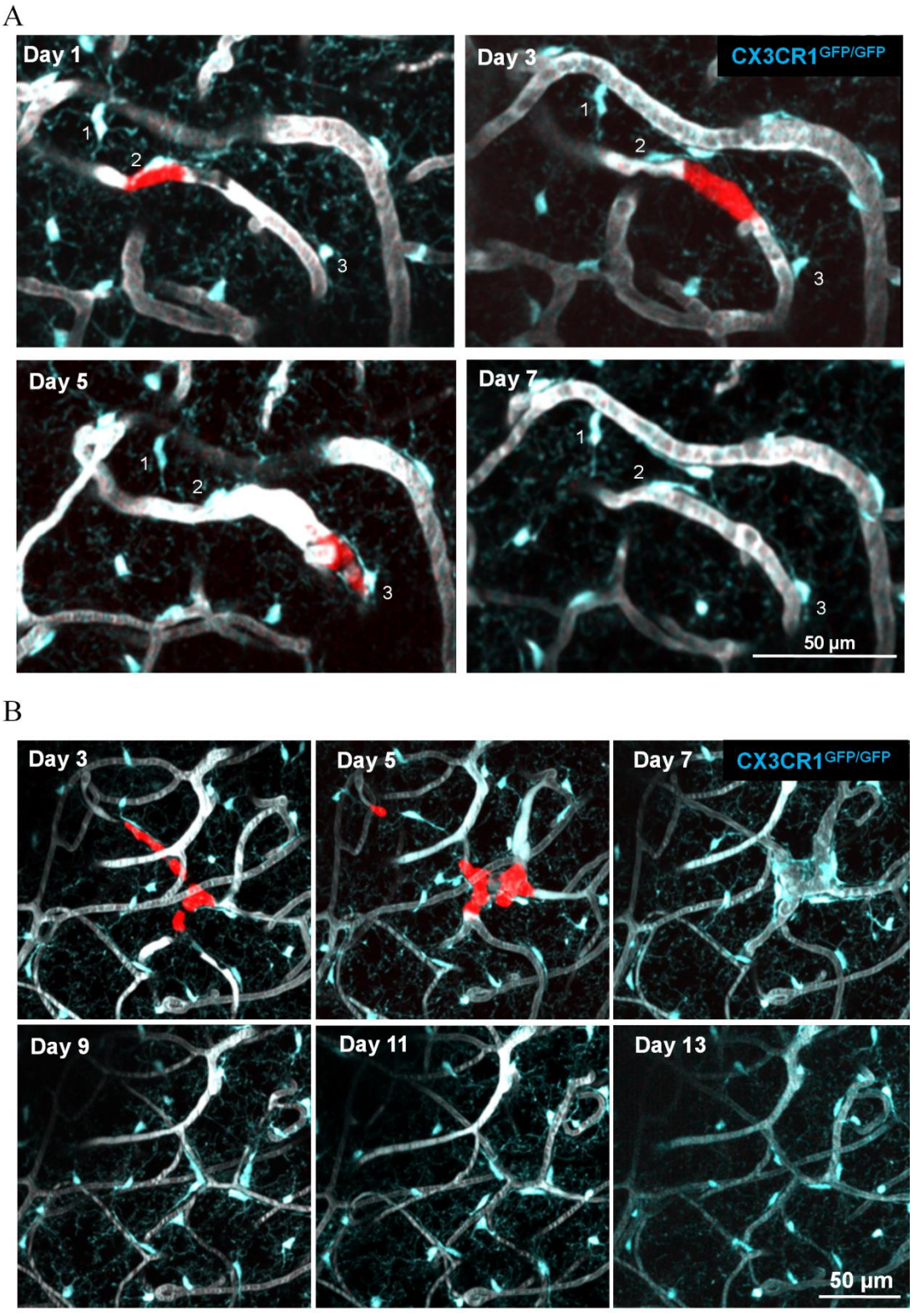

Figure 25: Interactions between TAMs and metastasizing Lewis lung carcinoma/LL/2/LLc1-Tdt lung carcinoma cells in the early steps of cerebral metastasis formation in CX3CR1$^{GFP/GFP}$ mice.

A. TAMs (highlighted by numbers 1/2/3, remained stable over a period of 5 days when the tumor cells were arrested in an intravascular location in CX3CR1$^{GFP/GFP}$ mice (depth, 160-210 μm; scale bar, 50 μm).
B. Pathological vessel structure and morphological and density changes of TAMs were observed before and after single metastasizing Lewis lung carcinoma/LL/2 /LLc1-Tdt tumor cells were arrested at the branch point of the small cerebral capillary (depth, 100-150 μm; scale bar, 50 μm).

4.8 Resting TAMs retain a stable state both in CX3CR1$^{GPF/wt}$ and CX3CR1$^{GPF/GFP}$ mice

To compare the density and cell body volume of TAMs in metastatic tumor lesions and normal resting TAMs, cranial window were prepared using control CX3CR1$^{GFP/wt}$ and deficient CX3CR1$^{GFP/GFP}$ mice without tumor implantation.

The TPLSM images showed that the resting TAMs were relatively stable, without apparent migration or activation both in normal CX3CR1$^{GFP/wt}$ and homozygous CX3CR1$^{GFP/GFP}$ mice.

After acquiring all of these images, both the density and cell body volume of the microglia/macrophages were analyzed. As seen from the bar graph, both parameters remained at a stable level in both mouse strains. Further, there were no statistically significant differences between normal CX3CR1$^{GFP/wt}$ and homozygous CX3CR1$^{GFP/GFP}$ mice, which indicated that both the density and cell bodies of resting microglia/macrophages in CX3CR1$^{GFP/wt}$ and CX3CR1$^{GFP/GFP}$ were similar and remained at a stable level.

A

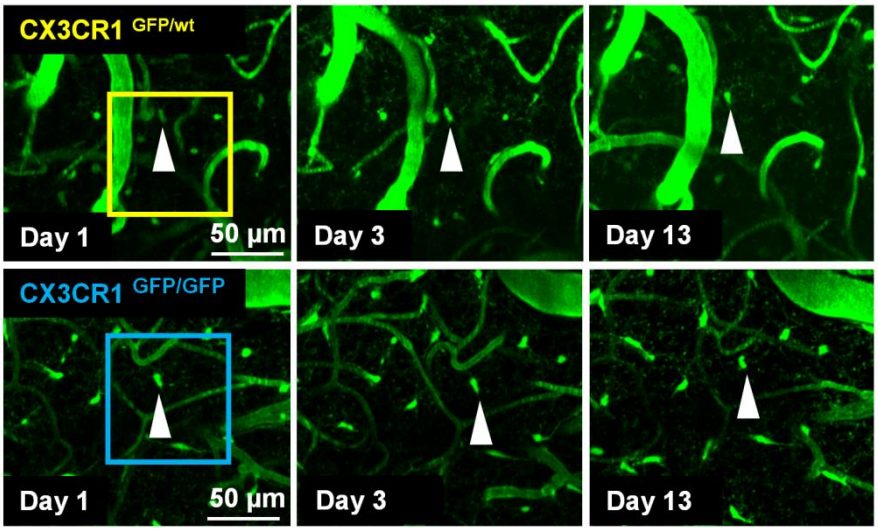

B

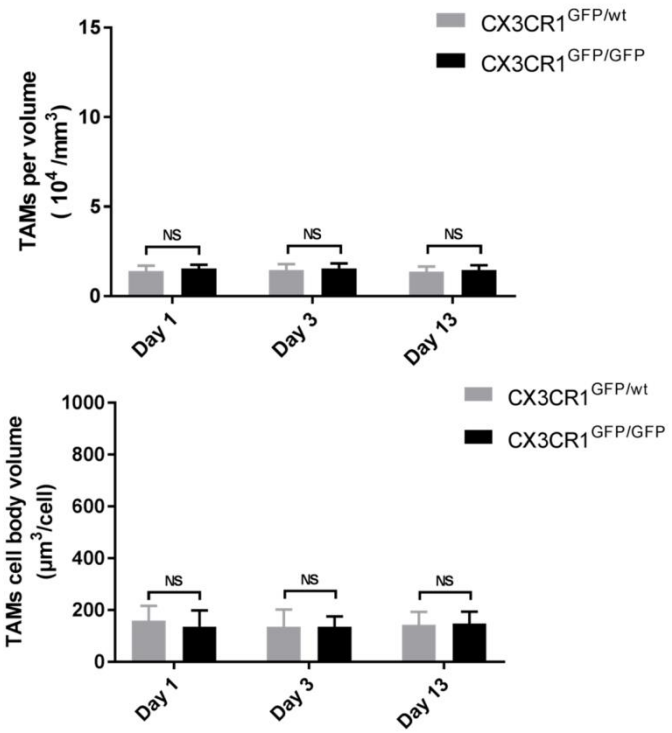

Figure 26: Resting microglia/macrophages in CX3CR1$^{GFP/wt}$ and CX3CR1$^{GFP/GFP}$ mice.

A. Two examples obtained using fluorescence two-photon *in vivo* images, illustrating the small cell bodies and low motility of resting microglia/macrophages both in CX3CR1$^{GFP/wt}$ and CX3CR1$^{GFP/GFP}$ mice. (depth, 40-80 µm; scale bar, 50 µm).

B. Quantification of the density and cell body volume of resting microglia/macrophages in CX3CR1$^{GFP/wt}$ and CX3CR1$^{GFP/GFP}$ mice.

4.9 Comparison of the density and cell body volume of TAMs in micrometastases in CX3CR1$^{GPF/wt}$ and CX3CR1$^{GPF/GFP}$ mice

To further investigate the role of the CX3CR1 receptor in cerebral metastasis formation, both the density and cell body volume of TAMs were quantified and the regions of interest analyzed in both mice strains.

Representative TPLSM images of the micrometastasis illustrate that more TAMs were present in tumor lesions in normal CX3CR1$^{GFP/wt}$ than CX3CR1$^{GFP/GFP}$ mice. To confirm this finding, the TAM density in the micrometastasis tumor mass was quantified in 3D using Imaris. We calculated the density of TAMs in metastasizing micrometastasis in all mice that were successfully followed using two-photon microscopy, in both normal CX3CR1$^{GFP/wt}$ and CX3CR1 deficient mice. Despite the absence of significant differences between the two groups, a trend was apparent, that is, the density of TAMs in the micrometastasis was higher in normal CX3CR1$^{GFP/wt}$ compared with homozygous CX3CR1-deficient mice (Figure 27 CX3CR1$^{GFP/wt}$ $(3.72\pm1.04)\times10^4$ /mm^3 VS CX3CR1$^{GFP/GFP}$ $(2.91\pm0.70)\times10^4$ /mm^3; P= 0.0532 >0.05, no significance, Mann-Whitney U test).

The cell body volume of TAMs correlated with their activation degree[118]. Resting microglia usually formed a small cell body, and once activated, the cell body became enlarged. Thus, the cell body volume serves as a representative parameter for the activation of microglia. To further investigate whether CX3CR1 receptor also affected the activation degree of TAMs, the cell body volume of TAMs in regions of interest was quantified.

Comparing the two different mouse strains: CX3CR1$^{GFP/wt}$ and CX3CR1$^{GFP/GFP}$, no apparent differences were observed in the TPLSM images. To further investigate this finding, the cell body volume data were quantified and analyzed in more details using Imaris. The data showed similar results, in which the cell body volume of TAMs were similar in both normal

CX3CR1 $^{GFP/wt}$ and deficient CX3CR1$^{GFP/GFP}$ mice in the micrometastasis (Figure 27 CX3CR1$^{GFP/wt}$ 411.6±109 μm^3/cell VS CX3CR1$^{GFP/GFP}$ 465.0±284.2 μm^3/cell; P=0.07108>0.05, no significance, Mann-Whitney U test).

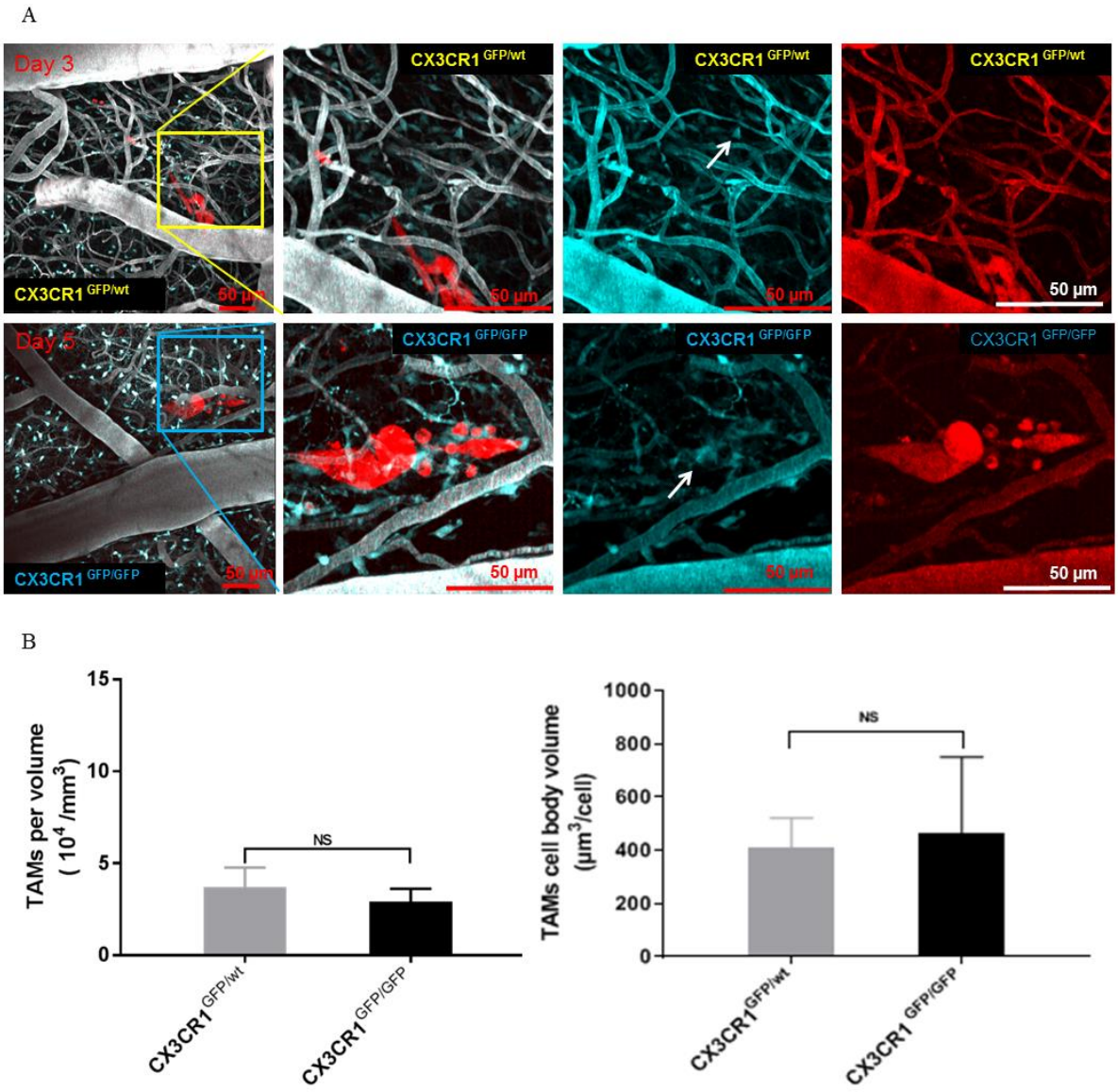

Figure 27: Comparison of the density and cell body volume of TAMs in the micrometastasis in CX3CR1$^{GFP/wt}$ and CX3CR1$^{GFP/GFP}$ mice.

A. Fluorescent MPLSM images were used to compare TAMs in the micrometastasis in CX3CR1$^{GFP/wt}$ and CX3CR1$^{GFP/GFP}$ mice. Magnification of the images highlights the corresponding regions in blue and red channels, and the arrowhead indicates representative TAMs (depth, 0-200 μm in the left column, 0-40 μm in the middle and right column; scale bar, 50 μm).

B. Calculation of the TAMs density and volume in the micrometastasis of CX3CR1$^{GFP/wt}$ and CX3CR1$^{GFP/GFP}$ mice. Eight mice were used for the calculation in each group, and 8 and 17 regions were quantified in the CX3CR1$^{GFP/wt}$ and CX3CR1$^{GFP/GFP}$ group, respectively.

4.10 Comparison of the density and cell body volume of TAMs in macrometastases in CX3CR1$^{GPF/wt}$ and CX3CR1$^{GPF/GFP}$ mice

Both parameters of TAMs were analyzed not only in micrometastases but also in macrometastases. Images of the macrometastases were acquired using TPLSM, and then the density of TAMs in regions of interest was analyzed using Imaris. The images revealed more TAMs in macrometastases in normal CX3CR1$^{GFP/wt}$ than deficient CX3CR1$^{GFP/GFP}$ mice, which became even more evident when only one channel was highlighted, as shown in the figure (28). Furthermore, the calculated data from 8 mice for the two mouse strains repeatedly confirmed the results showing that the density of TAMs in macrometastases was significantly higher in normal CX3CR1$^{GFP/wt}$ than in deficient CX3CR1$^{GFP/GFP}$ mice (Figure 28 CX3CR1$^{GFP/wt}$ $(7.719 \pm 2.444) \times 10^4$ /mm^3 VS CX3CR1$^{GFP/GFP}$ $(4.564 \pm 2.515) \times 10^4$ /mm^3; P= 0.0045<0.05, significance, Mann-Whitney U test).

These results indicate that the CX3CR1 receptor influenced the number of TAMs that infiltrated in the micrometastasis and macrometastasis.

Similar to micrometastases, the cell body volume of TAMs recruited to macrometastases was also calculated. Quantification of the results showed no statistically significant difference between CX3CR1$^{GFP/wt}$ and CX3CR1$^{GFP/GFP}$ mice (Figure 28 CX3CR1$^{GFP/wt}$ 481.3 ± 247.8 μm^3/cell VS CX3CR1$^{GFP/GFP}$ 662.7 ± 157.2 μm^3/cell; P= 0.0698>0.05, no significance, Mann-Whitney U test).

These results illustrated that the cell body volume of TAMs recruited into growing metastases, which could be used as a measure for activation, did not differ between CX3CR1$^{GFP/GFP}$ and

$CX3CR1^{GFP/WT}$ mice.

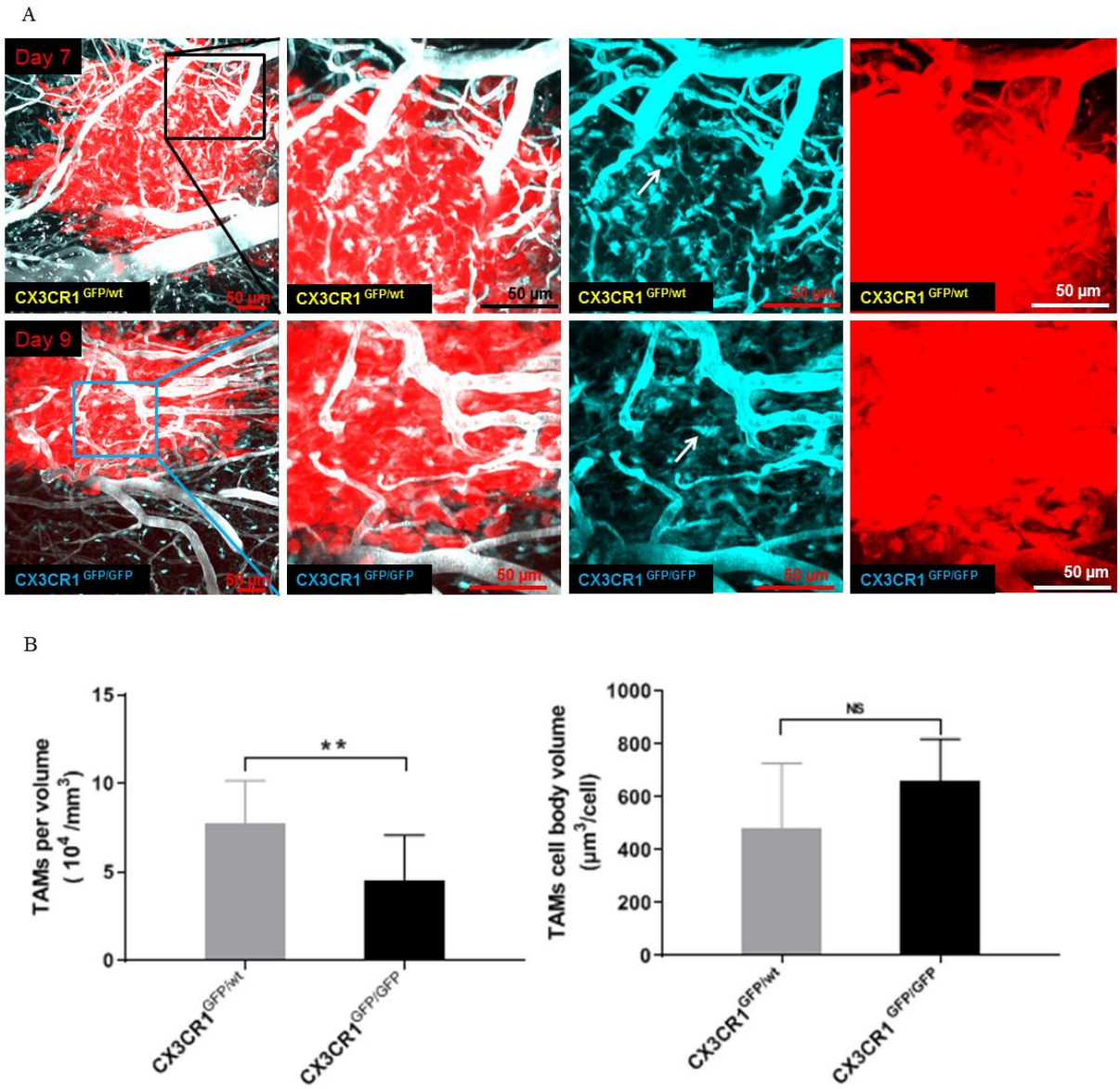

Figure 28: Comparison of the density of TAMs in macrometastases in $CX3CR1^{GFP/wt}$ and $CX3CR1^{GFP/GFP}$ mice.

A. Fluorescence TPLSM images showing TAMs in macrometastases of $CX3CR1^{GFP/wt}$ and $CX3CR1^{GFP/GFP}$ mice. Magnification of the images shows TAMs in the corresponding regions, and arrowhead indicates single TAMs (depth, 0-200 µm in the left column, 60-100 µm in the right and middle column; scale bar, 50 µm).
B. Quantification of the TAMs density and cell body volume in macrometastases of $CX3CR1^{GFP/wt}$ and $CX3CR1^{GFP/GFP}$ mice. The macrometastasis results were from 8 mice per group, and 6 and 14 regions

were quantified in the CX3CR1$^{GFP/wt}$ and CX3CR1$^{GFP/GFP}$ group, respectively (two-tailed Mann-Whitney-U test, **P<0.01; error bars indicate SD).

4.11 Comparison of the density and cell body volume of TAMs during different steps of cerebral metastasis formation

In addition to the density and cell body volume of TAMs quantified in micrometastases and macrometastases, they were also calculated in other steps of cerebral metastasis formation. As shown in the figure (29), before single tumor arrival, the density of TAMs was similar in the two mouse strains, without a significant difference. However, after the arrival of single tumors, significantly more TAMs were observed to infiltrate into the metastatic tumor lesions. Additionally, in the micrometastases to macrometastases, a greater number of TAMs were infiltrated into the tumor mass in CX3CR1$^{GFP/wt}$ than CX3CR1$^{GFP/GFP}$ mice.

This finding indicated that the absence of CX3CR1 influenced the number of TAMs that had infiltrated into the metastasizing tumor lesion in different steps of cerebral metastasis formation.

In contrast to the results obtained for the TAM density in metastasizing tumor lesions, the cell body volume of TAMs was similar in all steps of cerebral metastasis formation in CX3CR1$^{GFP/wt}$ and CX3CR1$^{GFP/GFP}$ mice. No statistically differences could be detected concerning the cell body volume of TAMs during different steps of cerebral metastasis formation.

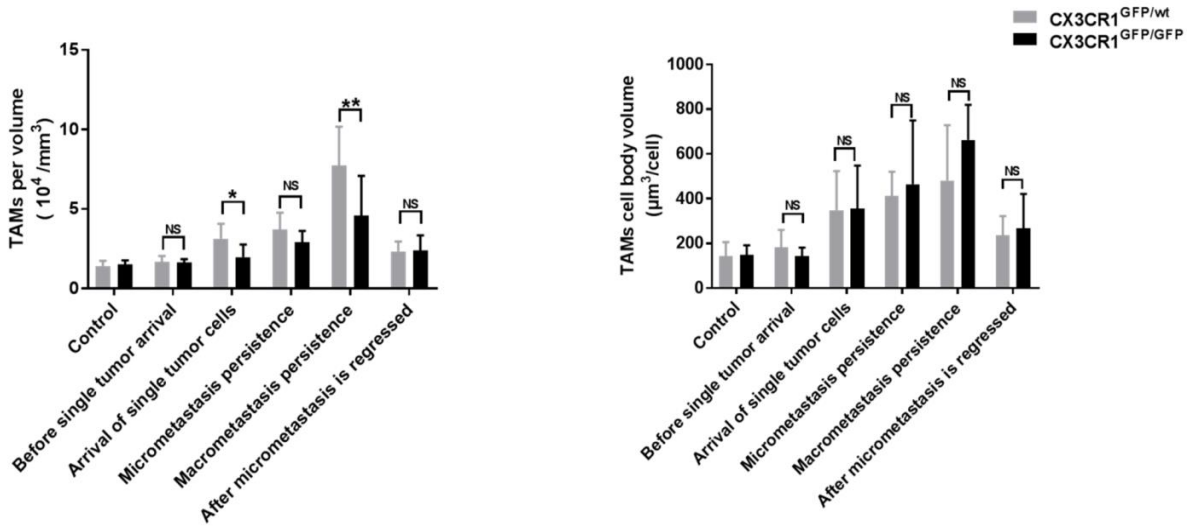

Figure 29: Comparison of the density and cell body volume of TAMs in different steps of cerebral metastasis formation.

The left bar graph indicates the density of TAMs in different steps of cerebral metastasis formation, while the right bar graph shows the cell body volume. (In CX3CR1$^{GFP/wt}$ mice: n=17 ROIs for the control, 3 ROIs before single tumor cell arrival, 6 ROIs upon arrival of single tumor cells, 8 ROIs for micrometastasis persistence, 6 ROIs for macrometastasis persistence, 8 ROIs after micrometastasis regression, calculated in 8 mice with metastasis and 3 control mice; in CX3CR1$^{GFP/GFP}$ mice: n=18 ROIs for the control, 7 RIOs before single tumor cell arrival, 15 ROIs upon arrival of single tumor cells, 17 ROIs for micrometastasis persistence, 14 ROIs for macrometastasis persistence, 6 ROIs after micrometastasis regression, calculated in 8 mice with metastasis and 3 control mice. Two-tailed Mann-Whitney-U test, *P<0.05, **P<0.01, ***P<0.01; error bars indicate SD).

4.12 Comparison of the fate of single metastasizing tumor cells in CX3CR1$^{GPF/wt}$ and CX3CR1$^{GPF/GFP}$ mice

A total of 107 and 137 single tumor cells could be successfully followed in CX3CR1$^{GFP/wt}$ and CX3CR1$^{GFP/GFP}$ mice, respectively. Most of the initially arrested tumor cells were dead or displaced before extravasation (57%, 71.5%). Only 42.9% of the initially arrested tumor cells in CX3CR1$^{GFP/wt}$ mice and only 28.4% of the initially arrested tumor cells in CX3CR1$^{GFP/GFP}$

mice showed successfully completed extravasation. This difference was statistically significant (p =0.0215< 0.05, Chi-square test) – the tumor cells in CX3CR1$^{GFP/wt}$ mice more often showed successful extravasation. However, only 8.4% (CX3CR1$^{GFP/wt}$) and 13.9% (CX3CR1$^{GFP/GFP}$) of the initially arrested tumor cells successfully formed micrometastases. Based on this finding in CX3CR1$^{GFP/wt}$ mice, micrometastasis formation was significantly less frequent than in CX3CR1$^{GFP/GFP}$ mice (p =0.0044<0.05, Chi-square test). Similarly, macrometastasis formation was observed less frequently in CX3CR1$^{GFP/wt}$ than in CX3CR1$^{GFP/GFP}$ mice (4.6% vs. 11.6%, respectively). However, this difference was not significant (p = 0.1652>0.05, Fisher's exact test).

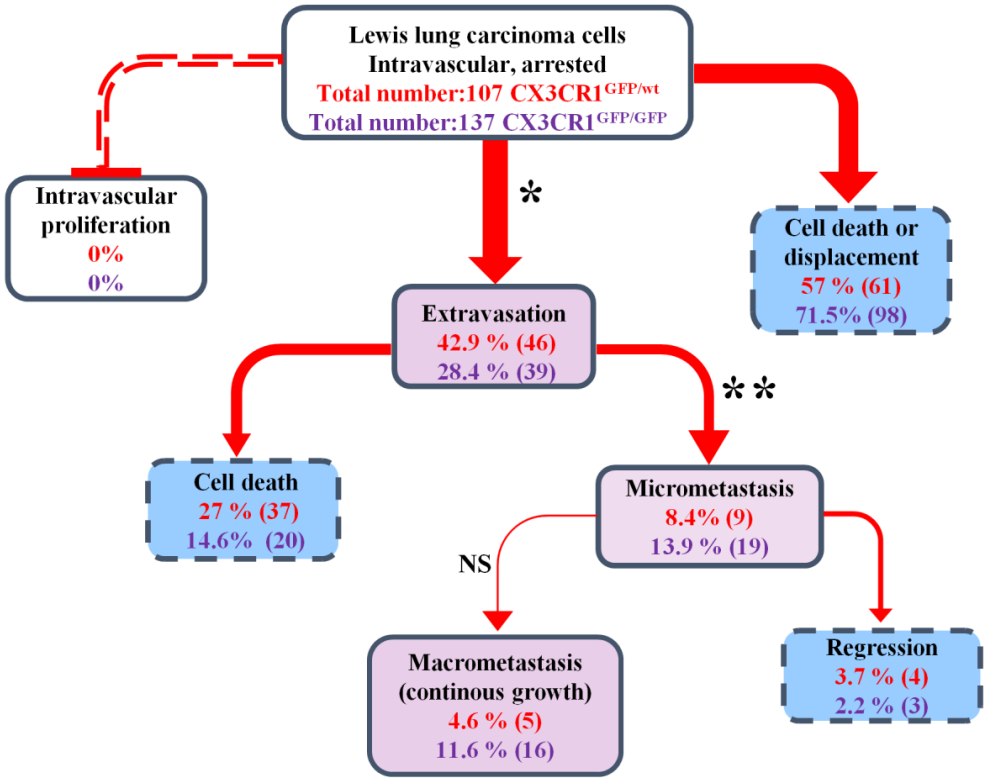

Figure 30: Comparison of the fate of metastasizing tumor cells in CX3CR1$^{GFP/wt}$ and CX3CR1$^{GFP/GFP}$ mice.

Quantification of the fate of single metastatic tumor cells in CX3CR1$^{GFP/wt}$ and CX3CR1$^{GFP/GFP}$ mice (n=8 mice per group) (extravasation versus cell death or displacement, cell death after extravasation versus micrometastasis, Chi-square test; macrometastasis versus regression of micrometastasis, Fisher`s exact test,*P<0.05, **P<0.01, ***P<0.01).

Taken together, our results showed that the metastastic efficiency in our syngeneic model was

very low. Furthermore, the metastatic efficiency was lower in CX3CR1$^{GFP/WT}$ than in CX3CR1$^{GFP/GFP}$ mice, although the process of extravasation seemed to be more efficient in CX3CR1$^{GFP/WT}$ mice.

5 Discussion

5.1 Mouse model

Prior to the development of mouse models, *in vitro* assays were the main approaches for the acquisition of cancer knowledge. Although the usage of *in vitro* assays provides valuable information and remains an important cancer research methodology, their limitations are obvious. For instance, such models fail to mimic the interactions between tumor cells and stromal cells of the microenvironment *in vivo*.

Thus, good experimental mouse models are urgently needed for preclinical research to reveal the mechanisms and to search for novel therapeutic regimens. Some xenograft mouse models have overcome these limitations and achieved certain levels of progress, but the usage of immunocompromised mice or subcutaneous implantation could not truly reflect the tumor characteristics both at genetic and morphologic levels. Therefore, the establishment of an ideal mouse model that could fully resemble human cancer cells has become the first and most important step for cancer research[119,120].

In 2009, a new animal model was established for brain metastasis research using a cranial window and two-photon laser scanning microscopy (TPLSM), which allows the tracking of single metastasizing tumor cells from different carcinomas *in vivo* over time for a period of weeks, which has been a major challenge in metastasis research over the past decades[17]. Compared with other models, the newly established model has several advantages.

First, the newly established model has a high cerebral metastasis formation efficiency. Generally, for the establishment of metastasis, mouse model tumor cells are injected in three positions: tail vein, intracardiac injection, and intracarotid injection. Tail vein injection of cancer cells usually leads to the formation of metastasis in the lung and seldomly the

outgrowth of tumor cells in the brain parenchyma. Thus, this technique is usually used for lung metastasis instead of brain metastasis models. Intracardiac injection of tumor cells frequently leads to the formation of metastases in other organs because only approximately 20% of tumor cells can travel to the brain through the blood flow, and tumor growth in the brain exhibits wide variability, making it difficult for therapeutic efficiency evaluations[121].

In our model, cancer cells were injected through the internal carotid artery. To avoid the spread of tumor cells to other regions, such as the face, eye, and ear, the external carotid artery was ligated. According to our experience, approximately 60% of the mice survived the procedure and had tumor cells under the chronic cranial window that could be followed using TPLSM. This result is similar to the data published by Yvonne Kienast *et al*[122]. Other groups have injected tumor cells through common carotid artery without ligation of the external carotid artery[37,38], although their data showed that this procedure also led to the formation of brain metastasis, and they did not describe the proportion of mice that formed metastasis in other parts of the head but not the brain.

Upon contacting the first author of the *Nature* paper[38], she replied that they attempted to ligate the external carotid artery, but due to technical difficulty, a high percentage of the consequently mice died. They also believed that ligation of external carotid artery should be better for establishment of the cerebral metastasis model.

Moreover, in some models, despite using intravital microscopic imaging to investigate the interactions between TAMs and metastasizing tumor cells, confocal but not multiphoton laser scanning microscopy were used, resulting in a depth of only less than 100 μm, which was not enough to investigate the interactions in the deeper cortex of the brain parenchyma[123]. In our model, we were able to obtain high-quality images as deep as 300 μm, which allowed us to acquire much more information than other imaging technologies.

Furthermore, in some cerebral metastasis mouse models, human tumor cell lines and nude mice were used[122]. However, this combination is not suitable to answer questions such as the role of TAMs in processes of cerebral metastasis formation, as nude mouse carry the *foxn 1* gene mutation, which causes a deteriorated or absent thymus, resulting in an inhibited immune system due to a greatly reduced number of T cells[124]. As T cells play an important role in antitumor outgrowth, T cell deficiency could not fully simulate patients in the clinic.

We established a syngeneic mouse model using Lewis lung carcinoma/LL/2/LLc1-Tdt cells and CX3CR1$^{GFP/wt}$ and CX3CR1$^{GFP/GFP}$ mice on the C57BL6 mouse strain background. Lewis lung carcinoma/LL/2/LLc1-Tdt is a cell line established from the lung of a C57BL mouse bearing a tumor resulting from implantation of primary Lewis lung carcinoma/LL/2/LLc1-Tdt, and matching of the murine tumor cell line and CX3CR1^{GFP} mouse strain to the utmost extent simulated cerebral metastasis in the clinic.

Another advantage of our models was that we could analyze the interactions between TAMs and tumor cells in 3D. Thus, both the density and volume of TAMs could be followed. Compared with other technologies, for example, immunohistochemistry, usually only 2D information can be obtained[12,14,125]. Moreover, for immunohistochemistry, large amounts of cutting and staining work are required, necessitating large amounts of time and cost to determine the exact distribution of metastases in the whole brain. However, in our model, TPLSM imaging of one region only takes 5-10 mins, which is more convenient.

5.2 Interactions between TAMs and metastasizing tumor cells in the early steps of cerebral metastasis formation

Numerous researchers have focused on the roles of TAMs in brain tumors. In malignant gliomas, TAMs constitute as many as 30-50%[126,127], while in human brain metastases, they can account for as much as 4 to 70%[128]. A large number of TAMs infiltrated in brain tumor masses are associated with a poor prognosis[129]. Scientists are attempting to reveal the role of TAMs in cerebral metastasis formation and expect to develop novel therapeutic strategies through a better understanding of the microenvironment of brain metastases. Former studies have shown the dual roles of TAMs in brain tumor progression. On the one hand, they act as tumor terminators and inhibit brain metastasis via phagocytosis and the release of cytotoxic factors[108,109]; on the other hand, ongoing inflammation can polarize TAMs into immunosuppressive stromal cells that promote tumor growth, colonization, angiogenesis, and brain invasion in response to certain stimuli[128,130].

The first question we need to answer concerns how TPLSM reveals the interactions between TAMs and tumor cells, using the 3D scan time lapse or only the 3D scan. Although the 3D scan time lapse is a good strategy for the timely recording of interactions between cells, the extravasation process may require hours or even longer. Thus, 3D scan time lapse is not as suitable to follow single metastasizing tumor cells in different steps of cerebral metastasis formation. Furthermore, long-term imaging of the same position may lead to phototoxicity and pathological changes. Additionally, long-term imaging is challenging for the mice.

Therefore, we chose the 3D scan instead of 3D scan time lapse for our experiments. At first, the time interval was 2-3 days; however, we found this time interval to be too long to gain sufficient information, as many interesting phenomena occur during the two imaging time points. However, conversely, we could not perform *in vivo* imaging on a daily basis, as high-frequency imaging will have severe side effects on the mice. Taking all of this

information into consideration, we acquired images every two days to follow regions of interest over time.

After the imaging methodology and time interval were determined, we started the experiments accordingly and obtained some interesting findings.

In the early steps of cerebral metastasis before extravasation, we found that tumor cells were elongated inside the vascular lumen, which is similar to a previous report[14]. However, we also found some differences from previous studies, which did not detect significant destruction of the vessel wall by immunohistochemistry[14]. In contrast, our data showed an increase in vascular diameter during the early steps of cerebral metastasis, and the pathological vascular morphology was recovered after regression of the metastatic tumor cells.

Moreover, we also acquired many interesting phenomena that have never been previously shown. For instance, previous literature has shown a heterogeneous recruitment and activation of TAMs in early steps of cerebral metastasis, either an absence of TAMs when metastatic tumor cells arrived in the brain parenchyma[14] or hyperactivation of TAMs[12]. The diverse responses of TAMs seem depends on differ mouse strains and tumor cell lines. Our data illustrated that when metastatic tumor cells attempted to escape from the BBB, resident immune cells in the brain started the activation process and the first wave of immune surveillance. In my opinion, there are two approaches via which TAMs can receive the signal from metastasizing tumor cells and become activated. As resident microglia have many motile processes extending from the small soma, timely scanning occurs to patrol the brain parenchyma[70]. Thus, microglia can be stimulated by direct interactions with metastasizing tumor cells. In such cases, the blood brain barrier will be damaged or at least a portion of the single tumor cells exposed outside of the vasculature.

Another possibility is that TAMs may be activated by certain factors, or cytokines. If tumor cells are attempting to escape the vessel to enter the brain cortex, the blood brain barrier will be destroyed, damage-associated molecular pattern molecules (DAMPs) will be released from the vessel wall[131], and the surrounding TAMs may receive these signals in a timely manner and be stimulated.

Although previous researchers have investigated the interactions between TAMs and metastatic tumor cells, most of them have failed to investigate their crosstalk in the early steps of cerebral metastasis[12,14,37]. Our data showed that TAMs had close contact with metastatic tumor cells in the early steps of cerebral metastasis. This close contact was beneficial for the elimination of metastasizing tumor cells, as we observed that TAMs exerted engulfment functions for single metastasizing tumor cells after extravasation. These results indicated that in the early stages of cerebral metastasis, innate responses mediated by microglia were beneficial and involved the activation of effective surveillance and tumoricidal effects, resulting in the elimination of single metastasizing cells.

5.3 Density and cell body volume of TAMs in different steps of cerebral metastasis formation

The changes in the number and activation degree of TAMs usually indicate different kinds of brain damage or injury[70]. For instance, in an Alzheimer's disease mouse model, increasing numbers of microglia promote the elimination of neurons[52], whereas depletion of microglia reduces motor-learning-dependent synapse formation. Also for other diseases: stroke, migraine, dementia, traumatic injury, epilepsy, and Parkinson's disease[132-134].

In brain tumor research, scientists have illustrated that TAMs are highly infiltrated in the

malignant tumor mass[135,136]. Some cerebral metastasis research has shown that TAMs gradually accumulate and show an enhanced degree of activation during tumor growth[123]; however, these data failed to follow the same region over time to compare the density and cell body volume changes from single metastasizing tumor cells to micro/macrometastases. Further, they could not indicate whether these parameter alterations occurred in regressing tumor lesions.

In our metastasis model, TAMs were followed in the same regions from the single tumor cell to micro/macrometastases. Our data showed that the densities and cell body volumes of TAMs gradually increased when single tumor cells arrived in the brain parenchyma, and the cell body volume simultaneously increased in both CX3CR1$^{GFP/wt}$ mice and CX3CR1$^{GFP/GFP}$ mice. Significant differences were observed in different steps of cerebral metastasis formation compared with control group mice in terms of the TAM density and cell body volume. In contrast, in regressing micrometastasis, both parameters were significantly decreased.

These data indicated that both the density and cell body volume of TAMs were influenced by metastasizing tumor cells, in different steps of cerebral metastasis the activation degrees of TAMs were different, and the larger the tumor size, the greater was the number of infiltrating TAMs, and vice versa.

5.4 Factors mediating the interactions between TAMs and metastasizing tumor cells

Cross-talk between metastatic tumor cells, TAMs, and other stromal cells facilitates establishment of the tumor microenvironment, and it also influences the tumor outcome[92]. Multiple factors that are expressed either by TAMs or tumor cells play critical roles in

tumorigenesis and invasion[137]. These factors include cytokines/chemokines like monocyte chemoattractant protein-1 (MCP-1), granulocyte/macrophage-colony stimulating factor (GM-CSF), CX3CL1, and CCL[138]; growth factors such as glia cell-derived neurotrophic factor (GDNF) and hepatocyte growth factor/scatter factor (HFG/SF)[139]; matrix metalloproteinases; and extracellular vesicles such as metabolites (e.g., adenosine triphosphate/ATP)[140,141], proteins, and nucleic acids (e.g., microRNAs: miR-223, miR-124, miR-137, miR-146b, and miR-451)[142-147].

CX3CR1, a G-protein-coupled receptor, and its ligand CX3CL1 (FKN) were first investigated in the transendothelial migration of leukocytes during the process of inflammation[148,149]. Their interactions may assist in the arrest of leukocytes in the small capillary under flow conditions.

Afterwards, many researchers revealed that CX3CR1 might play an important role in the process of tumor progression. For instance, CX3CR1 is overexpressed both at mRNA and protein levels in TAMs of malignant human astrocytomas and glioblastomas, regulating the recruitment and migration of immune cells in the tumor mass[49,58,150].

In the NF 1 (neurofibromatosis type 1)-associated optic glioma mouse model, CX3CR1 deficiency reduces TAM numbers and, thus, delays optic glioma formation[61]. Similarly, in the hepatic metastasis model, the microenvironment lacking CX3CR1 significantly suppresses tumor metastasis[62]. However, other publication have shown that in CX3CR1-deficient mice, neither the proliferation of GL261 glioma cells nor the infiltration of microglia and lymphocytes are altered compared with control mice[67].

The role of CX3CR1 has also been investigated in other type of cancers, such as human colon cancer, in which CX3CR1 upregulation is associated with a higher histologic malignancy grade and a poor prognosis. Deficiency of CX3CR1 inhibits the accumulation of TAMs in the

tumor mass, as well as increases TAM apoptosis. Moreover, angiogenesis is also blocked. Thus, CX3CR1 deficiency impairs tumor metastasis[62].

Some of our data are similar to previous studies, but others are not. For example, we also found an absence of CX3CR1 leading to decreased infiltration of TAMs in metastatic tumor lesions. However, in contrast to previous studies, we found that CX3CR1 deficiency assisted cerebral metastasis formation. This result indicates that the role of CX3CR1 in metastasis may differ in different organs.

Although the absence of CX3CR1 reduced TAM infiltration in metastatic tumor lesions, we still observed an increased number of TAMs in metastatic tumor lesions compared with regions without metastatic tumor growth, illustrating that CX3CR1 was not the only receptor mediating the recruitment of TAMs, as many receptors and signaling pathways are involved in communications between TAMs and tumor cells, such as CSF-1R[65,99]. Thus, CX3CR1 only partially affected their interactions.

5.5 Fate of metastatic tumor cells in the brain

Our data illustrate that the efficiency of cerebral metastasis formation is very low, with only approximately 5% and 12% of tumor cells successfully proliferating to generate a large macrometastasis in the $CX3CR1^{GFP/wt}$ and $CX3CR1^{GFP/GFP}$ group, respectively. Previous studies have also illustrated a low efficiency of metastasis. For instance, B16 melanoma lung metastasis experiments showed that 24 hours post-intravenous injection, only 1.5% of tumor cells survived, and less than 0.01% of circulating tumor cells in the blood streams formed lung metastases in the end[151]. Not only in lung metastasis, but brain metastasis formation efficiency is also very low. TPLSM was applied to successfully follow more than 100

metastatic lung carcinoma cells in the brain, of which only less than 3% successfully formed macrometastases[122].

Several explanations may be proposed to explain the low brain metastasis efficiency. First, the brain metastasis cascade requires several steps, each of which is challenging for metastatic tumor cells, and the tough blood brain barrier (BBB) makes the brain vessel wall more difficult to overcome compared with other organs[152]. Another possible explanation is immune surveillance, as numerous immune cells, such as NK cells, DCs, monocytes, T cells, and B cells, are circulating and surveying in the blood, resulting in the elimination of many cells. Moreover, microglia and macrophages in the brain also exhibit immune response toward the metastatic tumor cells. Thus, both physical barriers and immune activation together lead to the inefficiency of brain metastasis formation.

After comparing the fate of tumor cells in the two mouse strains, $CX3CR1^{GFP/wt}$ and $CX3CR1^{GFP/GFP}$, we found that the absence of CX3CR1 significantly increased cerebral metastasis formation. This result seems to differ from the former literature. In liver cancer lacking CX3CR1, tumor metastasis is inhibited[62], and in a glioma model, reduced CX3CR1 expression delays tumor outgrowth[61]. We think the role of CX3CR1 may be different in different types of cancers, and in brain metastasis, it may facilitate TAMs recruitment and elimination of metastatic tumor cells, while in glioma and liver cancer, overexpression of CX3CR1 may help to establish a suppressive microenvironment that facilitates tumor proliferation and metastasis.

5.6 Limitations

As both microglia/macrophages express CX3CR1 receptor, the GFP signal could be investigated in both immune cells. Thus, in this thesis, we did not distinguish microglia/macrophages. However, TAMs have different origins and belong to different cell types. Thus, it is still necessary to investigate whether microglia/macrophages have different roles in cerebral metastasis formation.

One strategy to distinguish microglia/macrophages could depend on turnover rate differences. In contrast to peripheral monocytes and inflammatory macrophages that exhibit rapid turnover[153], microglia are self-renewable with a low turnover rate[154,155].

Theoretically, generation of the CX3CR1$^{CreER/+}$-eYFP: R26$^{DsRed/+}$ mouse strain could successfully distinguish microglia/macrophages using two-photon *in vivo* microscopy. According to previous publications in CX3CR1$^{CreER/+}$: R26$^{iDTR/+}$ mice, tamoxifen administration 30 days prior to the administration of DT successfully depleted approximately 99% of microglia; however, monocytes in the blood or spleen did not show significant differences compared with the control mice. This finding indicated that microglia were specifically depleted in the CNS[156].

Another selective microglial ablation strategy is the use of the CSF-1R inhibitor PLX3397. CSF-1R-dependent signaling is very important for the survival and activation of microglia. Extensive treatment with a brain-penetrant CSF-1R kinase inhibitor resulted in the elimination of ~99% of microglia throughout the brain. The depletion of microglia has no apparent gross deleterious effects in healthy mice: no signs of BBB damage, leukocyte recruitment, weight loss, or brain inflammation are[157] observed after CSF-1R inhibition. Thus, the depletion of microglia using a small-molecule inhibitor introduces minimal disturbance to the brain and no alterations of peripheral leukocytes, enabling our group to selectively study

the roles of microglia[158,159].

Another limitation of this thesis is the origin of the increasing TAMs. As we observed, a large number of TAMs infiltrated in the cerebral metastases, and thus, it was difficult to determine whether these cells were from the proliferation of TAMs or the peripheral blood.

Furthermore, we did not distinguish the subtypes of TAMs in different steps of cerebral metastasis formation. The M1/M2 phenotypes of TAMs have different tumor cell roles, and their numbers and proportions will influence the fate of metastatic tumor cells. This part of our work will be continued using immunohistochemistry.

6 Conclusion

Although numerous studies have already focused on the role of TAMs in brain tumors, the detailed interactions between TAMs and metastasizing tumor cells in different steps of cerebral metastasis formation are still unclear.

Here we established a syngeneic mouse model to follow the interactions between TAMs and metastatic tumor cells over time.

Further, in CX3CR1$^{GFP/wt}$ mice, we demonstrated that TAMs have close contacts with tumor cells in the early steps of cerebral metastasis formation. Close contact between TAMs and metastasizing tumor cells in the early steps of cerebral metastasis is beneficial, as TAMs have engulfment functions for single extravasated tumor cells.

In CX3CR1$^{GFP/GFP}$ mice, we found that TAMs remained in a relatively stable state for intravascularly arrested tumor cells. We also observed a close contact between TAMs in the early steps of cerebral metastasis formation.

After calculation of both the density and cell body volume of TAMs in both groups of mice, we found that both parameters were influenced by metastatic tumor cells. Both the density and cell body volume of TAMs gradually increased along with tumor proliferation. However, when metastasis regressed, both parameters decreased. A statistically significant difference in different steps of cerebral metastasis was observed compared with control group mice.

After comparison of the density and cell body volume of TAMs in CX3CR1$^{GFP/wt}$ and CX3CR1$^{GFP/GFP}$ mice, we found effect of CX3CR1 on the infiltration of TAMs toward metastatic tumor cells, but not activation. As suggested by the quantitative data, fewer TAMs

were infiltrated in metastatic tumor lesions in CX3CR1-deficient mice, while the cell body volume of TAMs was similar without a significant difference. This finding indicated that CX3CR1 played an important role in the infiltration of TAMs toward metastatic tumor cells, but not their activation.

Moreover, we compared the fate of metastatic tumor cells in $CX3CR1^{GFP/wt}$ and $CX3CR1^{GFP/GFP}$ mice. After quantification, we observed the formation of significantly more tumor cells in micrometastases with reduced elimination in $CX3CR1^{GFP/GFP}$ mice after extravasation. In the $CX3CR1^{GFP/GFP}$ group, successful cerebral metastasis efficiency was much higher than in normal $CX3CR1^{GFP/wt}$ mice. We further found that in both normal $CX3CR1^{GFP/wt}$ and deficient $CX3CR1^{GFP/GFP}$ mice, the efficiency of successful cerebral metastasis was very low at approximately 5% and 12%, respectively.

Overall, we established a syngeneic cerebral metastasis model combining the chronic cranial window and two-photon microscopy. Using this model, we successfully investigated the interactions between TAMs and metastatic tumor cells in different steps of cerebral metastasis formation. We found that TAMs had close contact with metastatic tumor cells in the early steps of cerebral metastasis, and this close contact was beneficial for the eradication of metastatic tumor cells as the TAMs could exert engulfment functions toward metastatic tumor cells after extravasation. Moreover, in the CX3CR1-deficient group, we found that fewer TAMs were infiltrated in metastatic tumor lesions, potentially fewer tumor cells were eliminated during the first wave of immune surveillance and then more tumor cells formed micrometastases. Ultimately, the successful cerebral metastasis efficiency was higher in $CX3CR1^{GFP/GFP}$ than in $CX3CR1^{GFP/wt}$ mice.

7 Outlook

In addition to focusing on the role of CX3CR1 in cerebral metastasis, another receptor we plan to investigate is CSF-1R. CSF-1R is very important for the proliferation, differentiation, and survival of TAMs[160]. Publications have shown that extensive treatment of mice using the CSF-1R inhibitor PLX3397 specifically depletes brain microglia, with a depletion efficiency reaching as high as 99%. Elimination of microglia in the adult CNS has no side effects such as body weight loss or deficits in behavior, cognition, or the blood brain barrier. Moreover, CSF-1R inhibition does not alter the spleen and blood immune cells; thus, the small molecule inhibitor PLX3397 can be used for the depletion of microglia and investigation of changes in cerebral metastasis after microglial elimination[158,159].

We also investigated the depletion efficiency using our *in vivo* mouse model, and preliminary results showed a high depletion efficiency of PLX3397. After 1 month of treatment, 85-87% of the microglia/macrophages were depleted.

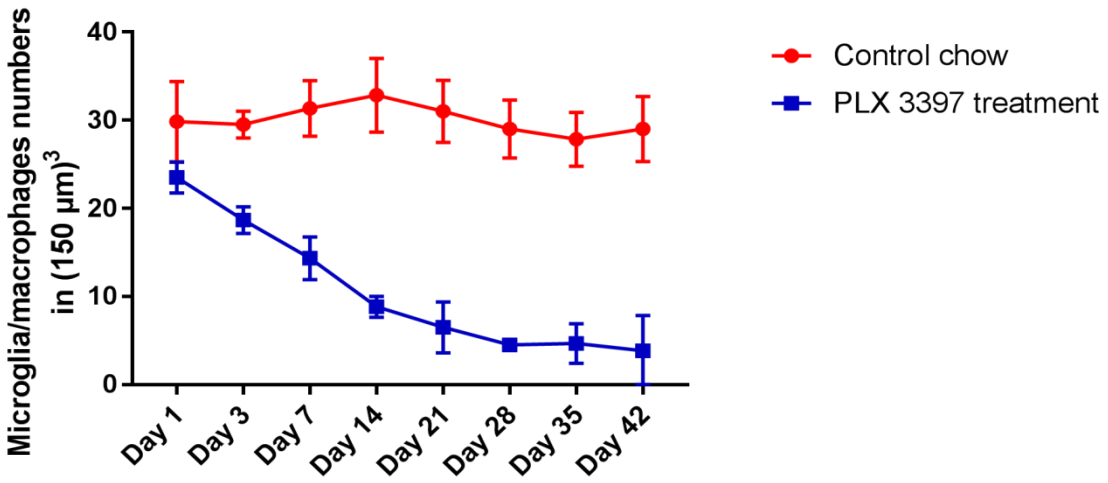

Figure 31: High depletion efficiency of brain microglia/macrophages after CSF-1R inhibition using PLX3397.

Control chow treatment did not alter the numbers of microglia/macrophages, while CSF-1R treatment led to a high depletion efficiency. One mouse per group and 6 regions were followed over time.

In the next steps, we plan to confirm the side effects of PLX3397 treatment. Immune cells from the blood, bone marrow, and spleen will be harvested and analyzed using FACS to confirm whether CSF-1R inhibition using PLX3397 has no influence on peripheral immune cells.

8 Acknowledgments

How time flies. I cannot imagine the four years of colorful, happy, and stressful PhD life coming to an end. The scene on the first day I arrived in Munich is still vivid in my mind. I am honored to be a member of LMU; the experience I had here will benefit my whole life.

First, I am sincerely grateful to my supervisor, Louisa, who gave me this opportunity to study in this world-renowned university. She guided me step by step toward the right path of scientific research. Looking back, my basic knowledge was relatively weak, and I had developed some unscientific experimental ideas and habits, which seriously hindered my progress and development of my project. She patiently corrected my mistakes, tolerated my shortcomings and waited for my progress. When confronted with difficulties, she consistently helped me to search for the possible reasons, and after discussion, correct approaches could be found. Her working style of a scientific, rigorous research attitude and the pursuit of excellence is my lifelong goal.

Second, I would like to extend my great thanks to my TAC members, Prof. Steffen Massberg, Prof. Andreas Straube, and Prof. Christian Schulz. With their help, I obtained the chance to study here and start my project. Through their support, I became a PhD student of IRTG 914. They offered an excellent experimental platform and provided many good suggestions and guidance for the progress of the project. Their encouragement helped give me confidence and energy.

Third, I would like to show my great thanks to Sigrid Langer. As a foreigner, Visa application and flat renting constitute the basis of living in Munich. Because of language barriers, this issue raised many difficulties. I am very thankful to Sigrid, she helped me contact the related departments and prepare the necessary documents to guarantee that I could study and work here. Not only for daily life but also in experiments, Sigrid offered many good ideas and

suggestions.

Moreover, I would like to show my great thanks to Matthias Mulazzani and most of the experimental technicians, for assistance with, e.g., window preparation, animal care, and two-photon microscopy. He also provided many sources of literature, documents, and good ideas, which assisted the progress of this project. At first, speaking and listening to English was very difficult for me. During daily communication with Matthias, my English improved, laying the foundation for the start of the experiments.

I would also like to show my sincere thanks to Iven, especially for the quantification and statistical analysis. He helped me determine the correct method to analyze different data and recalculated data to avoid bias. He also offered many good suggestions during my thesis writing.

Furthermore, I would like to show my great thanks to Tao Xu. He came to the lab about three months before I left. These three months were the busiest period for me. I had to finish my project, prepare figures, and plan a 3rd TAC meeting, among others. After Tao arrived in Munich, he started to kindly help me with all kinds of works, which save me lots of time to concentrate on the main part of my work. He also encouraged me when I was confronted with some difficulties. His positive attitude and hard-working passion impressed me. I believe he will do a good job in our lab and look forward to further cooperation with him after he returns to China.

Moreover, I would like to extend my great thanks to Anna, who had only several months to perform her internship lab work. During this short period of time, she became skilled at immunohistology and started to perform staining of the TAMs to confirm the observations we acquired from TPLSM. Her efforts efficiently improved the progress of our project. I appreciate her participation.

And also, I would like to show my great thanks to Teresa from the company of American Journal Experts (AJE). He/she helped to correct grammar and format errors this makes the thesis meet the submission requirements.

Furthermore, I would like to show my great thanks to my friends, Xiaolan, Wenwen, Shuxia, Zhe Zhang, Yuan Shi, Jiehua, Zheming, Liu huan, Wenyan, Jiahui, Duorong, Wangjing, and Ningning. We have shared our study experiences and helped each other, making life colorful and interesting. With their friendship, I am no longer alone.

Additionally, I would like to show my great thanks to the CSC (China Scholarship Council). I am proud to be a member of the CSC-LMU program. With their financial support, I can focus on my studies here without worrying about daily expenses.

Last but not least, I am very grateful to my parents and large family. Their encouragement, support, and understanding afforded me the courage to overcome difficulties and persevere.

9 References

1. Steeg, P.S. Tumor metastasis: mechanistic insights and clinical challenges. *Nature medicine* **12**, 895-904 (2006).
2. Massagué, J. & Obenauf, A.C. Metastatic colonization by circulating tumour cells. *Nature* **529**, 298-306 (2016).
3. Chen, Q.*, et al.* Carcinoma–astrocyte gap junctions promote brain metastasis by cGAMP transfer. *Nature* **533**, 493-498 (2016).
4. Zhang, L.*, et al.* Microenvironment-induced PTEN loss by exosomal microRNA primes brain metastasis outgrowth. *Nature* **527**, 100-104 (2015).
5. Headley, M.B.*, et al.* Visualization of immediate immune responses to pioneer metastatic cells in the lung. *Nature* **531**, 513-517 (2016).
6. Osswald, M.*, et al.* Brain tumour cells interconnect to a functional and resistant network. *Nature* (2015).
7. Pyonteck, S.M.*, et al.* CSF-1R inhibition alters macrophage polarization and blocks glioma progression. *Nature medicine* **19**, 1264-1272 (2013).
8. Prinz, M. & Priller, J. Microglia and brain macrophages in the molecular age: from origin to neuropsychiatric disease. *Nature Reviews Neuroscience* **15**, 300-312 (2014).
9. Hickey, W.F. & Kimura, H. Perivascular microglial cells of the CNS are bone marrow-derived and present antigen in vivo. *Science* **239**, 290-292 (1988).
10. Hickey, W.F., Vass, K. & Lassmann, H. Bone marrow-derived elements in the central nervous system: an immunohistochemical and ultrastructural survey of rat chimeras. *Journal of Neuropathology & Experimental Neurology* **51**, 246-256 (1992).
11. Zhang, M. & Olsson, Y. Reactions of astrocytes and microglial cells around hematogenous metastases of the human brain. Expression of endothelin-like immunoreactivity in reactive astrocytes and activation of microglial cells. *Journal of the neurological sciences* **134**, 26-32 (1995).
12. He, B.P.*, et al.* Differential reactions of microglia to brain metastasis of lung cancer. *Molecular medicine (Cambridge, Mass.)* **12**, 161-170 (2006).
13. Fitzgerald, D.P.*, et al.* Reactive glia are recruited by highly proliferative brain metastases of breast cancer and promote tumor cell colonization. *Clinical & experimental metastasis* **25**, 799-810 (2008).
14. Lorger, M. & Felding-Habermann, B. Capturing changes in the brain microenvironment during initial steps of breast cancer brain metastasis. *The American journal of pathology* **176**, 2958-2971 (2010).
15. Jung, S.*, et al.* Analysis of fractalkine receptor CX3CR1 function by targeted

deletion and green fluorescent protein reporter gene insertion. *Molecular and cellular biology* **20**, 4106-4114 (2000).

16. Held-Feindt, J.*, et al.* CX3CR1 promotes recruitment of human glioma-infiltrating microglia/macrophages (GIMs). *Experimental cell research* **316**, 1553-1566 (2010).
17. Kienast, Y.*, et al.* Real-time imaging reveals the single steps of brain metastasis formation. *Nature medicine* **16**, 116 (2010).
18. Palmieri, D., Chambers, A.F., Felding-Habermann, B., Huang, S. & Steeg, P.S. The biology of metastasis to a sanctuary site. *Clinical cancer research : an official journal of the American Association for Cancer Research* **13**, 1656-1662 (2007).
19. Posner, J.B. & Chernik, N.L. Intracranial metastases from systemic cancer. *Adv Neurol* **19**, 579-592 (1978).
20. Takakura, K. *Metastatic tumors of the central nervous system*, (Igaku-Shoin Medical Publishers, 1982).
21. Stewart, B. & Wild, C.P. World cancer report 2014. *Health* (2017).
22. Palmieri, D., Chambers, A.F., Felding-Habermann, B., Huang, S. & Steeg, P.S. The biology of metastasis to a sanctuary site. *Clinical Cancer Research* **13**, 1656-1662 (2007).
23. Vachan, C. Magnetic resonance images of brain metastases (2017).
24. Delattre, J.Y., Krol, G., Thaler, H.T. & Posner, J.B. Distribution of brain metastases. *Arch Neurol* **45**, 741-744 (1988).
25. Chang, E.L.*, et al.* A pilot study of neurocognitive function in patients with one to three new brain metastases initially treated with stereotactic radiosurgery alone. *Neurosurgery* **60**, 277-283; discussion 283-274 (2007).
26. Mehta, M.P.*, et al.* Survival and neurologic outcomes in a randomized trial of motexafin gadolinium and whole-brain radiation therapy in brain metastases. *Journal of clinical oncology : official journal of the American Society of Clinical Oncology* **21**, 2529-2536 (2003).
27. Eichler, A.F.*, et al.* The biology of brain metastases-translation to new therapies. *Nature reviews. Clinical oncology* **8**, 344-356 (2011).
28. Lin, X. & DeAngelis, L.M. Treatment of Brain Metastases. *Journal of clinical oncology : official journal of the American Society of Clinical Oncology* **33**, 3475-3484 (2015).
29. Headley, M.B.*, et al.* Visualization of immediate immune responses to pioneer metastatic cells in the lung. *Nature* **531**, 513 (2016).
30. Strilic, B.*, et al.* Tumour-cell-induced endothelial cell necroptosis via death receptor 6 promotes metastasis. *Nature* **536**, 215 (2016).

31. Hess, K.R., *et al.* Metastatic patterns in adenocarcinoma. *Cancer* **106**, 1624-1633 (2006).

32. Patel, J.K., Didolkar, M.S., Pickren, J.W. & Moore, R.H. Metastatic pattern of malignant melanoma. A study of 216 autopsy cases. *Am J Surg* **135**, 807-810 (1978).

33. Paget, S. The distribution of secondary growths in cancer of the breast. 1889. *Cancer Metastasis Rev* **8**, 98-101 (1989).

34. Ewing, J. Neoplastic diseases. A treatise on tumors. *The American Journal of the Medical Sciences* **176**, 278 (1928).

35. Duda, D.G., *et al.* Malignant cells facilitate lung metastasis by bringing their own soil. *Proceedings of the National Academy of Sciences* **107**, 21677-21682 (2010).

36. Pukrop, T., *et al.* Microglia promote colonization of brain tissue by breast cancer cells in a Wnt-dependent way. *Glia* **58**, 1477-1489 (2010).

37. Qiao, S., Qian, Y., Xu, G., Luo, Q. & Zhang, Z. Long-term characterization of activated microglia/macrophages facilitating the development of experimental brain metastasis through intravital microscopic imaging. *Journal of neuroinflammation* **16**, 4 (2019).

38. Zhang, L., *et al.* Microenvironment-induced PTEN loss by exosomal microRNA primes brain metastasis outgrowth. *Nature* **527**, 100-104 (2015).

39. Junttila, M.R. & de Sauvage, F.J. Influence of tumour micro-environment heterogeneity on therapeutic response. *Nature* **501**, 346 (2013).

40. Wolf, Y., Yona, S., Kim, K.W. & Jung, S. Microglia, seen from the CX3CR1 angle. *Front Cell Neurosci* **7**, 26 (2013).

41. Bazan, J.F., *et al.* A new class of membrane-bound chemokine with a CX3C motif. *Nature* **385**, 640-644 (1997).

42. Pan, Y., *et al.* Neurotactin, a membrane-anchored chemokine upregulated in brain inflammation. *Nature* **387**, 611-617 (1997).

43. Kanazawa, N., *et al.* Fractalkine and macrophage-derived chemokine: T cell-attracting chemokines expressed in T cell area dendritic cells. *European journal of immunology* **29**, 1925-1932 (1999).

44. Papadopoulos, E.J., *et al.* Fractalkine, a CX3C chemokine, is expressed by dendritic cells and is up-regulated upon dendritic cell maturation. *European journal of immunology* **29**, 2551-2559 (1999).

45. Lindia, J.A., McGowan, E., Jochnowitz, N. & Abbadie, C. Induction of CX3CL1 expression in astrocytes and CX3CR1 in microglia in the spinal cord of a rat model of neuropathic pain. *The journal of pain : official journal of the American Pain Society* **6**, 434-438 (2005).

46. Harrison, J.K., *et al.* Role for neuronally derived fractalkine in mediating interactions between neurons and CX3CR1-expressing microglia. *Proceedings of the National Academy of Sciences of the United States of America* **95**, 10896-10901 (1998).

47. Nishiyori, A., *et al.* Localization of fractalkine and CX3CR1 mRNAs in rat brain: does fractalkine play a role in signaling from neuron to microglia? *FEBS letters* **429**, 167-172 (1998).

48. Zhang, M., Xu, G., Liu, W., Ni, Y. & Zhou, W. Role of fractalkine/CX3CR1 interaction in light-induced photoreceptor degeneration through regulating retinal microglial activation and migration. *PloS one* **7**, e35446 (2012).

49. Ferretti, E., Pistoia, V. & Corcione, A. Role of fractalkine/CX3CL1 and its receptor in the pathogenesis of inflammatory and malignant diseases with emphasis on B cell malignancies. *Mediators of inflammation* **2014**, 480941 (2014).

50. Medina-Contreras, O., *et al.* CX3CR1 regulates intestinal macrophage homeostasis, bacterial translocation, and colitogenic Th17 responses in mice. *The Journal of clinical investigation* **121**, 4787-4795 (2011).

51. Fong, A.M., *et al.* Fractalkine and CX3CR1 mediate a novel mechanism of leukocyte capture, firm adhesion, and activation under physiologic flow. *The Journal of experimental medicine* **188**, 1413-1419 (1998).

52. Fuhrmann, M., *et al.* Microglial Cx3cr1 knockout prevents neuron loss in a mouse model of Alzheimer's disease. *Nat Neurosci* **13**, 411-413 (2010).

53. Ambrosini, E. & Aloisi, F. Chemokines and glial cells: a complex network in the central nervous system. *Neurochemical research* **29**, 1017-1038 (2004).

54. Savarin-Vuaillat, C. & Ransohoff, R.M. Chemokines and chemokine receptors in neurological disease: raise, retain, or reduce? *Neurotherapeutics : the journal of the American Society for Experimental NeuroTherapeutics* **4**, 590-601 (2007).

55. Cartier, L., Hartley, O., Dubois-Dauphin, M. & Krause, K.H. Chemokine receptors in the central nervous system: role in brain inflammation and neurodegenerative diseases. *Brain research. Brain research reviews* **48**, 16-42 (2005).

56. Lauro, C., *et al.* Activity of adenosine receptors type 1 Is required for CX3CL1-mediated neuroprotection and neuromodulation in hippocampal neurons. *Journal of immunology (Baltimore, Md. : 1950)* **180**, 7590-7596 (2008).

57. Locatelli, M., *et al.* Human glioma tumors express high levels of the chemokine receptor CX3CR1. *European cytokine network* **21**, 27-33 (2010).

58. Held-Feindt, J., *et al.* CX3CR1 promotes recruitment of human glioma-infiltrating microglia/macrophages (GIMs). *Experimental cell research* **316**, 1553-1566 (2010).

59. Park, M.H., Lee, J.S. & Yoon, J.H. High expression of CX3CL1 by tumor cells

correlates with a good prognosis and increased tumor-infiltrating CD8+ T cells, natural killer cells, and dendritic cells in breast carcinoma. *Journal of surgical oncology* **106**, 386-392 (2012).

60. Sciume, G.*, et al.* CX3CR1/CX3CL1 axis negatively controls glioma cell invasion and is modulated by transforming growth factor-beta1. *Neuro-oncology* **12**, 701-710 (2010).

61. Pong, W.W., Higer, S.B., Gianino, S.M., Emnett, R.J. & Gutmann, D.H. Reduced microglial CX3CR1 expression delays neurofibromatosis-1 glioma formation. *Annals of neurology* **73**, 303-308 (2013).

62. Zheng, J.*, et al.* Chemokine receptor CX3CR1 contributes to macrophage survival in tumor metastasis. *Molecular cancer* **12**, 141 (2013).

63. Andre, F.*, et al.* Expression of chemokine receptors predicts the site of metastatic relapse in patients with axillary node positive primary breast cancer. *Annals of oncology : official journal of the European Society for Medical Oncology* **17**, 945-951 (2006).

64. Su, Z.*, et al.* The synergistic interaction between the calcineurin B subunit and IFN-γ enhances macrophage antitumor activity. *Cell Death &Amp; Disease* **6**, e1740 (2015).

65. Pyonteck, S.M.*, et al.* CSF-1R inhibition alters macrophage polarization and blocks glioma progression. *Nature medicine* **19**, 1264-1272 (2013).

66. Yu, R.*, et al.* Inhibition of the CSF-1 receptor sensitizes ovarian cancer cells to cisplatin. *Cell biochemistry and function* **36**, 80-87 (2018).

67. Liu, C., Luo, D., Streit, W.J. & Harrison, J.K. CX3CL1 and CX3CR1 in the GL261 murine model of glioma: CX3CR1 deficiency does not impact tumor growth or infiltration of microglia and lymphocytes. *Journal of neuroimmunology* **198**, 98-105 (2008).

68. Jung, S.*, et al.* Analysis of fractalkine receptor CX(3)CR1 function by targeted deletion and green fluorescent protein reporter gene insertion. *Mol Cell Biol* **20**, 4106-4114 (2000).

69. Penfield, W. *Cytology & cellular pathology of the nervous system*, (P.B. Hoeber, inc., New York, 1932).

70. Nimmerjahn, A., Kirchhoff, F. & Helmchen, F. Resting microglial cells are highly dynamic surveillants of brain parenchyma in vivo. *Science* **308**, 1314-1318 (2005).

71. Prinz, M. & Priller, J. Microglia and brain macrophages in the molecular age: from origin to neuropsychiatric disease. *Nature reviews. Neuroscience* **15**, 300-312 (2014).

72. Yona, S.*, et al.* Fate mapping reveals origins and dynamics of monocytes and tissue

macrophages under homeostasis. *Immunity* **38**, 79-91 (2013).

73. Ginhoux, F.*, et al.* Fate mapping analysis reveals that adult microglia derive from primitive macrophages. *Science* **330**, 841-845 (2010).

74. Kierdorf, K.*, et al.* Microglia emerge from erythromyeloid precursors via Pu.1- and Irf8-dependent pathways. *Nature neuroscience* **16**, 273-280 (2013).

75. Schulz, C.*, et al.* A lineage of myeloid cells independent of Myb and hematopoietic stem cells. *Science* **336**, 86-90 (2012).

76. Alliot, F., Godin, I. & Pessac, B. Microglia derive from progenitors, originating from the yolk sac, and which proliferate in the brain. *Brain research. Developmental brain research* **117**, 145-152 (1999).

77. Davalos, D.*, et al.* ATP mediates rapid microglial response to local brain injury in vivo. *Nat Neurosci* **8**, 752-758 (2005).

78. Sieger, D., Moritz, C., Ziegenhals, T., Prykhozhij, S. & Peri, F. Long-range Ca2+ waves transmit brain-damage signals to microglia. *Developmental cell* **22**, 1138-1148 (2012).

79. Hanisch, U.K. & Kettenmann, H. Microglia: active sensor and versatile effector cells in the normal and pathologic brain. *Nat Neurosci* **10**, 1387-1394 (2007).

80. S.Vandenbery. Introduction to the pathobiology of the Nervous system. (2010).

81. Hickey, W.F. & Kimura, H. Perivascular microglial cells of the CNS are bone marrow-derived and present antigen in vivo. *Science (New York, N.Y.)* **239**, 290-292 (1988).

82. Hickey, W.F., Vass, K. & Lassmann, H. Bone marrow-derived elements in the central nervous system: an immunohistochemical and ultrastructural survey of rat chimeras. *Journal of neuropathology and experimental neurology* **51**, 246-256 (1992).

83. Bertrand, J.Y.*, et al.* Three pathways to mature macrophages in the early mouse yolk sac. *Blood* **106**, 3004-3011 (2005).

84. Cumano, A. & Godin, I. Ontogeny of the hematopoietic system. *Annu. Rev. Immunol.* **25**, 745-785 (2007).

85. Graeber, M.B., Scheithauer, B.W. & Kreutzberg, G.W. Microglia in brain tumors. *Glia* **40**, 252-259 (2002).

86. Watters, J.J., Schartner, J.M. & Badie, B. Microglia function in brain tumors. *Journal of neuroscience research* **81**, 447-455 (2005).

87. Izraely, S.*, et al.* The metastatic microenvironment: Melanoma-microglia cross-talk promotes the malignant phenotype of melanoma cells. *International journal of cancer* **144**, 802-817 (2019).

88. De Palma, M.*, et al.* Tie2 identifies a hematopoietic lineage of proangiogenic

monocytes required for tumor vessel formation and a mesenchymal population of pericyte progenitors. *Cancer Cell* **8**, 211-226 (2005).

89. Lu-Emerson, C.*, et al.* Increase in tumor-associated macrophages after antiangiogenic therapy is associated with poor survival among patients with recurrent glioblastoma. *Neuro-oncology* **15**, 1079-1087 (2013).

90. Piao, Y.*, et al.* Glioblastoma resistance to anti-VEGF therapy is associated with myeloid cell infiltration, stem cell accumulation, and a mesenchymal phenotype. *Neuro-oncology* **14**, 1379-1392 (2012).

91. Benbenishty, A.*, et al.* Prophylactic TLR9 stimulation reduces brain metastasis through microglia activation. *PLoS biology* **17**, e2006859 (2019).

92. Movahedi, K.*, et al.* Different tumor microenvironments contain functionally distinct subsets of macrophages derived from Ly6C(high) monocytes. *Cancer research* **70**, 5728-5739 (2010).

93. Mantovani, A., Sozzani, S., Locati, M., Allavena, P. & Sica, A. Macrophage polarization: tumor-associated macrophages as a paradigm for polarized M2 mononuclear phagocytes. *Trends in immunology* **23**, 549-555 (2002).

94. Su, Z.*, et al.* The synergistic interaction between the calcineurin B subunit and IFN-gamma enhances macrophage antitumor activity. *Cell Death Dis* **6**, e1740 (2015).

95. Wynn, T.A., Chawla, A. & Pollard, J.W. Macrophage biology in development, homeostasis and disease. *Nature* **496**, 445-455 (2013).

96. Biswas, S.K. & Mantovani, A. Macrophage plasticity and interaction with lymphocyte subsets: cancer as a paradigm. *Nature immunology* **11**, 889-896 (2010).

97. Gordon, S. & Martinez, F.O. Alternative activation of macrophages: mechanism and functions. *Immunity* **32**, 593-604 (2010).

98. Hoves, S.*, et al.* A critical role for granzymes in antigen cross-presentation through regulating phagocytosis of killed tumor cells. *Journal of immunology (Baltimore, Md. : 1950)* **187**, 1166-1175 (2011).

99. Ries, C.H.*, et al.* Targeting tumor-associated macrophages with anti-CSF-1R antibody reveals a strategy for cancer therapy. *Cancer cell* **25**, 846-859 (2014).

100. So, P.T. Two-photon Fluorescence Light Microscopy. *eLS*.

101. Göppert-Mayer, M. Über elementarakte mit zwei quantensprüngen. *Annalen der Physik* **401**, 273-294 (1931).

102. Denk, W., Strickler, J.H. & Webb, W.W. Two-photon laser scanning fluorescence microscopy. *Science (New York, N.Y.)* **248**, 73-76 (1990).

103. So, P.T. Two-photon Fluorescence Light Microscopy. (2002).

104. Helmchen, F. & Denk, W. Deep tissue two-photon microscopy. *Nature methods* **2**, 932 (2005).

105. Dibaj, P.*, et al.* In vivo imaging reveals rapid morphological reactions of astrocytes towards focal lesions in an ALS mouse model. *Neuroscience letters* **497**, 148-151 (2011).

106. Kasischke, K.A., Vishwasrao, H.D., Fisher, P.J., Zipfel, W.R. & Webb, W.W. Neural activity triggers neuronal oxidative metabolism followed by astrocytic glycolysis. *Science (New York, N.Y.)* **305**, 99-103 (2004).

107. Lichtman, J.W. & Fraser, S.E. The neuronal naturalist: watching neurons in their native habitat. *Nat Neurosci* **4 Suppl**, 1215-1220 (2001).

108. Svoboda, K., Tank, D.W. & Denk, W. Direct measurement of coupling between dendritic spines and shafts. *Science (New York, N.Y.)* **272**, 716-719 (1996).

109. Lütcke, H. & Helmchen, F. Two-photon imaging and analysis of neural network dynamics. *Reports on Progress in Physics* **74**, 086602 (2011).

110. Denk, W.*, et al.* Anatomical and functional imaging of neurons using 2-photon laser scanning microscopy. *Journal of neuroscience methods* **54**, 151-162 (1994).

111. Nolte, C.*, et al.* GFAP promoter-controlled EGFP-expressing transgenic mice: a tool to visualize astrocytes and astrogliosis in living brain tissue. *Glia* **33**, 72-86 (2001).

112. Hirrlinger, P.G.*, et al.* Expression of reef coral fluorescent proteins in the central nervous system of transgenic mice. *Molecular and cellular neurosciences* **30**, 291-303 (2005).

113. Weigert, R., Porat-Shliom, N. & Amornphimoltham, P. Imaging cell biology in live animals: ready for prime time. *The Journal of cell biology* **201**, 969-979 (2013).

114. Winkler, F.*, et al.* Kinetics of vascular normalization by VEGFR2 blockade governs brain tumor response to radiation: role of oxygenation, angiopoietin-1, and matrix metalloproteinases. *Cancer Cell* **6**, 553-563 (2004).

115. von Baumgarten, L.*, et al.* Bevacizumab has differential and dose-dependent effects on glioma blood vessels and tumor cells. *Clinical cancer research : an official journal of the American Association for Cancer Research* **17**, 6192-6205 (2011).

116. Campbell, R.E.*, et al.* A monomeric red fluorescent protein. *Proceedings of the National Academy of Sciences of the United States of America* **99**, 7877-7882 (2002).

117. Winnard, P.T., Jr., Kluth, J.B. & Raman, V. Noninvasive optical tracking of red fluorescent protein-expressing cancer cells in a model of metastatic breast cancer. *Neoplasia (New York, N.Y.)* **8**, 796-806 (2006).

118. Boche, D., Perry, V.H. & Nicoll, J.A. Review: activation patterns of microglia and

their identification in the human brain. *Neuropathology and applied neurobiology* **39**, 3-18 (2013).

119. Zhang, W., Moore, L. & Ji, P. Mouse models for cancer research. *Chinese journal of cancer* **30**, 149 (2011).

120. Cheon, D.-J. & Orsulic, S. Mouse models of cancer. (2011).

121. Zhang, C., Lowery, F.J. & Yu, D. Intracarotid Cancer Cell Injection to Produce Mouse Models of Brain Metastasis. *Journal of visualized experiments : JoVE* (2017).

122. Kienast, Y.*, et al.* Real-time imaging reveals the single steps of brain metastasis formation. *Nature medicine* **16**, 116-122 (2010).

123. Qiao, S., Qian, Y., Xu, G., Luo, Q. & Zhang, Z. Long-term characterization of activated microglia/macrophages facilitating the development of experimental brain metastasis through intravital microscopic imaging. **16**, 4 (2019).

124. Pelleitier, M. & Montplaisir, S. The nude mouse: a model of deficient T-cell function. *Methods and achievements in experimental pathology* **7**, 149-166 (1975).

125. Strik, H.M., Stoll, M. & Meyermann, R. Immune cell infiltration of intrinsic and metastatic intracranial tumours. *Anticancer research* **24**, 37-42 (2004).

126. Graeber, M.B., Scheithauer, B.W. & Kreutzberg, G.W. Microglia in brain tumors. *Glia* **40**, 252-259 (2002).

127. Watters, J.J., Schartner, J.M. & Badie, B. Microglia function in brain tumors. *Journal of neuroscience research* **81**, 447-455 (2005).

128. Morantz, R.A., Wood, G.W., Foster, M., Clark, M. & Gollahon, K. Macrophages in experimental and human brain tumors. Part 2: studies of the macrophage content of human brain tumors. *Journal of neurosurgery* **50**, 305-311 (1979).

129. Wu, S.-Y. & Watabe, K. The roles of microglia/macrophages in tumor progression of brain cancer and metastatic disease. *Frontiers in bioscience (Landmark edition)* **22**, 1805 (2017).

130. Wu, S.Y. & Watabe, K. The roles of microglia/macrophages in tumor progression of brain cancer and metastatic disease. *Frontiers in bioscience (Landmark edition)* **22**, 1805-1829 (2017).

131. Alarcon, C.R. & Tavazoie, S.F. Cancer: Endothelial-cell killing promotes metastasis. *Nature* **536**, 154-155 (2016).

132. Block, M.L., Zecca, L. & Hong, J.S. Microglia-mediated neurotoxicity: uncovering the molecular mechanisms. *Nature reviews. Neuroscience* **8**, 57-69 (2007).

133. Dheen, S.T., Kaur, C. & Ling, E.A. Microglial activation and its implications in the brain diseases. *Current medicinal chemistry* **14**, 1189-1197 (2007).

134. Iadecola, C. & Anrather, J. The immunology of stroke: from mechanisms to translation. *Nature medicine* **17**, 796-808 (2011).

135. Hambardzumyan, D., Gutmann, D.H. & Kettenmann, H. The role of microglia and macrophages in glioma maintenance and progression. *Nature neuroscience* **19**, 20-27 (2016).

136. Liu, C., Luo, D., Streit, W.J. & Harrison, J.K. CX3CL1 and CX3CR1 in the GL261 murine model of glioma: CX3CR1 deficiency does not impact tumor growth or infiltration of microglia and lymphocytes. *Journal of neuroimmunology* **198**, 98-105 (2008).

137. Leung, S.Y., Wong, M.P., Chung, L.P., Chan, A.S.Y. & Yuen, S.T. Monocyte chemoattractant protein-1 expression and macrophage infiltration in gliomas. *Acta neuropathologica* **93**, 518-527 (1997).

138. Badie, B., Schartner, J., Klaver, J. & Vorpahl, J. In vitro modulation of microglia motility by glioma cells is mediated by hepatocyte growth factor/scatter factor. *Neurosurgery* **44**, 1077-1082 (1999).

139. Rosen, E.M.*, et al.* Scatter factor expression and regulation in human glial tumors. *International journal of cancer* **67**, 248-255 (1996).

140. Denzer, K., Kleijmeer, M.J., Heijnen, H., Stoorvogel, W. & Geuze, H.J. Exosome: from internal vesicle of the multivesicular body to intercellular signaling device. *Journal of cell science* **113**, 3365-3374 (2000).

141. van den Boorn, J.G., Daßler, J., Coch, C., Schlee, M. & Hartmann, G. Exosomes as nucleic acid nanocarriers. *Advanced drug delivery reviews* **65**, 331-335 (2013).

142. Xia, H.*, et al.* MicroRNA-15b regulates cell cycle progression by targeting cyclins in glioma cells. *Biochemical and biophysical research communications* **380**, 205-210 (2009).

143. Xia, H.*, et al.* microRNA-146b inhibits glioma cell migration and invasion by targeting MMPs. *Brain research* **1269**, 158-165 (2009).

144. Xia, H.*, et al.* Loss of brain-enriched miR-124 microRNA enhances stem-like traits and invasiveness of glioma cells. *Journal of Biological Chemistry* **287**, 9962-9971 (2012).

145. Silber, J.*, et al.* miR-124 and miR-137 inhibit proliferation of glioblastoma multiforme cells and induce differentiation of brain tumor stem cells. *BMC medicine* **6**, 14 (2008).

146. Godlewski, J.*, et al.* MicroRNA-451 regulates LKB1/AMPK signaling and allows adaptation to metabolic stress in glioma cells. *Molecular cell* **37**, 620-632 (2010).

147. Cheng, L.-C., Pastrana, E., Tavazoie, M. & Doetsch, F. miR-124 regulates adult neurogenesis in the subventricular zone stem cell niche. *Nature neuroscience* **12**, 399 (2009).

148. Butcher, E.C. & Picker, L.J. Lymphocyte homing and homeostasis. *Science (New York, N.Y.)* **272**, 60-66 (1996).

149. Campbell, J.J.*, et al.* Chemokines and the arrest of lymphocytes rolling under flow conditions. *Science (New York, N.Y.)* **279**, 381-384 (1998).

150. Feng, X.*, et al.* Loss of CX3CR1 increases accumulation of inflammatory monocytes and promotes gliomagenesis. *Oncotarget* **6**, 15077-15094 (2015).

151. Yoshida, K., Fujikawa, T., Tanabe, A. & Sakurai, K. Quantitative analysis of distribution and fate of human lung cancer emboli labeled with 125I-5-iodo-2'-deoxyuridine in nude mice. *Surgery today* **23**, 979-983 (1993).

152. Eichler, A.F.*, et al.* The biology of brain metastases-translation to new therapies. *Nature reviews. Clinical oncology* **8**, 344-356 (2011).

153. van Furth, R. & Cohn, Z.A. The origin and kinetics of mononuclear phagocytes. *The Journal of experimental medicine* **128**, 415-435 (1968).

154. Ajami, B., Bennett, J.L., Krieger, C., Tetzlaff, W. & Rossi, F.M. Local self-renewal can sustain CNS microglia maintenance and function throughout adult life. *Nat Neurosci* **10**, 1538-1543 (2007).

155. Lawson, L.J., Perry, V.H. & Gordon, S. Turnover of resident microglia in the normal adult mouse brain. *Neuroscience* **48**, 405-415 (1992).

156. Parkhurst, C.N.*, et al.* Microglia promote learning-dependent synapse formation through brain-derived neurotrophic factor. *Cell* **155**, 1596-1609 (2013).

157. Rice, R.A.*, et al.* Elimination of Microglia Improves Functional Outcomes Following Extensive Neuronal Loss in the Hippocampus. **35**, 9977-9989 (2015).

158. Elmore, M.R.*, et al.* Colony-stimulating factor 1 receptor signaling is necessary for microglia viability, unmasking a microglia progenitor cell in the adult brain. *Neuron* **82**, 380-397 (2014).

159. Szalay, G.*, et al.* Microglia protect against brain injury and their selective elimination dysregulates neuronal network activity after stroke. *Nature communications* **7**, 11499 (2016).

160. Patel, S. & Player, M.R. Colony-stimulating factor-1 receptor inhibitors for the treatment of cancer and inflammatory disease. *Curr Top Med Chem* **9**, 599-610 (2009).

10 APPENDIX

Affidavit

Wenlong Zhang

ZHANG wenlong

Surname, first name

I hereby declare, that the submitted thesis entitled

The role of CX3CR1 in cerebral metastasis formation

is my own work. I have only used the sources indicated and have not made unauthorized use of services of a third party. Where the work of others has been quoted or reproduced, the source is always given.

I further declare that the submitted thesis or parts have not been presented as part of an examination degree to any other university.

Beijing，CHINA 26.03.2020 — Ort, Datum

Wenlong ZHANG — Unterschrift,Doktorand